NATIONAL ACADEMY OF SCIENCES OF UKRAINE ● G. V. KURDYUMOV INSTITUTE FOR METAL PHYSICS

A MONTHLY RESEARCH JOURNAL

METALLOPHYSICS AND ADVANCED TECHNOLOGIES

(Metallofizika i Noveishie Tekhnologii)

FOUNDED IN SEPTEMBER, 1979

Volume 48, No. 4; April 2026

CONTENTS

Scientific Editors of Issue—*O. S. Gatsenko, V. A. Tatarenko*
Executive Managing Editor—*O. S. Gatsenko*
Editors—*L. I. Makarenko, M. V. Manilo, I. V. Zagorulko*
The artwork for direct reproduction is made by computer group of EPD of the G. V. Kurdyumov Institute for Metal Physics, N.A.S. of Ukraine

Editorial Office Address:
G. V. Kurdyumov Institute for Metal Physics, N.A.S. of Ukraine, EPD—'MNT',
36 Academician Vernadsky Boulevard, UA-03142 Kyiv, Ukraine
Telephone: +380 44 4249042. Fax: +380 44 4242561. E-mail: mfint@imp.kiev.ua
Media Identifier R30-03171

Approved for publication by the Academic Council of the G. V. Kurdyumov Institute for Metal Physics of the National Academy of Sciences of Ukraine
Published in English or Ukrainian languages according to resolution of Editorial Board of the journal

Printed by Publishing House 'Akademperiodyka', of the NAS of Ukraine
4 Tereshchenkivs'ka Str., UA-01024 Kyiv, Ukraine
Registration Certificate of Publishing Subject: ДК № 544 on 27.07.2001

Journal website: http://mfint.imp.kiev.ua
Journal DOI: https://doi.org/10.15407/mfint

Issue DOI: https://doi.org/10.15407/mfint.48.04

НАЦІОНАЛЬНА АКАДЕМІЯ НАУК УКРАЇНИ ● ІНСТИТУТ МЕТАЛОФІЗИКИ ім. Г. В. Курдюмова

МЕТАЛОФІЗИКА ТА НОВІТНІ ТЕХНОЛОГІЇ

ЩОМІСЯЧНИЙ НАУКОВИЙ ЖУРНАЛ
ЗАСНОВАНИЙ У ВЕРЕСНІ 1979 р.

Том 48, № 4; квітень, 2026

ЗМІСТ

Наукові редактори випуску: *О. С. Гаценко, В. А. Татаренко*
Відповідальний секретар редакційної колегії *О. С. Гаценко*
Редактор-коректор *О. С. Гаценко*
Технічні редактори: *І. В. Загорулько, Л. І. Макаренко, М. В. Маніло*
Художні редактори: *І. В. Загорулько, Л. І. Макаренко, М. В. Маніло*
Оригінал-макет для прямого репродукування виготовлено комп'ютерною групою РВВ Інституту металофізики ім. Г. В. Курдюмова НАН України

Адреса редакції:
Інститут металофізики ім. Г. В. Курдюмова НАН України, РВВ—Редакція «МНТ»
бульв. Акад. Вернадського, 36; 03142 Київ, Україна
Тел.: +380 44 4249042; факс: +380 44 4242561
Ел. пошта: mfint@imp.kiev.ua
Ідентифікатор медіа R30-03171

Затверджено до друку вченою радою Інституту металофізики ім. Г. В. Курдюмова НАН України
Друкується за постановою редакційної колегії журналу англійською або українською мовами

Підписано до друку 30.04.2026 р. Формат 70×100/16.
Ум. друк. арк. 9,34. Обл.-вид. арк. 8,60.
Наклад 55 пр. Зам. № 0000 від 30.04.2026 р.

Віддруковано ВД «Академперіодика» НАН України
вул. Терещенківська, 4; 01024 Київ, Україна
Свідоцтво суб'єкта видавничої справи ДК № 544 від 27.07.2001 р.

Сайт журналу: http://mfint.imp.kiev.ua
DOI (журналу): https://doi.org/10.15407/mfint
DOI (випуску): https://doi.org/10.15407/mfint.48.04

INFORMATION (GUIDELINES) FOR CONTRIBUTORS

Submission of Manuscripts: Manuscripts should be sent by e-mail (mfint@imp.kiev.ua). Additionally, they can be sent by regular mail to Executive Managing Editor, Editorial Office, G. V. Kurdyumov Institute for Metal Physics, N.A.S. of Ukraine, 36 Academician Vernadsky Boulevard, UA-03142 Kyiv, Ukraine. Manuscripts may also be submitted to a member of the Editorial Advisory Board or to the appropriate Regional Editor who is familiar with the research presented.
Submission of a paper to '*Metallophysics and Advanced Technologies*' (transliteration: '*Metallofizika i Noveishie Tekhnologii*', *i.e.*, '*MfNT*') will be taken to imply that it represents original work not previously published, that it is not being considered for publication elsewhere, and that, if accepted for publication, it will not be republished without the consent of the Editors and Publisher. It is a condition of acceptance by the Editor of a manuscript for publication that the Publishers acquire automatically the copyright in the manuscript throughout the world. Journal '*MfNT*' supports the generally accepted principles described in documents on publication ethics and unacceptable practices, which are presented on the journal website.
Scope of the Journal: *Electronic Structure and Properties, Crystal-Lattice Defects, Phase Transformations, Physics of Strength and Plasticity, Metallic Surfaces and Films, Structure and Properties of Nanoscale and Mesoscopic Materials, Amorphous and Liquid States, Interactions of Radiation and Particles with Condensed Matter, Materials in Extremal Conditions, Reactor and Aerospace Metals Science, Medical Metals Science, New Metallic Materials and Synthetic Metals, Metal-Containing Smart Materials, Physical and Technical Basis of Experiment and Diagnostics, Articles under Discussion*.
Language: The language of publication may be English (preferably) or Ukrainian.
Abstract: Each paper requires an abstract of 200–250 words summarizing the significant coverage and findings (the use of mathematical symbols and expressions in abstract is not recommended).
Keywords and PACS numbers: 5–7 keywords and PACS numbers reflecting the content of the contribution should be supplied (see 'Physics and Astronomy Classification Scheme 2010').
Manuscript Preparation: Papers should be formatted according to the template, which can be downloaded from the Journal's website. The length of **research papers** should not in general exceed 5000 words and 10 figures; **review articles** should not exceed 10000 words and 30 figures, including tables and diagrams. Authors are urged to arrange the subject matter clearly under headings such as: 1. Introduction, 2. Experimental/Theoretical Details, 3. Results, 4. Discussion, 5. Conclusion, References. Subsections should be identified with section and subsection numbers (such as 6.1. Second-Value Subheading).
References and Notes: Notes are indicated in the text by consecutive superior Arabic numbers (without parentheses). References should be numbered consecutively (in square brackets) throughout the text. The full list should be collected and typed at the end of the paper in numerical order. Listed references should be completed in all details including **DOI** (if available) but excluding article titles in journals. **All authors'** initials should precede their names. Examples of references preparation:

1. S. O. Firstov and T. G. Rogul, *Metallofiz. Noveishie Tekhnol.*, **44**, No. 1: 127 (2022) (in Ukrainian). https://doi.org/10.15407/mfint.44.01.0127
2. V. B. Tarelnyk, O. P. Gaponova, and Ye. V. Konoplianchenko, *Prog. Phys. Met.*, **23**, No. 1: 27 (2022). https://doi.org/10.15407/ufm.23.01.027
3. A. Meisel, G. Leonhardt, and R. Szargan, *Röntgenspektren und Chemische Bindung* [X-Ray Spectra and Chemical Bond] (Leipzig: Akademische Verlagsgesellschaft Geest & Portig K.-G.: 1977) (in German).
4. J. M. Ziman, *Printsipy Teorii Tverdogo Tela* [Principles of the Theory of Solids] (Moscow: Mir: 1974) (Russian translation).
5. M. A. Stucke, D. M. Dimiduk, and D. M. Hazzledine, *High Temperature Ordered Intermetallic Alloys. V* (Eds. I. Baker and R. Darolia) (Pittsburgh, PA, USA: MRS: 1993), p. 471.
6. *Handbook of Mathematical Functions with Formulas, Graphs and Mathematical Tables* (Eds. M. Abramowitz and I. A. Stegun), Nat'l Bureau of Standards. Appl. Math. Ser. Vol. **55** (Washington, D.C.: U.S. Govt. Printing Office: 1964).
7. B. B. Karpovych and O. B. Borovkoff, *Proc. of Symp. 'Micromaterials Engineering' (Dec. 25–31, 1999)* (Kyiv: RVV IMF: 2000), vol. **2**, p. 113 (in Russian).
8. A. E. Krug, *Abstr. Int. Conf. Phys. Phenomena (Dec. 25–31, 1991, Alushta)* (Kharkiv: 1991), p. 12.
9. T. M. Radchenko, *Vplyv Uporyadkuvannya Defektnoyi Struktury на Transportni Vlastyvosti Zmishanykh Krystaliv* [Influence of Ordering of the Defect Structure on Transport Properties of the Mixed Crystals] (Thesis of Disser. for the Degree of Dr. Phys.-Math. Sci.) (Kyiv: G. V. Kurdyumov Institute for Metal Physics, N.A.S.U.: 2015) (in Ukrainian). https://doi.org/10.13140/RG.2.2.35430.22089

10. E. M. Gololobov, V. B. Shipilo, N. I. Sedrenok, and A. I. Dudyak, *Sposob Polucheniya Karbonitridov Metallov* [Production Method of Metal Carbonitrides], Authors' Certificate 722341 SSSR (Publ. November 21, 1979) (in Russian).
11. V. G. Trubachev, K. V. Chuistov, V. N. Gorshkov, and A. E. Perekos, *Sposob Polucheniya Metallicheskikh Poroshkov* [The Technology of Metallic Powder Production]: Patent 1639892 SU. MKI, B22 F9/02, 9/14 (Otkrytiya i Izobreteniya, **34**, No. 13: 11) (1991) (in Russian).
12. Yu. M. Koval' and V. V. Nemoshkalenko, *O Prirode Martensitnykh Prevrashcheniy* [On the Nature of Martensitic Transformations] (Kyiv: 1998) (Prepr./N.A.S. of Ukraine. Inst. for Metal Physics. No. 1, 1998) (in Russian).

Journal title abbreviations should conform to generally accepted styles:
https://www.cas.org/support/documentation/references/corejournals;
https://cdn.journals.aps.org/files/rmpguapb.pdf;
https://images.webofknowledge.com/WOK46P9/help/WOS/A_abrvjt.html;
https://mathscinet.ams.org/msnhtml/serials.pdf.

Equations and Formulae: Formulas in the text should be inserted by **MathType**, fully compatible with MS Office. Vectors should be typed in bold without arrows above. Note that complicated formulae, mathematical expressions or (de)notations are not recommended in the title, abstract, and keywords.

Tables: Number tables consecutively with Arabic numerals and give a clear descriptive caption at the top.

Figures: All figures should be numbered with consecutive Arabic numbers, have descriptive captions and be mentioned in the text. Keep figures separate at the end of the text and clearly label each figure with author's name and figure number. The labels at axis should contain the designation (or notation) of quantities and their units.

Preparation: Figures submitted must be of a high enough standard for reproduction with 300–600 dpi resolution (including half-tone illustrations). Redrawing or retouching of unusable figures will be charged to the authors.

Colour Plates: Whenever, the use of colour is an integral part of the research, or where the work is generated in colour, the Journal will publish (in paper version) the colour illustrations with charge to the author. Reprints in colour will carry a surcharge. Please write to the Publisher for details.

Submission of Electronic Text: Authors should submit the electronic version of their paper by e-mail to the Editorial Office. The text file should be saved in the native formats of the MS Word with a name consisting the name of the first author, for example, Hotovchenko.docx. The electronic form of figures (in TIF, EPS, JPG, PNG formats preferably and with name consisting the name of the first author also, for example, Hotovchenko_fig2a.jpg) should be planned so that they reduce to 12.7 cm column width (or less), and keep them separated from the text file. It is desirable to submit additionally all the **figures** within the format of the program, in which they were created.

Proofs: Contributors will receive page proofs for correction by e-mail as a PDF document. These must be returned to Kyiv office (mfint@imp.kiev.ua with subject beginning by word 'mfint') within 5 days of receipt.

Page Charges: There are no page charges to individuals or institutions.

Reprints: Authors can freely download a PDF version of their published article from journal website: https://mfint.imp.kiev.ua. The printed issues may be ordered by completing the appropriate form sent with proofs and prepaid by authors under the terms as for subscription.

Further Information: All questions arising during the **peer review** or after acceptance of manuscripts, especially those relating to reprints, should be directed to G. V. Kurdyumov Institute for Metal Physics, N.A.S. of Ukraine, Executive Managing Editor, Editorial Office, 36 Academician Vernadsky Blvd., UA-03142 Kyiv, Ukraine;
Fax: +380 44 4242561, e-mail: mfint@imp.kiev.ua (with subject beginning by word 'mfint').

We ask the authors to apply with their manuscript Copyright Transfer Agreement form.

Copyright Transfer Agreement

We, the undersigned authors of the manuscript '_____', transfer to the Founders, Publisher, and Editorial Board of the Journal 'Metallophysics and Advanced Technologies' (according to agreements between them) the right to publish this manuscript in original language or in translation to the other languages. We confirm that publication of this manuscript **will not** infringe a copyright of other persons or organizations and publication ethics.

Author(s):_____
(Last Name, First Name, Affiliation)

Correspondence Address:_____

Phone and e-mail: _____

_____ _____
(Signature) *(Date)*

ІНФОРМАЦІЯ (ПРАВИЛА) ДЛЯ АВТОРІВ

Науковий журнал «Металофізика та новітні технології» (МфНТ) щомісяця публікує статті, які раніше ще не публікувалися та не перебувають на розгляді для опублікування в інших виданнях. Статті мають містити результати експериментальних і теоретичних досліджень в області фізики та технологій металів, стопів і сполук з металічними властивостями; рецензії на монографії; інформацію про конференції, семінари; відомості з історії металофізики; рекламу нових технологій, матеріялів, приладів. Журнал дотримується загальноприйнятих принципів, зазначених на його сайті в документах з публікаційної етики та щодо неприйнятних практик.

Тематика журналу: *Електронні структура та властивості, Дефекти кристалічної ґратниці, Фазові перетворення, Фізика міцности та пластичности, Металічні поверхні та плівки, Будова та властивості наномасштабних і мезоскопічних матеріялів, Аморфний і рідкий стани, Взаємодії випромінення та частинок із конденсованою речовиною, Матеріяли в екстремальних умовах, Реакторне й авіакосмічне металознавство, Медичне металознавство, Нові металеві матеріяли та синтетичні метали, Металовмісні смарт-матеріяли, Фізико-технічні основи експерименту та діягностики, Дискусійні повідомлення*.

Статті публікуються однією з двох мов: англійською (віддається перевага) або українською.

Статті, в оформленні яких не дотримано наступних правил для опублікування в МфНТ, повертаються авторам без розгляду по суті. (Датою надходження вважається день повторного надання статті після дотримання зазначених нижче правил.)

1. Стаття має бути підписаною всіма авторами (із зазначенням їхніх адрес електронної пошти); слід вказати прізвище, ім'я та по батькові автора, з яким редакція буде вести листування, його поштову адресу, номери телефону та факсу й адресу електронної пошти.

2. Виклад матеріялу має бути чітким, **структурованим** (розділами, наприклад, «1. Вступ», «2. Експериментальна/Теоретична методика», «3. Результати та їх обговорення», «4. Висновки», «Цитована література»), стислим, без довгих преамбул, відхилень і повторів, а також без дублювання в тексті даних таблиць, рисунків і підписів до них. Анотація та розділ «Висновки» мають не дублювати один одного. Числові дані слід наводити в загальноприйнятих одиницях.

3. Об'єм оригінальної (неоглядової) статті має бути не більше 5000 слів (з урахуванням основного тексту, таблиць, підписів до рисунків, списку використаних джерел) і 10 рисунків. **Об'єм оглядової статті** — до 10000 слів та 30 рисунків.

4. За потреби до редакції може надаватися друкований (А4, подвійний інтервал) примірник рукопису з ілюстраціями.

5. До редакції обов'язково надається (по **e-mail**) файл статті, набраний у текстовому редакторі Microsoft Word, з назвою, що складається з прізвища першого автора (латиницею), наприклад, Hotovchenko.docx.

6. Електронна версія рукопису та його друкований варіянт (в разі його надання) мають бути ідентичними. Вони мають оформлюватися за шаблоном, який можна завантажити з сайту журналу, і містити 5–7 **індексів PACS** в редакції 'Physics and Astronomy Classification Scheme 2010'. Тексти статей мають також містити **назву статті**, **список авторів**, **повні назви** та **поштові адреси установ**, в яких вони працюють, **анотацію статті** (200–250 слів), **5–7 ключових слів** двома мовами (**англійською** та **українською**), а заголовки таблиць і підписи до рисунків мають подаватися **як мовою рукопису, так і англійською мовою**; англомовна анотація може бути представленою в більш розгорнутому варіянті (до 500 слів). Назва статті, її анотація та ключові слова мають не містити складні формули, математичні вирази чи позначення.

7. Електронні версії рисунків мають бути представленими у вигляді окремих файлів (у форматах TIF, EPS, JPG, PNG з розріженням у 300–600 dpi) з назвами, що складаються з прізвища першого автора (латиницею) та номера рисунка, наприклад, Hotovchenko_fig2a.jpg. Додатково рисунки надаються у форматі програми, в якій вони створювалися.

8. Написи на рисунках (особливо на півтонових) слід по можливості замінити літерними позначеннями (набраними на контрастному фоні), а криві позначити цифрами або різними типами ліній/маркерів, які мають бути роз'ясненими в підписах до рисунків або в тексті. На графіках усі лінії/маркери мають бути достатньої товщини/розміру для якісного відтворення їх у зменшеному в 2–3 рази вигляді (рекомендована початкова ширина рисунка — 12,7 см). Світлини мають бути чіткими та контрастними, а написи та позначення мають не закривати істотні деталі (для чого можна використовувати стрілки). Замість зазначення в підтекстовці збільшення під час зйомки бажано проставити масштаб (на контрастному фоні) на одній з ідентичних світлин. На графіках підписи до осей, **виконані мовою статті**, мають містити позначення (або найменування) величин, що відкладаються вздовж осей, і відділені комою їхні одиниці вимірювання.

9. Формули в текст треба вставляти за допомогою редактора формул **MathType**, сумісного з MS Office. **Вектори** слід набирати напівтовстим шрифтом без стрілок зверху.

10. Рисунки, таблиці, формули, а також підрядкові **примітки (виноски)** мають нумеруватися поспіль по всій статті.

11. Посилання на літературні джерела слід давати у вигляді порядкового номера, надрукованого в рядок у квадратних дужках. Список цитованої літератури складається почергово за першою згадкою джерела. Приклади оформлення посилань наведено нижче (просимо звернути увагу на порядок розташування ініціалів і прізвищ авторів, бібліографічних відомостей і на розділові знаки, а також на необхідність зазначення **всіх** співавторів цитованої роботи та її ідентифікатора **DOI**, якщо він є):

1. S. O. Firstov and T. G. Rogul, *Metallofiz. Noveishie Tekhnol.*, **44**, No. 1: 127 (2022) (in Ukrainian). https://doi.org/10.15407/mfint.44.01.0127
2. V. B. Tarelnyk, O. P. Gaponova, and Ye. V. Konoplianchenko, *Prog. Phys. Met.*, **23**, No. 1: 27 (2022). https://doi.org/10.15407/ufm.23.01.027
3. A. Meisel, G. Leonhardt, and R. Szargan, *Röntgenspektren und Chemische Bindung* [X-Ray Spectra and Chemical Bond] (Leipzig: Akademische Verlagsgesellschaft Geest & Portig K.-G.: 1977) (in German).
4. J. M. Ziman, *Printsipy Teorii Tverdogo Tela* [Principles of the Theory of Solids] (Moscow: Mir: 1974) (Russian translation).
5. M. A. Stucke, D. M. Dimiduk, and D. M. Hazzledine, *High Temperature Ordered Intermetallic Alloys. V* (Eds. I. Baker and R. Darolia) (Pittsburgh, PA, USA: MRS: 1993), p. 471.
6. *Handbook of Mathematical Functions with Formulas, Graphs and Mathematical Tables* (Eds. M. Abramowitz and I. A. Stegun), Nat'l Bureau of Standards. Appl. Math. Ser. Vol. **55** (Washington, D.C.: U.S. Govt. Printing Office: 1964).
7. B. B. Karpovych and O. B. Borovkoff, *Proc. of Symp. 'Micromaterials Engineering' (Dec. 25–31, 1999)* (Kyiv: RVV IMF: 2000), vol. **2**, p. 113 (in Russian).
8. A. Eh. Krug, *Abstr. Int. Conf. Phys. Phenomena (Dec. 25–31, 1991, Alushta)* (Kharkiv: 1991), p. 12.
9. T. M. Radchenko, *Vplyv Uporyadkuvannya Defektnoyi Struktury na Transportni Vlastyvosti Zmishanykh Krystaliv* [Influence of Ordering of the Defect Structure on Transport Properties of the Mixed Crystals] (Thesis of Disser. for the Degree of Dr. Phys.-Math. Sci.) (Kyiv: G. V. Kurdyumov Institute for Metal Physics, N.A.S.U.: 2015) (in Ukrainian). https://doi.org/10.13140/RG.2.2.35430.22089
10. E. M. Gololobov, V. B. Shipilo, N. I. Sedrenok, and A. I. Dudyak, *Sposob Polucheniya Karbonitridov Metallov* [Production Method of Metal Carbonitrides], Authors' Certificate 722341 SSSR (Publ. November 21, 1979) (in Russian).
11. V. G. Trubachev, K. V. Chuistov, V. N. Gorshkov, and A. E. Perekos, *Sposob Polucheniya Metallicheskikh Poroshkov* [The Technology of Metallic Powder Production]: Patent 1639892 SU. MKI, B22 F9/02, 9/14 (Otkrytiya i Izobreteniya, **34**, No. 13: 11) (1991) (in Russian).
12. Yu. M. Koval' and V. V. Nemoshkalenko, *O Prirode Martensitnykh Prevrashcheniy* [On the Nature of Martensitic Transformations] (Kyiv: 1998) (Prepr./N.A.S. of Ukraine. Inst. for Metal Physics. No. 1, 1998) (in Russian).

Слід використовувати загальноприйняті скорочення назв журналів:
https://www.cas.org/support/documentation/references/corejournals;
https://cdn.journals.aps.org/files/rmpguapb.pdf;
https://images.webofknowledge.com/WOK46P9/help/WOS/A_abrvjt.html;
https://mathscinet.ams.org/msnhtml/serials.pdf.

Необхідною вимогою є також надання авторами додаткового списку цитованої літератури (**References**) в **латинській транслітерації** (система **BGN/PCGN**; рекомендовані транслітератори: http://www.slovnyk.ua/services/translit.php; http://ru.translit.net/?account=bgn).

Після транслітерованих назв книг, дисертацій, патентів та ін. слід у квадратних дужках наводити їхній англомовний переклад (див. приклади вище). При транслітерації статей з МфНТ слід використовувати написання П.І.Б. авторів, наведені **лише** в англомовному змісті відповідного випуску, і **офіційну** транслітеровану назву журналу (див. також першу сторінку кожної статті та сайт).

12. Коректура авторам надсилається електронною поштою у вигляді pdf-файлу після завершення етапу **рецензування**. На перевірку коректури авторам відводяться 5 робочих днів. Після закінчення зазначеного терміну стаття автоматично направляється до друку. Виправлення слід відмітити та прокоментувати в самому pdf-файлі або оформити у вигляді переліку виправлень (підписаного уповноваженим представником колективу авторів) і переслати електронною поштою на адресу редакції.

Електронний варіянт статті надсилається на e-mail: mfint@imp.kiev.ua (з темою, що починається словом 'mfint'). Друкована версія рукопису (якщо у ній є потреба) надсилається за адресою: **Інститут металофізики ім. Г. В. Курдюмова НАН України, редакція МфНТ; бульвар Акад. Вернадського, 36; 03142 Київ, Україна** або відповідному реґіональному редактору (див. сайт).

Автори можуть вільно завантажити pdf-файли опублікованих статей з сайту журналу (https://mfint.imp.kiev.ua), а також замовити друковані примірники випуску журналу зі своєю статтею, надіславши до редакції журналу **разом з коректурою відповідну заявку та квитанцію про оплату** друку необхідної кількості примірників випуску на умовах, аналогічних передплатним.

Відповідно до угод між редакцією МфНТ, засновниками та видавцем журналу, редакція вважає, що автори, надсилаючи їй рукопис статті, передають засновникам, видавцю та редколеґії право опублікувати цей рукопис мовою ориґіналу та в перекладі іншими мовами, і просить авторів відразу прикладати до рукопису «Угоду про передачу авторського права».

Угода про передачу авторського права

Ми, що нижче підписалися, автори рукопису «_____», передаємо засновникам, видавцю та редколеґії журналу «Металофізика та новітні технології» (згідно з угодами між ними) право опублікувати цей рукопис мовою ориґіналу та в перекладі іншими мовами. Ми підтверджуємо, що ця публікація **не** порушує авторського права інших осіб або організацій і принципів наукової етики. При цьому за авторами зберігаються всі інші права як власників цього рукопису.

Підписи авторів: _____ (П.І.Б., дата, адреса, тел., e-mail)

Metallophysics and Advanced Technologies
Металофіз. новітні технол.
Metallofiz. Noveishie Tekhnol.
2026, vol. 48, No. 4, pp. 341–350
https://doi.org/10.15407/mfint.48.04.0341
Reprints available directly from the publisher

PACS numbers: 47.65.Cb, 61.05.cp, 72.20.Pa, 75.50.Mm, 75.75.Cd, 83.60.Np, 83.80.Gv

Synthesis and Electrical Characterization of Spinel $M\mathrm{Fe_2O_4}$ (M = Ni, Co, Fe) Magnetic Nanoparticles

U. E. Nurimov, O. Q. Quvondiqov

Samarkand State University named after Sharof Rashidov,
15 University Blvd.,
UZ-140104 Samarkand, Uzbekistan

In this investigation, we delve into the precise synthesis of magnetic nanoparticles with a particular emphasis on the $\mathrm{NiFe_2O_4}$ and $\mathrm{CoFe_2O_4}$ ferrites, and the $\mathrm{FeFe_2O_4}$ magnetite, employing a meticulously controlled chemical-synthesis methodology to ensure reproducibility and optimal material properties. To verify the chemical makeup and purity of these synthesized nanoparticles, we conduct the detailed characterization through energy-dispersive x-ray spectroscopy (EDX), which provides quantitative insights into their elemental composition. Leveraging these well-characterized nanoparticles as the foundational components, we formulate a series of magnetic fluids at diverse concentration levels, tailoring their rheological and magnetic behaviours for potential applications in fields such as biomedicine, electronics, and environmental remediation. Additionally, to assess comprehensively the thermoelectrical performance of these magnetic fluids, we perform systematic measurements of their electrical conductivity over an extensive temperature spectrum, thereby, elucidating how thermal variations influence their conductive characteristics and overall functionality under varying operational environments.

Key words: magnetic nanoparticles, spinel ferrite nanoparticles, electrical conductivity, thermoelectrical properties, concentration effects, magnetic fluid, nanoparticles' dispersion.

Corresponding author: Umidjon Elmuradovich Nurimov
E-mail: nurimovumid1@gmail.com

Citation: U. E. Nurimov and O. Q. Quvondiqov, Synthesis and Electrical Characterization of Spinel $M\mathrm{Fe_2O_4}$ (M = Ni, Co, Fe) Magnetic Nanoparticles, *Metallofiz. Noveishie Tekhnol.*, **48**, No. 4: 341–350 (2026), DOI: 10.15407/mfint.48.04.0341

У цьому дослідженні ми розглядаємо прецизійну синтезу магнетних наночастинок із особливим акцентом на феритах Ni_2Fe_2O, $CoFe_2O_4$ та магнетиті $FeFe_2O_4$, використовуючи ретельно контрольовану методологію хемічної синтези для забезпечення відтворюваности й оптимальних властивостей матеріялу. Для підтвердження хемічного складу та чистоти синтезованих наночастинок було проведено детальну характеризацію за допомогою енергодисперсійної рентґенівської спектроскопії (EDX), що забезпечило кількісну оцінку їхнього елементного складу. Використовуючи ці добре охарактеризовані наночастинки в якості базових компонентів, було створено серію магнетних рідин із різними концентраційними рівнями, що уможливило цілеспрямовано модифікувати їхні реологічні та магнетні властивості для потенційного застосування в таких галузях, як біомедицина, електроніка й послаблення впливу на довкілля. Крім того, з метою комплексної оцінки термоелектричних характеристик цих магнетних рідин було проведено систематичні міряння їхньої електропровідности в широкому температурному діяпазоні, що дало змогу з'ясувати вплив температурних змін на їхні провідні властивості та загальну функціональність у різних умовах експлуатації.

Ключові слова: магнетні наночастинки, наночастинки шпінельного фериту, електропровідність, термоелектричні властивості, концентраційні ефекти, магнетна рідина, дисперсія наночастинок.

(Received 31 August, 2025; in final version, 13 March, 2026)

1. INTRODUCTION

The rapid advancement of science and technology in the 21st century has posed significant environmental challenges, necessitating innovative solutions from materials science and physics. Magnetic fluids, or ferrofluids, have emerged as versatile nanomaterials with promising potential to address these issues through their unique magneto-responsive properties [1, 7]. These colloidal suspensions, comprising magnetic nanoparticles dispersed in a carrier liquid with stabilizing surfactants, exhibit tuneable magnetic, electrical, and rheological behaviours, enabling applications in aerospace engineering, electronics, mechanical systems, biomedicine, and environmental remediation such as water and oil purification [5, 6]. This broad applicability has garnered substantial interest from the scientific community, driving research into their synthesis, characterization, and property optimization.

Magnetic fluids typically consist of magnetic nanoparticles dispersed in a liquid carrier medium and stabilized by surface-active agents. Among these components, magnetic nanoparticles are the primary determinants of the materials' performance [4, 9]. While the chemical composition governs the general quality of the fluid, the size, morphology, and crystal structure of the nanoparticles critically in-

fluence their fundamental physical, chemical, and functional properties. In particular, nanoparticles with the general formula MFe$_2$O$_4$ (M = Ni, Co, Fe) belong to the family of spinel ferrites, which are known for their remarkable magnetic and electrical characteristics [1, 2, 6]. However, the microstructural features and the mechanisms underlying the variations in magnetization and electrical behaviour in fluids containing mixed-metal ferrite nanoparticles remain insufficiently understood [5].

Despite extensive experimental and theoretical investigations, no unified framework describing the internal structure–property relationships of MFe$_2$O$_4$-based magnetic fluids has been established. Furthermore, the origins of variability in their electrical properties, especially as a function of composition, concentration, and temperature, have not been comprehensively explored. In this study, magnetic nanoparticles of MFe$_2$O$_4$ (M = Ni, Co, Fe) were synthesized *via* a chemical condensation method [11, 12]. The chemical composition of the nanoparticles was characterized using Energy-Dispersive X-Ray Spectroscopy (EDX). Magnetic fluids with varying nanoparticle concentrations, prepared using water as the base medium, were evaluated for their electrical conductivity across a range of temperatures. The findings of this work aim to contribute to the understanding of composition–structure–property relationships in spinel ferrite-based magnetic fluids, thereby, facilitating their targeted design for advanced engineering and environmental applications [4, 7].

2. EXPERIMENTAL DETAILS

2.1. Materials

Ferric chloride hexahydrate ($FeCl_3 \cdot 6H_2O$, ≥99%), ferrous chloride tetrahydrate ($FeCl_2 \cdot 4H_2O$, ≥99%), aqueous ammonia (NH_3(aq), 25%), oleic acid ($C_{18}H_{34}O_2$, ≥99%), citric acid ($C_6H_8O_7$, ≥99.5%), and acetone (C_3H_6O, ≥99.5%) were used as received. Deionized water (resistivity ≥ 18.2 MΩ·cm) was used in all preparations.

2.2 Synthesis of magnetite ($FeFe_2O_4$) nanoparticles

$FeFe_2O_4$ nanoparticles were prepared by chemical co-precipitation. Briefly, 2.0 g $FeCl_2 \cdot 4H_2O$ and 5.6 g $FeCl_3 \cdot 6H_2O$ (molar ratio FeI^+:FeI^+ = = 1:2) were dissolved in 100 mL deionized water and heated to 96°C under vigorous stirring. A total of 20 mL NH_4OH was added dropwise *via* syringe; the suspension was maintained at 96°C for 55 min. Then, 4.0 g citric acid (in 20 mL water) and 20 mL oleic acid were added sequentially. The mixture was heated to 100°C and stirred for an addi-

tional 90 min.

A small aliquot was diluted twofold and exposed to a constant magnetic field (0.35 T) to confirm magnetic response; the colloid remained stable in zero field. Excess unbound acids were removed by standing for 24 h followed by filtration. The precipitate was dried at room temperature for 48 h to yield $FeFe_2O_4$ nanopowder.

2.3 Synthesis of $NiFe_2O_4$ and $CoFe_2O_4$ nanoparticles

$NiFe_2O_4$ and $CoFe_2O_4$ nanoparticles were synthesised analogously by substituting the corresponding divalent metal salts for FeI^+ while maintaining the overall FeI^+:MI^+ stoichiometry (M = Ni or Co). Post-addition, the suspensions were aged at 100°C for 90 min, purified, and dried as above to obtain the respective ferrite nanopowders.

2.4 Reaction chemistry and stoichiometry

The co-precipitation proceeds *via* hydroxide formation, followed by in-situ dehydration/condensation to the spinel ferrite under hydrothermal-like ageing (≅ 100°C). The stepwise and net reactions are:
(*a*) nickel ferrite ($NiFe_2O_4$):

$$Ni^{2+} + 2Fe^{3+} + 8OH^- \rightarrow Ni(OH)_2 \cdot 2Fe(OH)_3 \rightarrow (100^oC) \rightarrow NiFe_2O_4;$$

(*b*) cobalt ferrite ($CoFe_2O_4$):

$$Co^{2+} + 2Fe^{3+} + 8OH^- \rightarrow Co(OH)_2 \cdot 2Fe(OH)_3 \rightarrow (100^oC) \rightarrow CoFe_2O_4;$$

(*c*) magnetite ($FeFe_2O_4$):

$$Fe^{2+} + 2Fe^{3+} + 8OH^- \rightarrow Fe(OH)_2 \cdot 2Fe(OH)_3 \rightarrow (100^oC) \rightarrow Fe_3O_4.$$

3. RESULTS AND DISCUSSIONS

Samples of $FeFe_2O_4$, $CoFe_2O_4$, and $NiFe_2O_4$ were analysed for their elemental composition using Energy Dispersive X-Ray (EDX) Spectroscopy. The EDX spectra of these samples are presented in Figs. 1–3.

The elemental composition of $NiFe_2O_4$ magnetic nanoparticles was determined using EDX Spectroscopy and studied in a dispersed state. The EDX spectrum obtained for $NiFe_2O_4$ magnetic nanoparticles is presented in Fig. 1. According to this figure, the sample contains Fe at 65.3% by mass, Ni at 34.5%, and Co at 0.22%.

The elemental composition of $CoFe_2O_4$ magnetic nanoparticles was determined using EDX Spectroscopy and studied in a dispersed state.

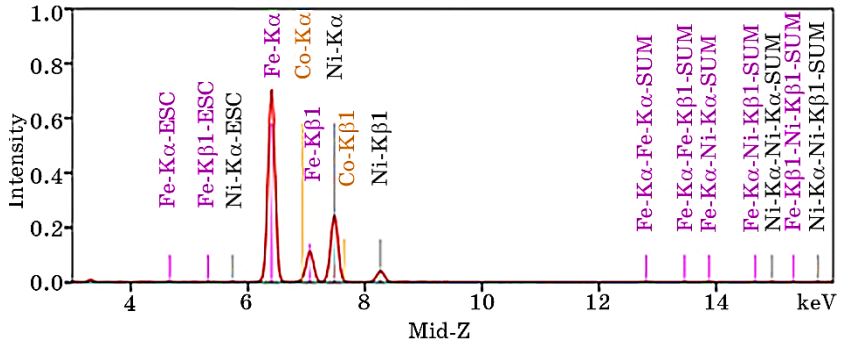

Fig. 1. EDX spectrum of powdered $NiFe_2O_4$ magnetic nanoparticles.

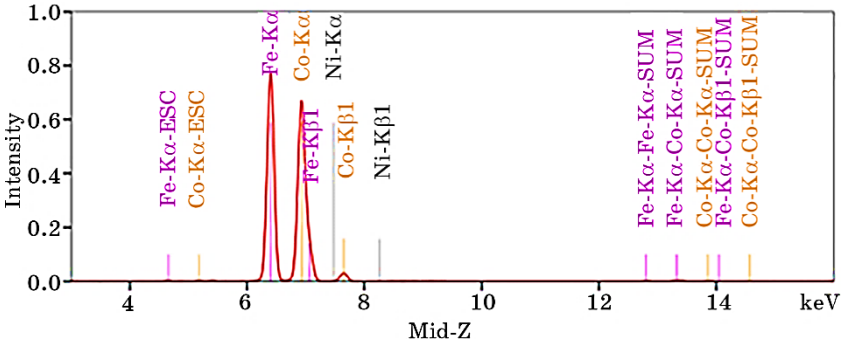

Fig. 2. EDX spectrum of powdered $CoFe_2O_4$ magnetic nanoparticles.

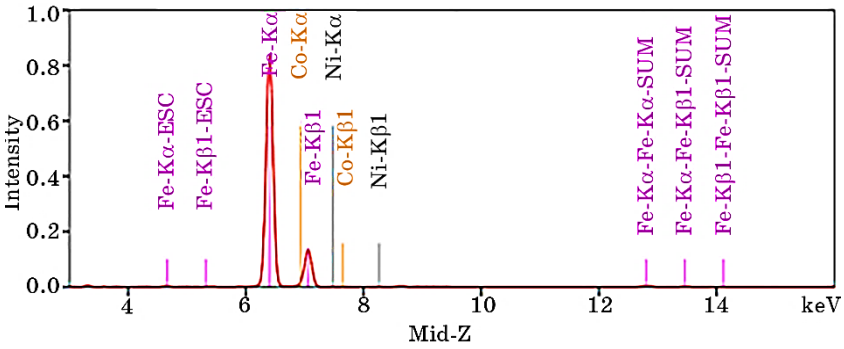

Fig. 3. EDX spectrum of powdered $FeFe_2O_4$ magnetic nanoparticles.

The EDX spectrum obtained for $CoFe_2O_4$ magnetic nanoparticles is presented in Fig. 2. According to this figure, the sample contains Fe at 61.5% by mass, Ni at 0.1%, and Co at 38.4%.

The elemental composition of $FeFe_2O_4$ magnetic nanoparticles was

determined using EDX Spectroscopy and studied in a dispersed state. The EDX spectrum obtained for $FeFe_2O_4$ magnetic nanoparticles is presented in Fig. 3. According to this figure, the sample contains Fe at 99.7% by mass, Ni at 0.1%, and Co at 0.2%. These results are presented in Tables 1–3 below.

Based on the results from Tables 1–3, it can be concluded that $NiFe_2O_4$, $CoFe_2O_4$, and $FeFe_2O_4$ magnetic nanoparticles were successfully synthesized.

The crystal structures of $NiFe_2O_4$, $CoFe_2O_4$, and $FeFe_2O_4$ magnetic nanoparticles were studied using x-ray diffraction (XRD) spectra. The $NiFe_2O_4$, $CoFe_2O_4$, and $FeFe_2O_4$ magnetic nanoparticles were dried, converted into powder form, and placed in a special container. X-ray beams with a uniform wavelength were directed onto their surfaces at angles ranging from 10° to 75° degrees. These reflected beams diffracted in the magnetic nanoparticles when positioned at an angle satisfying the Bragg condition. The dependence of the intensity of these diffracted x-ray beams on the angle of incidence on the nanoparticle surface is shown in Fig. 4 [5, 6, 9].

The structure of the magnetic nanoparticles was studied based on the relationship between the obtained intensity and the angle of incidence. As seen in Figure 4, the x-ray diffraction spectra of the synthesized magnetic nanoparticles show intensity peaks corresponding to

TABLE 1. Analysis results of the composition of $NiFe_2O_4$ magnetic nanoparticles.

No.	Element	Content	Statistical Error	Spectral Line	Intensity [cps·μA^{-1}]
1	Fe	65.3 wt.%	±0.0443%	M: FeK_α	285.91789
2	Ni	34.5 wt.%	±0.0263%	M: NiK_α	105.82723
3	Co	0.22 wt.%	±0.0061%	M: CoK_α	1.47739

TABLE 2. Analysis results of the composition of $CoFe_2O_4$ magnetic nanoparticles.

No.	Element	Content	Statistical Error	Spectral Line	Intensity [cps·μA^{-1}]
1	Fe	61.5 wt.%	±0.0372%	M: FeK_α	312.63410
2	Ni	0.1 wt.%	±0.0052%	M: NiK_α	0.40497
3	Co	38.4 wt.%	±0.0260%	M: CoK_α	279.11786

TABLE 3. Analysis results of the composition of $FeFe_2O_4$ magnetic nanoparticles.

No.	Element	Content	Statistical Error	Spectral Line	Intensity [cps·μA^{-1}]
1	Fe	99.7 wt.%	±0.0478%	M: FeK_α	425.83336
2	Ni	0.1 wt.%	±0.0038%	M: NiK_α	0.31522
3	Co	0.2 wt.%	±0.0071%	M: CoK_α	1.71781

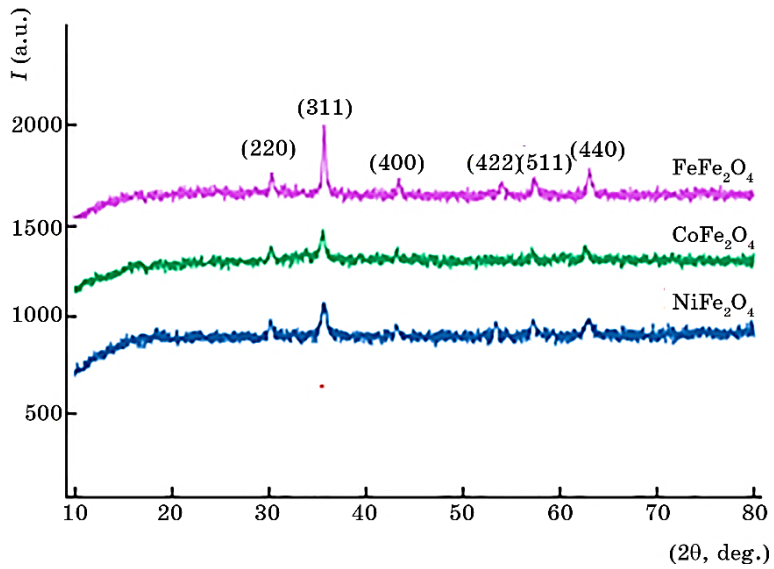

Fig. 4. X-ray diffraction of powdered $NiFe_2O_4$, $CoFe_2O_4$, and $FeFe_2O_4$ magnetic nanoparticles.

(220), (311), (400), (422), (511), and (400). The spectra of the diffracted x-rays indicate that all diffraction peaks for $NiFe_2O_4$, $CoFe_2O_4$, and $FeFe_2O_4$ magnetic nanoparticles correspond to a single-phase inverse cubic spinel structure, which is consistent with the results reported in scientific articles [3–7] (Fig. 4).

The average crystallite size of the $NiFe_2O_4$, $CoFe_2O_4$ and $FeFe_2O_4$ magnetic nanoparticles was estimated using the Debye–Scherrer equation from the most intense (311) diffraction peak in the x-ray diffraction (XRD) patterns:

$$D = \frac{0.89\lambda}{\beta\cos\theta}.$$

Here, λ is the wavelength of the x-ray radiation, β is the full width at half maximum (FWHM) of the spectral peak, and θ is the angle formed at the peak.

The lattice constants of $NiFe_2O_4$, $CoFe_2O_4$ and $FeFe_2O_4$ magnetic nanoparticles were determined using the following formula:

$$a = \sqrt{(h^2 + k^2 + l^2)d^2}\ .$$

Here, d is the distance between parallel planes, and h, k, l are the Miller's indices.

Additionally, the density of the nanoparticles was determined using

the following formula:

$$\rho = \frac{8M}{N_A a^3}.$$

Here, M represents the molecular weight of the magnetic nanoparticles, N_A is Avogadro's constant, and a is the crystal lattice parameter.

The particle size, lattice constant, and average density of the magnetic fluid particles, calculated using semi-empirical methods, are presented in Table 4 [4, 6, 9].

In this study, the composition of the magnetic fluids was formulated as follows:

1) $NiFe_2O_4$, $CoFe_2O_4$, and $FeFe_2O_4$ magnetic nanoparticles were used as the primary magnetic particles;

2) oleic acid ($C_{18}H_{34}O_2$) was employed as the surface-active agent;

3) distilled water was utilized as the liquid medium. Using these components, magnetic fluids with volumetric concentrations ranging from 0.5% to 5%, based on $NiFe_2O_4$, $CoFe_2O_4$, and $FeFe_2O_4$ magnetic nanoparticles, were prepared. Their electrical conductivity at room temperature was measured using the Karlaush method.

The magnetic fluids based on $NiFe_2O_4$, $CoFe_2O_4$, and $FeFe_2O_4$ magnetic nanoparticles investigated experimentally exhibit low electrical conductivity due to their predominantly dielectric nature. However, as the concentration of magnetic nanoparticles in these magnetic fluids increases, their electrical conductivity shows a significant rise. As observed from Fig. 5, the electrical conductivity of the prepared magnetic fluids at room temperature is as follows:

- for $FeFe_2O_4$-based magnetic fluid, with magnetic nanoparticle concentrations ranging from 0.5% to 5%, the electrical conductivity increased linearly from 15.6 μS/cm to 147.8 μS/cm;
- for $CoFe_2O_4$-based magnetic fluid, with magnetic nanoparticle concentrations ranging from 0.5% to 5%, the electrical conductivity increased linearly from 2.1 μS/cm to 20.2 μS/cm;
- for $NiFe_2O_4$-based magnetic fluid, with magnetic nanoparticle concentrations ranging from 0.5% to 5%, the electrical conductivity increased linearly from 0.23 μS/cm to 10.4 μS/cm.

The electrical conductivity of magnetic fluids is explained through

TABLE 4. Results of x-ray phase analysis of $NiFe_2O_4$, $CoFe_2O_4$, and $FeFe_2O_4$ magnetic nanoparticles.

Sample	D_{XRD} [nm]	a [Å]	a_{ave} [Å]	V [Å^3]	ρ_{XRD} [g·sm^{-3}]
$NiFe_2O_4$	16.9 ± 0.1	8.30		571.8	5.45
$CoFe_2O_4$	10.3 ± 0.1	8.37	8.47 ± 0.03	587.0	5.31
$FeFe_2O_4$	9.7 ± 0.1	8.73		598.0	5.28

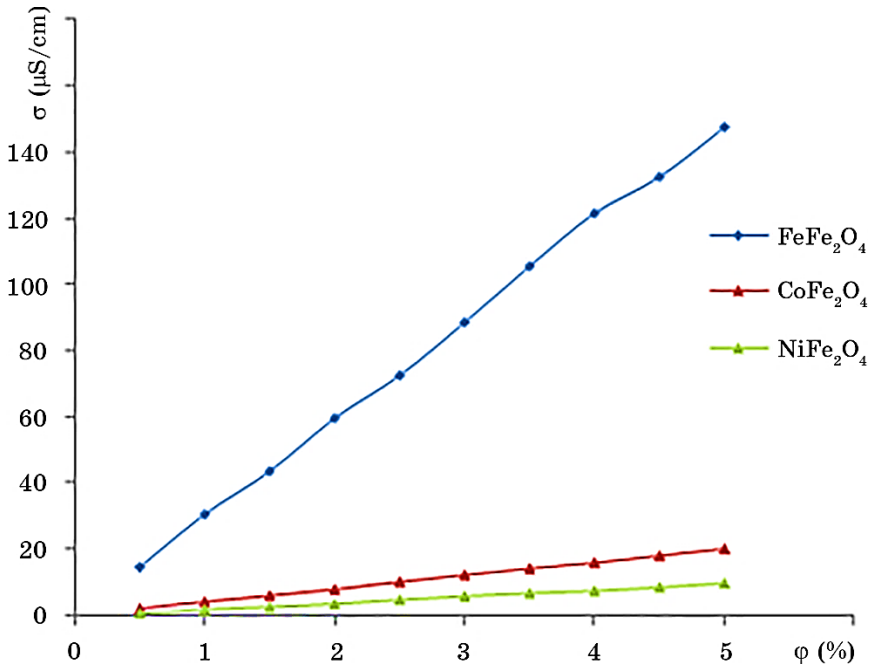

Fig. 5. Dependence of the electrical conductivity of magnetic fluids on concentration at room temperature.

an equation based on the Maxwell's model. However, for low-concentration magnetic fluids based on $NiFe_2O_4$, $CoFe_2O_4$, and $FeFe_2O_4$ magnetic nanoparticles, the enhanced Shen's model provides a more suitable explanation. According to this model, the following equation is formulated for low-concentration magnetic fluids: $\sigma = \sigma_M + \sigma_E + \sigma_B$. Here, σ_M represents the electrical conductivity calculated based on the Maxwell's model, σ_E denotes the electrical conductivity arising due to electrophoretic mobility, and σ_B indicates the electrical conductivity resulting from Brownian motion [11, 12].

4. CONCLUSIONS

$NiFe_2O_4$, $CoFe_2O_4$, and $FeFe_2O_4$ magnetic nanoparticles were synthesized *via* the chemical co-precipitation (chemical condensation) method. X-ray diffraction analysis confirmed that all diffraction peaks corresponded to a single-phase inverse cubic spinel structure for each composition, in agreement with previously reported literature data. Particle size estimation, based on transmission electron microscopy and the Debye–Scherrer equation, indicated average diameters of 25–38 nm for $NiFe_2O_4$, 10–30 nm for $CoFe_2O_4$, and 7–30 nm for $FeFe_2O_4$.

Electrical conductivity measurements at room temperature revealed the lowest value of 0.23 μS·cm^{-1} for the $NiFe_2O_4$-based magnetic fluid at 0.5% nanoparticles' concentration, and the highest value of 147.8 cm^{-1} for the $FeFe_2O_4$-based magnetic fluid at 5% concentration. These findings are consistent with predictions of the Shen's model.

AUTHORS' CONTRIBUTIONS

U. E. Nurimov carried out the experimental measurements, synthesized the magnetic nanoparticles, performed data processing, prepared the figures, and contributed to manuscript editing. O. Q. Quvondiqov conceptualized the research, supervised the study, developed the methodology, and conducted data analysis. Both authors discussed the results, contributed to the final version of the manuscript, and approved the submitted version.

REFERENCES

1. S. Mokhosi, W. Mdlalose, S. Mngadi, M. Singh, and T. Moyo, *Journal of Physics: Conference Series*, **1362**: 012104 (2019).
2. G. Asab, E. A. Zereffa, and T. A. Seghne, *Int. J. Biomaterials*, **2020**, No. 1: 4783612 (2020).
3. A. H. Oh, H.-Y. Park, Y.-G. Jung, S.-C. Choi, and G. S. An, *Ceramics International*, **46**, No. 8: 10723 (2020).
4. H. Moradmard, S. F. Shayesteh, P. Tohidi, Z. Abbas, and M. Khaleghi, *J. Alloys Compounds*, **649**: 116 (2015).
5. Z. Mahhouti, H. El Moussaoui, T. Mahfoud, M. Hamedoun, M. El Marssi, A. Lahmar, A. El Kenz, and A. Benyoussef, *J. Mater. Sci.: Materials in Electronics*, **30**, Iss. 16: 14913 (2019).
6. M. Abushad, M. Arshad, S. Naseem, H. Ahmed, A. Ansari, V.K. Chakradhary, S. Husain, and W. Khan, *Journal of Molecular Structure*, **1253**: 132205 (2022).
7. A. K. Sharma, A. K. Tiwari, and A. R. Dixit, *Materials and Manufacturing Processes*, **30**, No. 7: 813 (2015).
8. S. Halelfadl, P. Estellé, B. Aladag, N. Doner, and T. Maré, *Int. J. Therm. Sci.*, **71**: 111 (2013).
9. M. B. Javan, N. Tajabor, M. Behdani, and M. R. Rokn-Abadi, *Phys. B: Condensed Matter*, **405**, Iss. 24: 4937 (2010).
10. E. Scopel, P. P. Conti, D. G. Stroppa, and C. J. Dalmaschio, *SN Appl. Sci.*, **1**: 147 (2019).
11. J.-H. Lee, Y.-M. Huh, Y.-W. Jun, J.-W. Seo, J.-T. Jang, H.-T. Song, S. Kim, E.-J. Cho, H.-G. Yoon, J.-S. Suh, and J. Cheon, *Nature Medicine*, **13**, No. 1: 95 (2007).
12. M. F. Coelho, M. A. Rivas, G. Vilão, E. M. Nogueira, and T. P. Iglesias, *J. Chem. Thermodynamics*, **132**: 164 (2019).

Metallophysics and Advanced Technologies
Металофіз. новітні технол.
Metallofiz. Noveishie Tekhnol.
2026, vol. 48, No. 4, pp. 351–366
https://doi.org/10.15407/mfint.48.04.0351
Reprints available directly from the publisher

PACS numbers: 61.05.cp, 61.72.Ff, 68.35.Dv, 68.55.J-, 81.15.Gh, 81.65.Lp, 82.33.Ya

Features of the Formation of the Structure and Phase Composition of Modified Chrome PVD Coatings

E. P. Shtapenko, V. M. Nadtoka*, V. S. Krayeva*, and M. V. Krayev*

Ukrainian State University of Science and Technologies,
2 Lazariana Str.,
UA-49010 Dnipro, Ukraine
**Yuzhnoye State Design Office,*
3 Kryvorizka Str.,
UA-49008 Dnipro, Ukraine

The results of studies of the structure and phase composition of thick chromium coatings on the surface of the steel obtained by vacuum-arc deposition (arc-PVD) in an arc discharge and modified with nitrogen are presented. The modification is carried out directly in the process of vacuum-arc deposition in an argon-gas environment containing nitrogen. The features of the formation of the structure and phase composition of chromium coatings depending on the percentage of nitrogen in the chamber (from 20 to 100%) and the effect of the pulsed deposition mode at a fixed pressure value within the chamber ($(3–7)\cdot10^{-2}$ Pa) and substrate temperature (520–550°C) are established. The analysis of the studies shows that chromium coatings obtained in a steady-state mode in an argon environment (without nitrogen) have an open texture: in the cross section, the structure is columnar and coarse-crystalline, has an explicit relief surface with the release of fairly large pyramidal crystallites and a small droplet phase. The use of a pulsed deposition mode in an argon environment weakens significantly the texture of the coating, 'smooths' the surface with the formation of a fine-crystalline, close to globular coating structure. The introduction of nitrogen into the argon-gas environment changes the structure and phase composition of the coatings. With an increase

Corresponding author: Violeta Svyatoslavivna Krayeva
E-mail: kraevavioletta2020@gmail.com

Citation: E. P. Shtapenko, V. M. Nadtoka, V. S. Krayeva, and M. V. Krayev, Features of the Formation of the Structure and Phase Composition of Modified Chrome PVD Coatings, *Metallofiz. Noveishie Tekhnol.*, **48**, No. 4: 351–366 (2026). DOI: 10.15407/mfint.48.04.0351

in the percentage of nitrogen within the chamber, the structure of the coating in the cross-section changes from columnar coarse-crystalline to globular fine-crystalline, the lattice parameter and the size of the coherent-scattering region decrease, and the dislocation density increases. The introduction of nitrogen into the argon-gas environment leads to the formation of the hexagonal close-packed phase Cr_2N and the face-centred cubic phase CrN, the amounts of which depend on the deposition parameters. The use of a pulsed deposition mode, when modifying the coating with nitrogen, allows increasing the amount of nitrides in the coating compared to the steady-state mode.

Key words: arc-PVD, chromium coating, structure, phase composition, nitriding.

Представлено результати досліджень структури та фазового складу товстих хромових покриттів на поверхні криці, одержаних методою вакуумно-дугового осадження (arc-PVD) у дуговому розряді та модифікованих Нітроґеном. Модифікування проводилося безпосередньо в процесі вакуумно-дугового осадження в середовищі арґону, що містить азот. Встановлено особливості формування структури та фазового складу хромових покриттів залежно від відсотка Нітроґену у камері (від 20 до 100%) та впливу імпульсного режиму осадження за фіксованих значень тиску у камері ($(3–7)\cdot10^{-2}$ Па) та температури підкладинки (520–550°C). Аналіза досліджень показала, що хромові покриття, одержані за стаціонарного режиму в середовищі арґону (без азоту), мають яскраво виражену текстуру: у поперечному перерізі структура є стовпчастою, крупнокристалічною, має виражену рельєфну поверхню з виділенням достатньо великих пірамідальних кристалітів і дрібної крапельної фази. Використання імпульсного режиму осадження в середовищі арґону значно послаблює текстуру покриття, «згладжує» поверхню з утворенням дрібнокристалічної, близької до ґлобулярної структури покриття. Введення азоту в середовище арґону змінює структуру та фазовий склад покриттів. Зі збільшенням відсотка Нітроґену у камері структура покриття в поперечному перерізі змінюється від стовпчастої крупнокристалічної до ґлобулярної дрібнокристалічної, зменшуються параметр кристалічних ґратниць і розмір области когерентного розсіювання, а густина дислокацій збільшується. Введення азоту в середовище арґону приводить до утворення гексагональної щільноупакованої фази Cr_2N і гранецентрованої кубічної фази CrN, кількість яких залежить від параметрів осадження. Використання імпульсного режиму осадження під час модифікування покриття Нітроґеном уможливлює збільшити кількість нітридів у покритті порівняно зі стаціонарним режимом.

Ключові слова: електродугове нанесення покриття фізичним осадженням парів, хромове покриття, структура, фазовий склад, азотування.

(Received 2 May, 2025; in final version, 15 October, 2026)

1. INTRODUCTION

Thick chromium-based coatings are widely used as protective coatings:

as corrosion-resistant, antifriction and wear-resistant coatings [1–6]. The galvanic method of applying thick chromium coatings has long been one of the most widely used. The advantages of this method include its technical simplicity and the ability to obtain fairly thick and hard coatings [7–8]; the disadvantages include poor adhesion and porosity of the coating. Galvanic production is one of the most dangerous in terms of emissions of harmful substances into the environment [9], therefore, interest in environmental friendly technologies for obtaining coatings, in particular PVD technologies, has recently increased. One of the types of PVD technologies that allow obtaining the sufficiently thick chromium-based coatings (more than 10 μm thick) is the deposition of coatings by condensation from the gas phase in a vacuum arc discharge (arc-PVD) [10–12]. The properties of coatings primarily depend on their structure and phase composition. Arc-PVD allows controlling the structure of the coating with technological process parameters and achieving high adhesion to the substrate [13–15]. Having a number of advantages over galvanic coatings, PVD chrome coatings are still inferior to them in hardness. One of the ways to improve the mechanical characteristics of chrome PVD coatings is to modify them with nitrogen. Chromium nitrides can be classified as one of the most popular materials used in surface engineering. This is primarily due to the fact that they are characterized by very good tribological and mechanical properties [16, 17]. Compared to titanium nitrides, chromium nitride coatings have lower thermal conductivity, greater resistance to oxidation at high temperatures and greater plasticity, and have good corrosion and chemical resistance [18, 19]. Studies [20–25] have shown that the properties of Cr–N coatings are fundamentally determined by their structure and phase composition. Thus, expanding knowledge about the patterns of formation of the structure and phase composition of chromium coatings depending on the parameters of vacuum-arc deposition is relevant.

2. MATERIALS AND METHODS

Vacuum-arc deposition was carried out in a specialized vacuum plant with an end-face electric arc evaporator of metals. The cathode was made of chromium in the form of a cylinder with a diameter of 50 mm. The coatings were deposited on flat samples made of 38ХН3МФА (analogue 34NiCrMoV14-5) steel. Before applying the coating, chemical and mechanical cleaning of the samples was carried out. The samples were located in a plane parallel to the end surface of the cathode at a distance of 120 mm. The air was pumped out of the chamber until a deep vacuum $P = 1.3 \cdot 10^{-2}–4 \cdot 10^{-3}$ Pa was achieved. After pumping out, the working gas (argon, argon + nitrogen or nitrogen depending on the technological process) was introduced into the vacuum chamber to a

pressure of $P = (5.3–6.7)\cdot10^{-2}$ Pa. The steady-state deposition mode was carried out at a constant arc burning current of 70 A, arc burning voltage of 30–40 V, without bias voltage on the cathode, and the substrate temperature of 520–550°C. The pulsed deposition mode consisted of alternating cycles of low bias voltage of 40 V on the substrate lasting 5 minutes with a short pulse of 400 V lasting 20 s. The discharge current, arc burning voltage, chamber pressure, and process temperature were maintained the same as in the steady-state deposition mode.

Metallographic studies of the surface and cross-section were carried out using a metallographic light microscope MIM-10 (magnification up to ×1200). The structure of the coating was revealed by electrolytic etching of the ground surface and cross-section of the coatings on an electrolytic polishing machine 'Electro-P' (DEVCO S.r.l) in a 10%-solution of oxalic acid.

X-ray diffraction analysis (XRD) was performed on a DRON-2 X-ray diffractometer in monochromatic CoK_α radiation with a wavelength of $\lambda = 1.7902$ Å. Chemical elements and phases were identified by comparing interplanar distances with the PCPDFWIN card index. The parameters of the crystal lattice, microstrains, and defect density were calculated using the Williamson–Hall method. The sizes of coherent scattering regions (CSRs) were determined using the Selyakov–Scherrer formula. The textured state was assessed by comparing the relative intensities of diffraction peaks with reference values.

3. RESEARCH RESULTS AND DISCUSSION

The influence of the percentage ratio of nitrogen and argon in the gas environment of the vacuum chamber, as well as the use of a pulsed deposition mode of the change in the structure and phase composition of vacuum-arc chromium coatings was studied. The surface of the chromium coating obtained in a steady-state deposition mode in a pure argon environment is relief with the release of fairly large pyramidal crystallites with transverse dimensions of 5–7 μm and droplet inclusions with a diameter of 2–3 μm (Fig. 1, *a*).

Figure 1, *b* shows the surface structure after electrolytic etching, *i.e.*, crystallites with a certain degree of faceting emerges on the surface, which indicate textured growth. The structure in the cross section is columnar with small inclusions of equiaxed crystals, which disrupt the characteristic normal growth of the coating (Fig. 1, *c*).

To describe the process of formation of the structure of ion-plasma coatings, various known models of structural zones (MSZ) are used [26, 27]. The variety of such models is great and each of the models takes into account different factors that influence the mechanism of the initial stages of coating formation and its evolution. The main such factors include: homologous temperature T_s/T_m (the ratio of the sub-

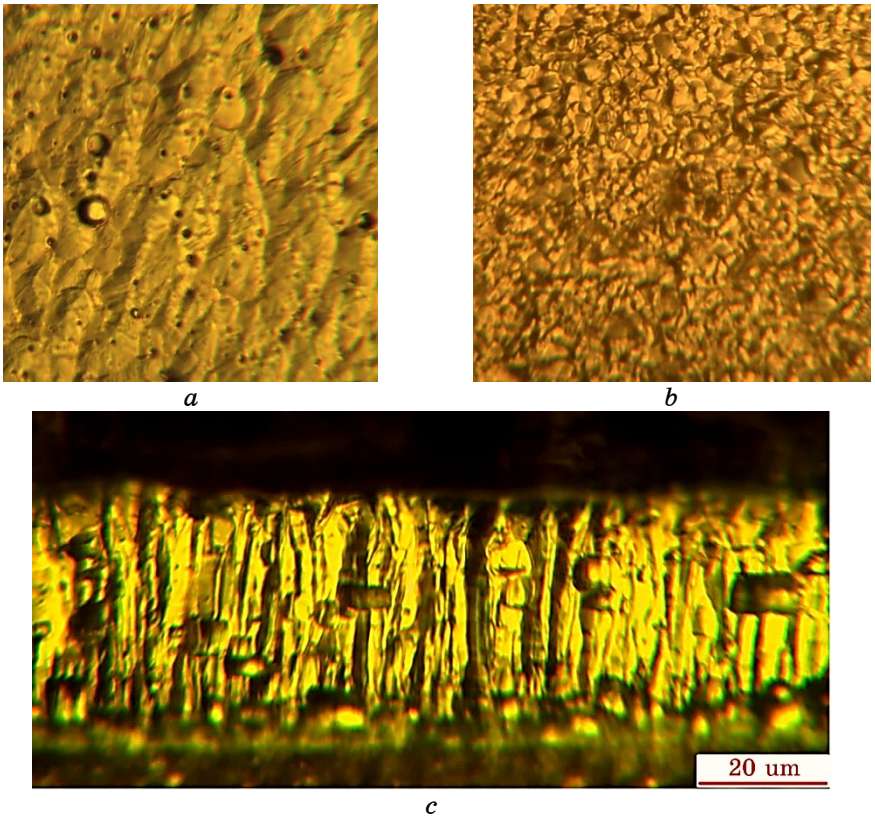

Fig. 1. Surface morphology (*a*), surface structure (*b*), cross-sectional structure (*c*) of the base chromium coating obtained in a steady-state deposition mode in a pure argon environment.

strate temperature to the melting point of the deposited coating material in kelvins), chamber pressure, arc burning current, substrate bias voltage, distance between the cathode and the substrate and their geometry, and impurity concentration in the chamber gas environment.

In this work, we investigated the effect of nitrogen concentration in the chamber on the coating formation process, so we chose the Barna and Adamik MSZ [28] (Fig. 2) as a basis, according to which an important role in the formation of the coating structure is played with the homologous temperature and the presence of active impurities that are released during the structuring and restructuring of the coatings.

In this study, the homologous deposition temperature fluctuated in a narrow range of $T_s/T_m \cong 0.36$–0.38, *i.e.*, was practically constant. The cross-sectional structure of the chromium coating obtained in the steady-state deposition mode in an argon environment (Fig. 1, *c*) correlates quite well with the structure similar to zone *3* (Fig. 2, *a*). At the

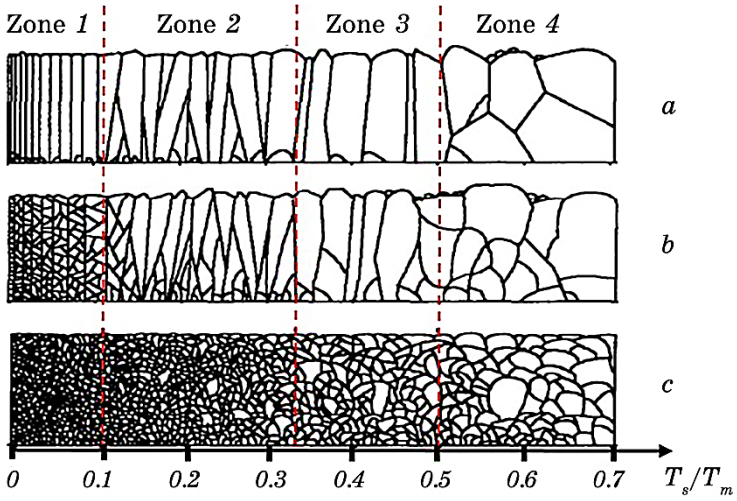

Fig. 2. Barna and Adamik MSZ: coating without impurity (base) (*a*), coating with impurity percentage of $\cong 1\%$ (*b*), coating with impurity percentage of $\geq 10\%$ (*c*).

substrate-coating interface, a transition layer is observed (Fig. 1, *c*), consisting of small misoriented crystallites.

The structure of the transition layer can be explained by the Stranski–Krastanov mechanism [29]. According to this mechanism, point nucleation centres are formed on the substrate, the rate of formation of which depends on the local temperature on the substrate, which then turn into two-dimensional islands, the growth rate of which depends on the surface diffusion of adatoms over the surface of the substrate. The relative rates of nucleation and formation of islands regulate the grain size before coalescence. At the initial stages of deposition, before coalescence, tangential growth predominates with the formation of equiaxed grains, and after coalescence, normal growth becomes predominant.

The introduction of nitrogen into the chamber gas environment as an active impurity leads to a change in both the surface morphology and the cross-sectional structure of the chromium coatings. Figure 3 shows photographs of the morphology and surface structure of the chromium coating obtained in the steady-state deposition mode at the minimum (20%$N_2$80%Ar) and maximum (80%$N_2$20%Ar) percentage of nitrogen in the chamber gas environment.

As can be seen in Fig. 3, *a*, the surface of the coating deposited in a 20%$N_2$80%Ar gas mixture remains relief.

The crystallites emerging on the surface are smoothed and reduced to several microns. A subsequent increase in the nitrogen concentration in the chamber to 80%$N_2$20%Ar 'smooths' the coating surface

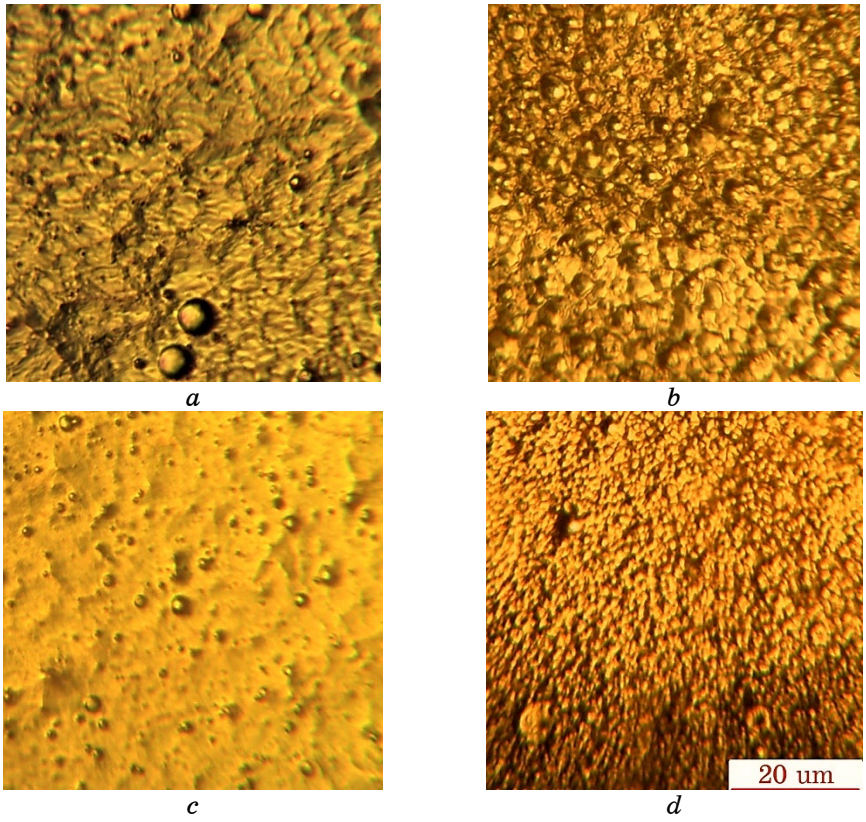

Fig. 3. Morphology and surface structure of chromium coatings obtained in a steady-state deposition mode in a nitrogen and argon environment with different percentage contents: 20%$N_2$80%Ar (*a*, *b*); 80%$N_2$20%Ar (*c*, *d*).

even more (Fig. 3, *c*). After electrolytic etching, globular elements are observed on the coating surface, the sizes of which decrease significantly with an increase in the nitrogen concentration in the chamber (Fig. 3, *b*, *d*).

According to the Barna and Adamik MSZ, the addition of impurities changes the coating structure. At low impurity concentrations (~ 1%), it accumulates predominantly at the grain boundaries during coating formation, resulting in a bimodal grain size distribution of the developing columnar structure; the diameter of the developing columns in zone *3* becomes smaller (Fig. 2, *b*) than in the base coating (Fig. 2, *a*). The texture, with minimized surface energy and interfacial energy, is not as explicit as in the base coating. With increasing impurity concentration, impurity segregation due to grain boundary motion becomes effective, resulting in complete coverage of the forming crystallite surface with a passivating layer and the development of three-

dimensional grains (Fig. 2, *c*), which are separated by stabilized grain boundaries. The impurity-stabilized grain size distribution is bimodal.

Similar conditions, in our opinion, are realized in this study during the deposition of chromium in the reaction gas nitrogen environment. Nitrogen ions, combining with chromium ions in the plasma volume, form nitrides, which act as impurities passivating the normal growth of crystallites, as evidenced by the structure of the coating in the cross section in Fig. 4.

The coating deposited from the 20%$N_2$80%Ar gas mixture is still characterized by a columnar structure interrupted by equiaxed grains (Fig. 4, *a*), but the diameter of the columns is significantly smaller than for the base coating (Fig. 1, *c*). With an increase in the nitrogen concentration in the chamber to 40%$N_2$60%Ar, the effect of suppressing columnar growth increases, globular grains with a disordered ori-

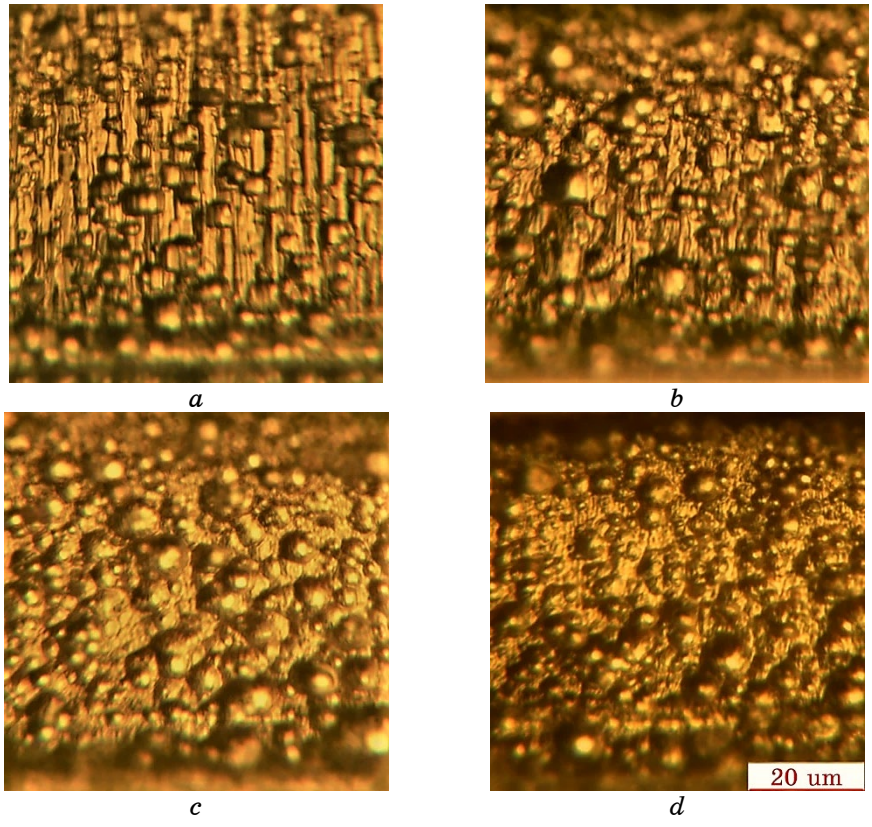

Fig. 4. The cross-sectional structure of chromium coatings obtained in a steady-state deposition mode in a nitrogen and argon environment with different percentage contents: 20%$N_2$80%Ar (*a*), 40%$N_2$60%Ar (*b*), 60%$N_2$20%Ar (*c*), 80%$N_2$20%Ar (*d*).

entation are formed (Fig. 4, *b*). A subsequent increase in the nitrogen concentration in the chamber gas mixture in the range of 60–80%N_2 completely disrupts the columnar growth of the coating and creates conditions for the formation of a globular structure and a decrease in the crystallite sizes (Fig. 4, *c*, *d*).

The study of coatings obtained in the steady-state deposition mode at 100%N_2 in the chamber showed a very low quality of such coatings. The coatings are friable, porous, and, during the study, they delaminate in planes parallel to the substrate, so they were of no interest for their further study. In the second stage of the study on the effect of deposition parameters on the structure and phase composition of chromium coatings, it was found that the use of pulsed deposition modes also allows one to 'escape' from the classical columnar structure of chromium condensates.

Figure 5 shows photographs of the surface morphology and structure of chromium coatings deposited in a pure argon environment in a pulsed mode.

Comparing the surface morphology of the chromium coating obtained in an argon environment in a steady-state mode (Fig. 1, *a*) and in a pulsed mode (Fig. 5, *a*), it is evident that the pulsed mode significantly smooths and refines the surface structure. After electrolytic etching, the release of small faceted crystallites is observed on the surface of the coating (Fig. 5, *b*). The cross-sectional structure (Fig. 5, *c*) is similar to the structure obtained in a steady-state mode with the addition of 40–60% nitrogen to the chamber, and consists of thin columns interrupted by globular grains.

Thus, the pulse mode plays the role of a passivating factor, similar to the effect of impurities during deposition in a nitrogen environment, which disrupts the columnar textured growth of the chromium coating.

Adding nitrogen to the chamber during the pulsed deposition mode leads to an effect similar to that for the steady-state mode—the surface morphology becomes smoothed cellular (Fig. 6, *a*), the surface structure is globular fine-grained (Fig. 6, *b*), in the cross section the structure is globular (Fig. 6, *c*). Increasing the nitrogen content to 80% leads to the formation of a layered structure (Fig. 6, *d*). The coating is very fragile, breaks down along the layer boundaries.

The results of XRD of chromium obtained in steady-state and pulsed deposition modes in an argon environment showed the presence of the body-centred cubic phase of Cr. Figure 7 shows the diffraction patterns of chromium coatings obtained in steady-state and pulsed deposition modes.

Analysis of the obtained data indicates the presence of a pronounced [200] texture in the chromium coating obtained in the steady-state mode.

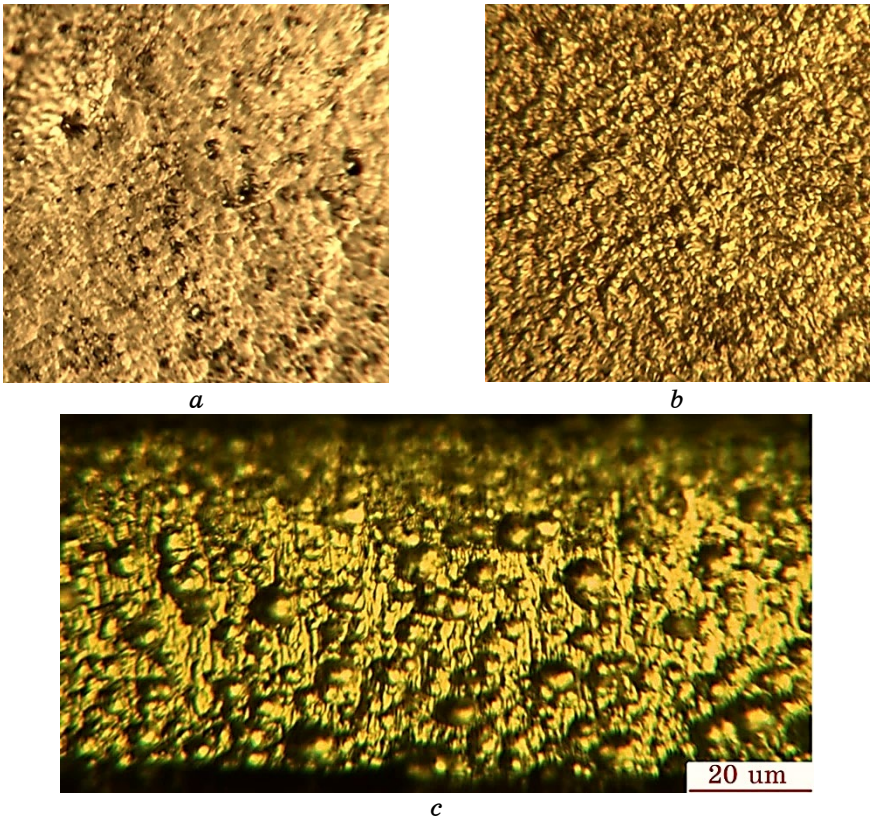

Fig. 5. Surface morphology (*a*), surface structure (*b*), cross-sectional structure (*c*) of a chromium coating obtained in a pulsed deposition mode in a pure argon environment.

The use of the pulsed mode leads to a redistribution of the intensities of the diffraction maxima, which can be used to estimate the weak [200] + [211] texture.

The lattice parameter as a result of the pulse mode decreases from 2.8985 to 2.8879 Å, which indicates the occurrence of compressing stresses. A finer crystalline and more defective structure is formed with a CSRs size of 1340 nm and a dislocation density of $9.51 \cdot 10^{10}$ cm^{-2} (for the steady-state mode, these parameters were equal to 1600 nm and $4.04 \cdot 10^{10}$ cm^{-2}, respectively). Thus, the use of the pulsed deposition mode leads to the suppression of textured growth and refinement of the chromium coating structure.

Adding nitrogen to the gas environment of the chamber led to a change in the microstructure, texture and phase composition of the coating of chromium coatings. Figure 8 shows the diffraction patterns

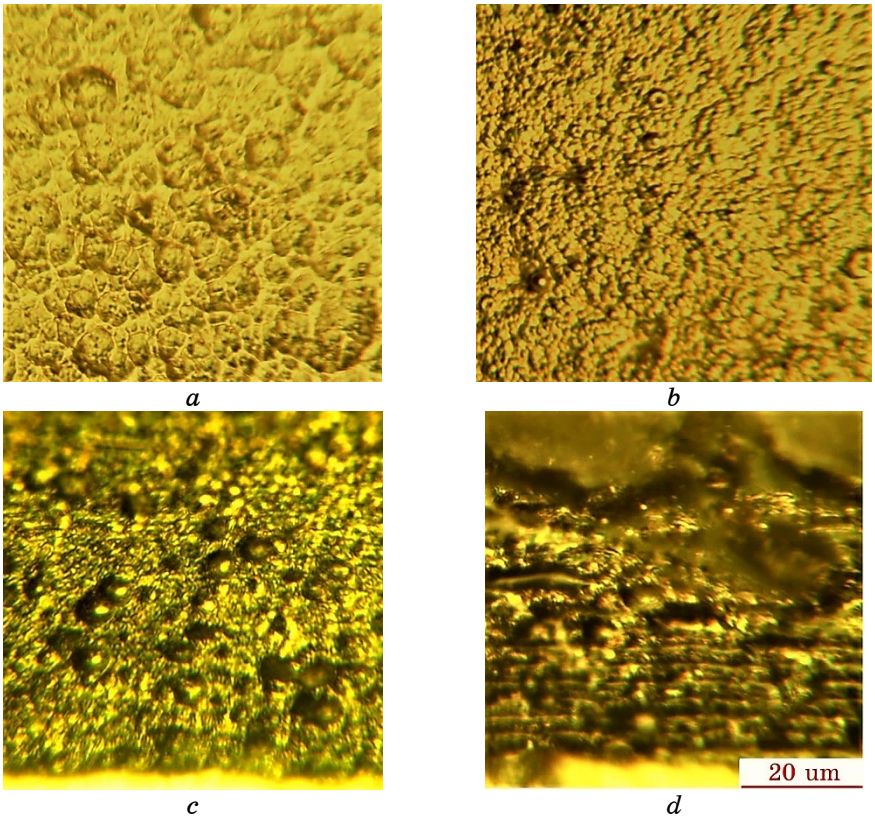

Fig. 6. Morphology (*a*), surface structure (*b*), cross-sectional structure (*c*) of a chromium coating obtained in the pulsed deposition mode in a gas environment of 60%$N_2$20%Ar and in a gas environment of 80%$N_2$20%Ar (*d*).

of chromium coatings modified with nitrogen. The texture of chromium modified with nitrogen in a steady-state mode at low nitrogen concentrations in the gas environment remains the same as for pure chromium: the most intense line remains (200). With increasing nitrogen concentration in the chamber, a redistribution of diffraction maximum occurs: the intensity of the maximum (200) decreases, while the maximum (110) and (211) are enhanced, which is associated with passivation of the surface of growing crystals by chromium nitrides. Phase XRD showed that modification of chromium with nitrogen leads to the formation of two chromium nitrides—Cr_2N with an hcp lattice and CrN with an f.c.c. lattice.

When modifying chromium with nitrogen in a steady-state mode in a chamber gas environment with a nitrogen percentage of less than 40%, chromium nitrides are practically not formed (< 1%). Increasing the nitrogen percentage in the chamber to more than 60% leads to an

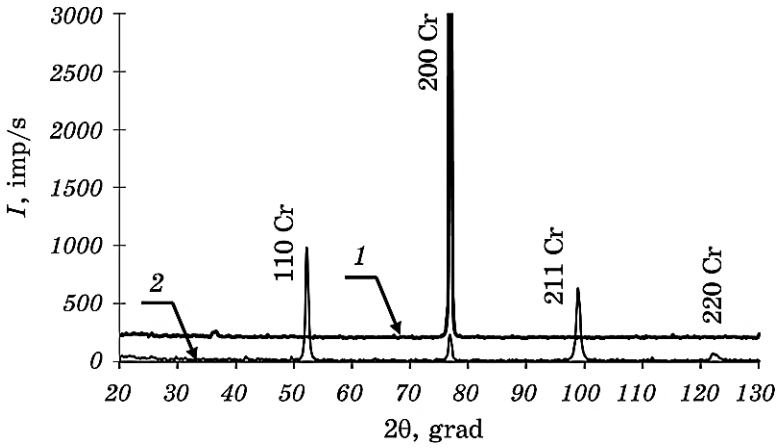

Fig. 7. Diffraction patterns of chromium coatings obtained in a steady-state deposition mode (*1*) and in a pulsed mode (*2*) in an argon gas environment.

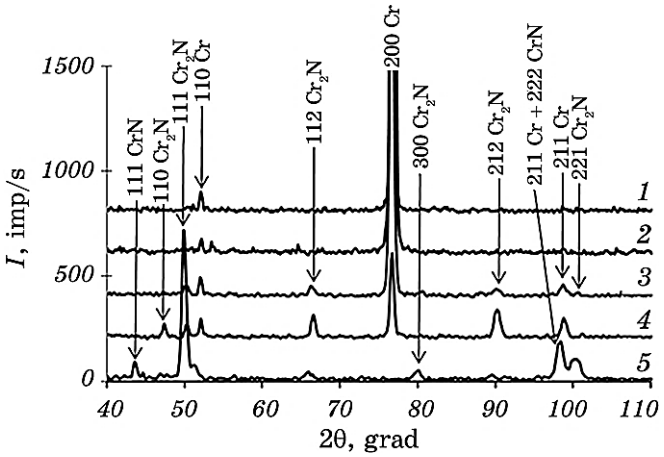

Fig. 8. Diffraction patterns of chromium coatings obtained in a steady-state deposition mode in a gas environment with different percentages of nitrogen: 20%$N_2$80%Ar (*1*); 40%$N_2$60%Ar (*2*); 60%$N_2$40%Ar (*3*); 80%$N_2$20%Ar (*4*); 100%N_2 (*5*).

increase for the amount of chromium nitride Cr_2N, reaching its maximum amount at content of 100% N_2 in the chamber (Table 1). Chromium nitride CrN is formed in a steady-state mode in a small amount (up to 8%) only at the maximum nitrogen content in the chamber.

The pulsed deposition mode intensifies the process of chromium modification with nitrogen. Figure 9 shows the diffraction patterns of chromium coatings modified with nitrogen in the pulsed mode at

TABLE 1. Microstructure and phase composition of chromium coatings under different deposition conditions.

Deposition conditions	Composition of the gas environment	Cr_2N, %	CrN, %	a, Å	L, nm	$D\times10^{10}$, cm^{-2}
Steady-state mode	100%Ar	–	–	2.8985	1600	4.04
Modification with nitrogen in steady-state mode	20%$N_2$80%Ar	0.5	–	2.8825	1100	7.72
	40%$N_2$60%Ar	0.5	–	2.8825	1050	8.64
	60%$N_2$40%Ar	8	–	2.8870	950	9.77
	80%$N_2$20%Ar	34	–	2.8889	920	10.59
	100%N_2	78	8	2.8988	570	38.5
Modification in pulse mode	100%Ar	–	–	2.8879	1340	9.51
	60%$N_2$40%Ar	55	29	2.8880	700	34.0
	80%$N_2$20%Ar	70	25	2.8988	520	39

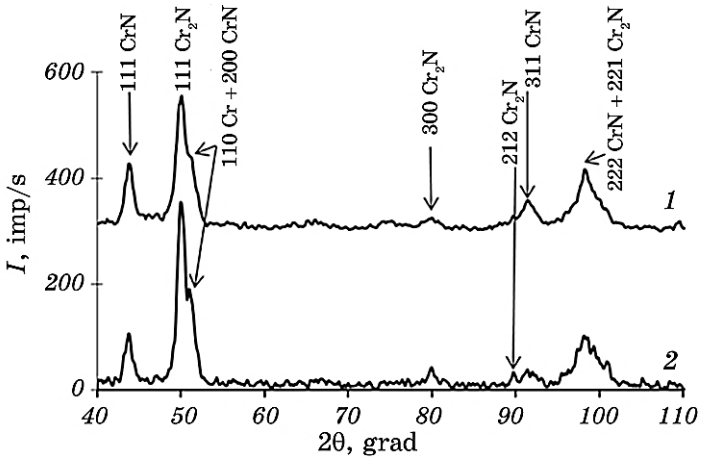

Fig. 9. Diffraction patterns of nitrogen-modified chromium coatings in pulse mode: 60%$N_2$40%Ar (*1*), 80%$N_2$20%Ar (*2*).

60%$N_2$40%Ar and 80%$N_2$20%Ar in the chamber. The use of the pulsed mode with a content of 60%$N_2$40%Ar in the chamber leads to a significant increase for the amount of Cr_2N and CrN nitrides compared to the steady-state mode (Table 1). This effect can be associated with the action of a short pulse with the supply a high bias voltage, which enhances the ionization of nitrogen atoms and intensifies the formation of nitrides.

The studies of the coating microstructure showed that the nitrogen-modified chromium coatings become more fine-crystalline and more

defective. The results of calculations of the lattice parameter, the sizes of the CSRs and the dislocation density are presented in Table 1. The values of the lattice parameter of chromium obtained in a gas environment with the addition of nitrogen are smaller than those for a pure chromium coating that indicates compressing stresses. With an increase in the percentage of nitrogen in the chamber, the lattice parameter increases and reaches its highest value at 100% N_2 in the chamber in the steady-state mode and 80%$N_2$20%Ar in the pulsed mode, which may indicate the introduction of nitrogen atoms into the chromium lattice. An increase in the percentage of nitrogen in the gas environment of the chamber leads to a decrease in the size of the CSRs and an increase in the dislocation density.

Thus, by varying the nitrogen content in the nitrogen-argon gas mixture in the chamber and the deposition modes, it is possible to control the structure and phase composition of chromium coatings during their arc-PVD.

4. CONCLUSIONS

The work establishes the patterns of formation of the structure and phase composition of chromium coatings obtained by arc-PVD in an argon-nitrogen gas environment, on the basis of which the following conclusions can be made:

– the coating obtained in the steady-state deposition mode in an argon environment has a columnar coarse-crystalline structure with a CSRs size of 1600 nm and an explicit texture [200];

– the use of a pulsed deposition mode in an argon environment significantly weakens the degree of texture, reduces the CSRs size to 1340 nm and disrupts the columnar growth of the coating with a transition to a columnar-globular structure;

– an increase in the percentage of nitrogen in the gas mixture in the chamber under steady-state deposition conditions helps to reduce the CSRs size from 1100 nm to 920 nm, increase the density of dislocations, and change the structure of the coating from columnar to globular;

– modification of the chromium coating with nitrogen in the steady-state deposition mode leads to the formation of 8% Cr_2N at a content of 60%$N_2$40%Ar in the chamber to 34% Cr_2N at 80%$N_2$20%Ar in the chamber;

– the use of pulse mode during modification with nitrogen helps to increase the amount of nitrides in the coating from 55% Cr_2N and 29% CrN with a content of 60%$N_2$40%Ar in the chamber to 70% Cr_2N and 25% CrN with 80%$N_2$20%Ar in the chamber;

– coatings obtained in an environment of 100% N_2 have unsatisfactory quality: non-uniform in thickness, brittle, delaminated in planes par-

allel to the substrate.

The established patterns of the structure and phase composition of modified chromium coatings can be used to predict their mechanical properties and to build models of structural zones.

This work was supported by the National Research Foundation of Ukraine (NRFU) under the project "Research for Strengthening the Defense Capacity and National Security of Ukraine", Project Registration No. 2025.06/0084.

AUTHORS' CONTRIBUTIONS

E. P. Shtapenko supervised the project, developed the concept, formulated the main objective of the study, and performed the overall analysis of the results. V. M. Nadtoka conducted the literature review, collected data on the methods of preparation and physical properties of modified chromium coatings, supervised the progress of the work, and wrote Sec. 1 'Introduction' of the manuscript. M. V. Krayev planned the experimental part of the study, developed the vacuum-arc deposition regimes for nitrogen-modified chromium coatings, and wrote Sec. 2 'Materials and Methods' of the manuscript. V. S. Krayeva carried out the experimental investigation and analysis of the structure and phase composition of the obtained coatings and wrote Sec. 3 'Results and Discussion' of the manuscript.

REFERENCES

1. V. M. Nadtoka, R. V. Pankov, Z. Stadomski, and O. G. Lytvinenko, *Wiad. Hutn.*, **80**, No. 5: 355 (2013).
2. R. V. Pankov, V. M. Nadtoka, N. V. Masljanyj, and L. N. Dejneko, *Visn. Dnipropetr. Univ. Ser. Fiz. Radioelektron.*, **19**, No. 2: 106 (2012) (in Ukrainian).
3. D. B. Hlushkova, V. M. Volchuk, P. M. Polyansky, V. A. Saenko, and A. A. Efimenko, *Funct. Mater.*, **30**, No. 2: 275 (2023) (in Ukrainian).
4. O. D. Sokolov and O. V. Mannapova, *Scientific Works Odessa National Academy of Food Technologies*, **42**, No. 2: 520 (2012) (in Ukrainian).
5. R. Saydakhmedov and G. Saydakhmedova, *Acta Period. Technol.*, **55**: 133 (2024).
6. A. S. Kuprin, V. A. Belous, V. V. Bryk, R. L. Vasilenko, V. N. Voyevodin, V. D. Ovcharenko, G. N. Tolmachova, I. V. Kolodiy, V. M. Lunyov, and I. O. Klimenko, *PAST*, **96**, No. 2: 111 (2015) (in Russian).
7. D. Chen, H. Daoud, T. Dörflinger, P. Näser, U. Smuda, J. Herlan, and U. Glatzel, *Surf. Coat. Technol.*, **455**: 129178 (2023).
8. V. Protsenko, L. Bobrova, and F. Danilov, *Anti-Corros. Methods Mater.*, **65**, No. 5: 499 (2018).
9. C. D. Muller, S. C. Garcia, N. Brucker, G. Goethel, E. Sauer, L. M. Lacerda, and L. R. Feksa, *Drug Chem. Toxicol.*, **45**, No. 2: 560 (2020).
10. X. L. Pinheiro, K. Oliveira, J. Santos, A. V. Girão, A. C. Bastos, M. Sousa,

D. Baptista, S. Gomes, R. Lobo, P. Oliveira, A. Monteiro, J. P. Teixeira, M. Monteiro, and P. A. Fernandes, *Process Saf. Environ. Prot.*, **182**: 727 (2024).
11. Y. Y. Aksenov, A. A. Andreev, V. L. Belous, V. E. Strel'nyckyj, and V. M. Horoshyh, *Vakuumnaya Duga* [Vacuum Arc] (Kiev: Naukova Dumka: 2012) (in Russian).
12. E. V. Ovchinnikov, N. M. Chekan, G. A. Kostyukovich, and D. S. Kalynov, *Mezhdunarodnyi Nauchno-Issledovatel'skiy Zhurnal*, **112**, No. 10: 23 (2021) (in Russian).
13. I. V. Serdiuk, S. I. Petrushenko, V. O. Stolbovyi, and M. Fijalkowski, *Metallofiz. Noveishie Tekhnol.*, **46**, No. 1: 23 (2024).
14. A. V. Kolubaev, O. V. Sizova, Y. A. Denisova, A. A. Leonov, N. V. Teryukalova, O. S. Novitskaya, and A. V. Byeli, *Fiz. Mezomekh.*, **25**: No. 2, 35 (2022) (in Russian).
15. M. J. M. Jimenez, V. Antunes, S. Cucatti, A. Riul Jr, L. F. Zagonel, C. A. Figueroab, D. Wisnivesky, and F. Alvarez, *Surf. Coat. Technol.*, **372**: 268 (2019).
16. J. Stallard, S. Poulat, and D. G. Teer, *Tribology and Interface Engineering Series* (Ed. Sujeet Sinha) (Elsevier: 2006), Vol. **51**, Ch. 13, p. 250.
17. D. B. Lee, Y. C. Lee, and S. C. Kwon, *Surf. Coat. Technol.*, **141**: 232 (2001).
18. E. Lugscheider, K. Bobzin, St. Bärwulf, and Th. Hornig, *Surf. Coat. Technol.*, **133–134**: 540 (2000).
19. G. Bertrand, H. Mahdjoub, and C. Meunier, *Surf. Coat. Technol.*, **126**, Iss. 2–3: 199 (2000).
20. A. G. Guglja and I. M. Nekljudov, *Usp. Fiz. Met.*, **6**: 197 (2005) (in Russian).
21. M. Ghoranneviss, Amir H. Sari, M. Esmaeelpour, M. R. Hantehzadeh, and H. Savaloni, *Appl. Surf. Sci.*, **237**: 326 (2004).
22. G. G. Fuentes, R. Rodriguez, J. C. Avelar-Batista, J. Housden, F. Montala, L. J. Carreras, A. B. Crist'obal, J. J. Damborenea, and T. J. Tate, *J. Mater. Process. Technol.*, **167**: 415 (2005).
23. M. Manouchehrian, M. M. Larijani, and B. Banagar, *Int. J. Thin Fil. Sci. Tec.*, **3**, No. 2: 67 (2014).
24. J. Smolik et Zbigniew Słomka, D. Pać k, and P. Hermanowicz, *Maintenance Problems*, **4**: 91 (2006).
25. J. J. Olaya, S. E. Rodil, S. Muhl, L. Huerta, *Surf. Coat. Technol.*, **200**: 5743 (2006).
26. A. L. Kameneva, *Evolyutsiya Predstavleniy o Strukturnykh Zonakh Polikristallicheskikh Nanostrukturirovannykh Plenok, Formiruemykh Metodami Vakuumnykh Tekhnologiy* [Evolution of Ideas about Structural Zones of Polycrystalline Nanostructured Films Formed by Vacuum Technology Methods] (Perm': 2012) (in Russian).
27. I. I. Aksenov and D. S. Aksyonov, *East Eur. J. Phys*, **1**, No. 3: 22 (2014) (in Russian).
28. P. B. Barna and M. Adamik, *Thin Solid Films*, **317**: 27 (1998).
29. I. M. Stranski and L. Krastanow, *Sitz Berl. Akod Wiss.*, **146**: 797 (1938).

Metallophysics and Advanced Technologies
Металофіз. новітні технол.
Metallofiz. Noveishie Tekhnol.
2026, vol. 48, No. 4, pp. 367–382
https://doi.org/10.15407/mfint.48.04.0367
Reprints available directly from the publisher

PACS numbers: 61.43.Dq, 61.72.Dd, 61.72.Ff, 62.20.fg, 65.60.+a, 81.05.Bx, 81.30.Kf

Structure and Properties of Heat-Treated $(TiHf)_{50}(NiCu)_{50}$ Alloys

N. A. Gurbanov[*], H. A. Ahlatci[**], K. H. Ismayilova[*], and Y. A. Abdulazimova[***]

[*]*Azerbaijan State Oil and Industry University,*
16/21 Azadlig Ave.,
AZ-1010 Baku, Azerbaijan
[**]*Karabük University,*
Kılavuzlar, 413. Sokak No: 10.,
TR-78050 Merkez/Karabük, Turkey
[***]*Baku Engineering University,*
120 Hasan Aliyev Ave.,
AZ-0101 Khirdalan, Azerbaijan

Shape-memory alloys are metallic smart materials, which can recover their original shape after deformation and primarily consist of two main solid phases. This study develops physical principles for selecting chemical compositions for quaternary alloys with shape-memory effects and other functional properties obtained using conventional and unconventional technologies. Studies on the $(TiHf)_{50}(NiCu)_{50}$ system obtained by rapid cooling have revealed that amorphous–crystalline or completely amorphous phases can form, depending on the composition. Furthermore, it is determined that the martensitic-transformation temperature, which depends on copper concentration in the alloys, does not change in rapidly cooled strip samples.

Key words: shape-memory alloy, sheet metal, planar flow casting, amorphous structure, enthalpy of mixing.

Стопи з пам'яттю форми — це металеві «розумні» матеріяли, які можуть відновлювати свою початкову форму після деформації та переважно

Corresponding author: Nurlan Gurbanov
E-mail: nurlan.gurbanov@asoiu.edu.az

Citation: N. A. Gurbanov, H. A. Ahlatci, K. H. Ismayilova, and Y. A. Abdulazimova, Structure and Properties of Heat-Treated $(TiHf)_{50}(NiCu)_{50}$ Alloys, *Metallofiz. Noveishie Tekhnol.*, **48**, No. 4: 367–382 (2026), DOI: 10.15407/mfint.48.04.0367

складаються з двох основних твердих фаз. У цьому дослідженні розроблено фізичні принципи вибору хемічного складу для чотирокомпонентних стопів з ефектами пам'яті форми й іншими функціональними властивостями, одержаними за допомогою традиційних і нетрадиційних технологій. Дослідження системи $(TiHf)_{50}(NiCu)_{50}$, одержаної швидким охолодженням, показали, що, залежно від складу, можуть утворюватися аморфно-кристалічні або повністю аморфні фази. Крім того, було встановлено, що температура мартенситного перетворення, яка залежить від концентрації Купруму у стопах, не змінюється у швидкоохолоджених зразках стрічки.

Ключові слова: стоп з пам'яттю форми, листовий метал, лиття планарним потоком, аморфна структура, ентальпія змішання.

(Received 18 November, 2025; in final version, 15 December, 2025)

1. INTRODUCTION

Today, technology is rapidly evolving to meet increasing needs. This rapidly advancing technology brings with it new generations of materials and instruments.

In addition to the physical properties of materials, different types of materials with different functionalities have been developed today [1]. High functionality can be achieved by controlling and monitoring the micro-level movements of smart materials, which are products of advanced technology, and by changing their internal structures in response to environmental effects [2, 3]. One of the most functional structures among smart metals is the shape-memory alloy [4]. Shape-memory alloys are defined by the ability of the material to return to its original shape, usually by heating, after severe deformations that occur at relatively low temperatures [3, 5, 6]. The shape-memory effect in shape-memory alloys is due largely to the solid–solid diffusionless thermoelastic martensitic transformation between cubic $B2$ austenite and monoclinic $B19'$ martensite phases [4, 7].

How $B2$ austenite transforms into $B19'$ martensite and how twinning occurs during the martensitic transformation, it has been investigated using atomistic simulations [8]. It is observed that when martensite grains nucleate within austenite, they form a twin relationship as a natural consequence of the crystal structure (Fig. 1). Atomic mixing is all that is required for the lattice transformation and twinning, and since the twinning plane cannot be kept fixed during the lattice transformation, no homogeneous slip occurs on the twinning plane. In this case, the twinning mechanism does not involve dislocations, and it is possible to achieve thermoelastic martensitic transformation.

The thermoelasticity of the transformation arises from the material's ability to elastically accommodate the stresses caused by the

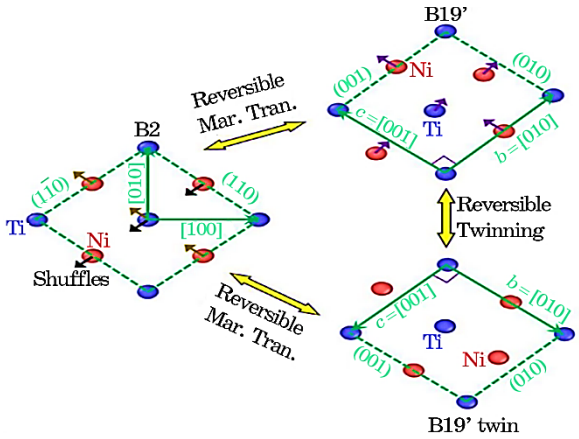

Fig. 1. Lattice transformations between *B*2, *B*19', and mirrored *B*19' [8].

volume change during the crystallographic rearrangement of different phases [5, 8]. As a general rule, the volume effect during thermoelastic martensitic transformation is very small (< 1%), which allows the consistency of the austenite/martensite interfaces to be maintained during the transformation [9]. The kinetic parameters of the thermoelastic martensitic transformation in shape-memory alloys can be followed by different kinetic models [10]. Common models for the simultaneous study of martensitic transformation are the Flynn–Wall–Ozawa and Kissinger models. The Kissinger approach determines a specific activation energy and thermal activation required for the transformation as a result of the effect of the heating/cooling rate on the reaction [4, 11]. The Ozawa approach is very similar to the Kissinger approach except that the reaction order is not affected by the heating/cooling rate [12].

Nanoscale precipitates are used in shape-memory alloys to tailor thermoelastic martensitic transformations [13]. These precipitates significantly affect the thermoelastic martensitic-transformation properties by introducing concentration heterogeneity, coherent stress field and geometric confinement in the parent phase [1, 14].

Among the shape-memory alloys, NiTi alloys stand out due to their good functional and mechanical properties such as ductility, fatigue strength, deformation rate [8, 9]. Today, NiTi alloys constitute the majority of shape-memory alloys used practically in industry, especially in biomedical fields [11]. However, since the transformation temperatures of NiTi alloys are below 100°C, their use is limited in areas requiring high temperatures such as aerospace, automobile and petroleum industries [15]. Therefore, researchers are working on developing materials with transformation temperatures above 100°C [16]. The most important alloy systems emphasized in the studies are the mate-

rials obtained by increasing the transformation temperatures of these alloys by alloying and precipitation formation methods using the NiTi binary alloy system as a base [17, 18]. Thus, the good properties of Ni-Ti alloys are utilized and alloys that can exhibit phase transformation at high temperatures can be obtained [19, 20]. One of the most important methods used for this purpose is alloying [16].

When combining NiTi binary alloys with a third alloying element, both the transformation temperatures of these alloys can be increased and some mechanical properties can be improved [4, 12–14]. With the changes made, it has been observed that the transformation temperatures of the elements V, Fe, Al, Mn, Cu, and Co added as third alloying elements decrease, while the phase transformation temperatures of Hf, Zr, Pt, Au, and Pd increase [15, 21]. Because Au, Pt, and Pd are very expensive, among these elements, which increase the phase-transformation temperatures, researchers have focused mostly on Hf and Zr [2, 4, 9]. Among these two elements, it has been determined that Hf is more preferred than Zr in terms of ductility, work production capacity, and cost [12–15, 21]. Moreover, the phase transformation temperatures of NiTiHf alloys can be adjusted between 100–300°C. The transformation temperatures of NiTiHf alloys do not increase negligibly up to 10% Hf content. However, it increases rapidly after 10% Hf addition and when the Hf ratio is 30%, the phase transformation temperatures continue above 500°C [9, 21].

The main disadvantages of NiTiHf alloys with low Ni content can be listed as low ductility, high thermal hysteresis (> 50°C) and low strength. Various studies have been carried out to increase the strength of these alloys [22]. One of these is to increase the strength by means of high deformation and the dislocations formed in the microstructure as a result [23]. As a result of these studies, it has been observed that the reversible deformation obtained increases and the thermal hysteresis values decrease [21–23]. Another method for improving the properties of NiTiHf alloys is precipitation hardening. This method is one of the methods that have been successful in increasing the strength. Studies have increased the strength and improved the functional properties of NiTiHf alloys by precipitation hardening [24–25].

Kollerov *et al.* [26] investigated a titanium–nickelide alloy alloyed with up to 1% Co, Cr, and Fe, up to 3% V, and up to 8% Nb. Kolomytsev *et al.* [27] investigated the effects of Fe, Al, and Cu on phase transformations in TiNi alloys.

Most metallic materials used in practice are not in complete thermodynamic equilibrium, corresponding to the maximum free energy. Obtaining alloys in a metastable state is considered an effective approach to ensure their physicochemical properties [4, 10, 28]. It is known that upon cooling below the melting temperature (T_m), the alloy either

transforms into an amorphous state or crystallizes. When crystallization occurs, the viscosity, volume, and internal energy change abruptly. If crystallization can be prevented, these properties change continuously and rapidly with temperature [2, 10, 14]. The crystallization kinetics of amorphous alloys is determined by the combined effects of thermodynamic factors and kinetic parameters [28–31].

Research has shown that the strengthening of the TiNi compound cannot be achieved sufficiently by alloying alone [16, 20–25].

This work offers a thorough thermodynamic–structural correlation for the quaternary $(TiHf)_{50}(NiCu)_{50}$ system created by planar flow casting under rapid cooling, in contrast to earlier research that focused exclusively on NiTiHf or NiTiCu systems. This study is noteworthy in that it demonstrates how differences in the enthalpy of mixing and amorphous phase stability produced by copper influence the behaviour of the martensitic transition following rapid quenching. Furthermore, the study develops a new framework for forecasting amorphous–crystalline transitions in multicomponent Ti-based shape-memory alloys by fusing theoretical modelling of mixing enthalpies (Ni–Ti *vs.* Ni–Hf subsystems) with actual calorimetry. For (TiHf)–(NiCu) systems, the dual thermodynamic–kinetic methodology allows for a quantifiable relationship between alloy composition, enthalpy landscape, and structural state evolution that has not before been demonstrated in the literature. As a result, the findings contribute to the development of high-temperature shape-memory materials with tuneable martensitic-transformation temperatures above the NiTiHf threshold and adjustable amorphous stability.

2. RESEARCH METHODOLOGY

2.1. Technology of Obtaining Layers as a Result of Ultra-Fast Cooling

For the preparation of the studied alloys, titanium (Ti), hafnium (Hf), nickel (Ni) and copper (Cu) chemical elements with a purity of 99.9–99.99% are used. The alloys are prepared by the induction method (the total weight of the casting varies from 30 g to 60 g).

For ultra-fast cooling, the ‘master’ alloys given in Table 1 were used. The samples were prepared by the planar casting method. In this method, the distance between the rapidly moving mass disk and the liquid metal is stable (less than 1 mm; in our alloys, this distance was 0.15–0.2 mm). The hole, into which the liquid metal is poured, is of 0.3–0.35 mm, and its length is of 7–10 mm. These distances allow the cross-section of the obtained ribbons to be large. A 5–15 g section of the mentioned ‘master’ alloy is placed in a quartz tube and heated by the induction method. The temperature is controlled by pyrometers. The temperature of pouring the alloy onto the casting drum is taken

TABLE 1. Nominal chemical composition, alloy heat treatment temperature $T_{\text{heat treat.}}$ [°C] and symbols of the studied samples.

Alloy symbol	Alloy composition, at.%	$T_{\text{heat treat.}}$, °C
SMA (1.1)	$Ti_{32}Hf_{18}Ni_{50}$	1300
SMA (1.2)	$Ti_{32}Hf_{18}Ni_{45}Cu_5$	1280
SMA (1.3)	$Ti_{32}Hf_{18}Ni_{35}Cu_{15}$	1220
SMA (1.4)	$Ti_{32}Hf_{18}Ni_{25}Cu_{25}$	1220

50–150 K above the liquidus line, while the viscosity of the alloy is also taken into account. The pouring process is carried out in an argon atmosphere under a pressure of 0.2 MPa. The material of the disk onto which the alloy is poured is made of Cu (Co–Be), and its diameter is of 200 mm. The rotation speed of the disk is between 5–30 m/s (optimal speed of 19 m/s, pressure of 0.2 MPa) (Fig. 2).

Heat Treatment of Samples. A tubular vacuum furnace was used for heat treatment of samples. This furnace belongs to the class of electric resistance furnaces and allows full temperature control. For complete thermal stabilization of samples, they are placed in a package (two parallel steel sheets).

The heat treatment process combines the following sequence: cut strips (flakes) are collected in a special package and placed in the middle of a quartz tube. With the help of a forevacuum pump, the pressure is brought to 10^{-2} torr, and with the use of a turbomolecular pump, to 10^{-5}. After that, the thermal treatment mode is set: heating rate, temperature, holding time (at a specified temperature) and the cooling process of the package.

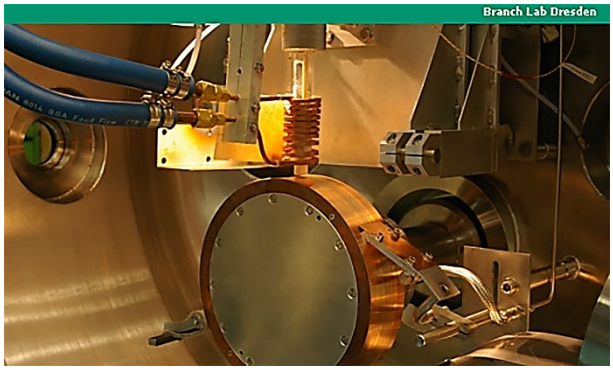

Fig. 2. The device used to produce ultra-fast hardened layers operates using the planar casting method.

The heating rate can be set to 300 K/h and 600 K/h, the isothermal holding mode can be set in the range of 300–900°C from 2 minutes to 4 hours, cooling is carried out in air. At this point, the sample package is removed from the quartz tube (and the quartz tube is cooled in a vacuum, as mentioned).

After the heat treatment process, the structure of the alloys was systematically studied using x-ray diffraction analysis, electron microscopy, and calorimetric methods.

X-Ray Diffraction Analysis. X-ray diffraction analysis was performed on a Philips diffractometer using CuK_α radiation (CoK_α) (voltage of 40 kV, current of 30 mA). The 20 angle was determined between 10–90°.

Transmission Electron Microscopy (TEM). A JEOL 1220 JEM transmission electron microscope (TEM) was used to determine the structure and phase boundaries of the samples.

Differential Scanning Calorimetry (DSC). Differential scanning calorimetry was used to study accurately any phase transformations that depend on temperature.

3. RESULTS AND DISCUSSION

3.1. Formation Enthalpy of Liquid Alloys of the $(TiHf)_{50}(NiCu)_{50}$ System

The heat of formation of liquid alloys of the two-component systems Ni–Ti and Ni–Hf was studied by the calorimetric method at 1873 K. The experiment consisted in continuously adding a certain mass of refractory metals and recording the thermal effect of their dissolution.

Several experiments were conducted for each system to study the enthalpies of mixing of refractory metals with nickel. It was found that the indicators of each of them were the same, and then they were processed together. The method of approximation of the experimental results consisted in constructing a simple polynomial model to describe the concentration dependence of the function of αMe partial enthalpy of mixing. The optimal degree of the polynomial was determined using the Fisher statistical criterion. Then, by integrating the dependence obtained according to the Gibbs–Duhem equation, the concentration dependence of the partial property of the second component and the integral enthalpy of mixing were calculated. It was carried out at a value of 0.95 for all quantities (amounts).

The phase diagrams of the studied system [32–34] show that in the crystalline state there is a strong interaction between the particles of the components, which determines the presence of a significant number of intermetallic compounds in them: three for the Ni–Ti system, eight for the Ni–Hf one. In addition, the thermal stability (stability or durability or strength) of the more difficult to melt of them is comparable to the thermal stability of pure nickel. The similar picture of the

phase diagrams [20, 22, 25] allows us to assume that a significant negative deviation from ideality should be observed for alloys of this system. The conducted experimental studies and the analysis of the literature data on the thermodynamic properties of alloys [21, 23, 30, 34, 35] have proven this assumption.

Ni–Ti System. The partial mixing enthalpies of titanium with nickel have been determined in the composition interval $x_{Ti} = 0–0.6$. The partial enthalpies of mixing titanium with nickel are more exothermic quantities. We have been able to express their concentration dependence by the following equation, kC/mol:

$$\Delta\overline{H}_{Ti} = \left(1 - x_{Ti}\right)^2 \left(\begin{array}{l} -194.90 - 151.54x_{Ti} - 1313.49x_{Ti}^2 + 18937.67x_{Ti}^3 - 43418.87x_{Ti}^4 + \\ +29329.04x_{Ti}^5 \end{array} \right).$$

The first minimum enthalpy of mixing of titanium is –194.9±11.0 kC/mol. This value is in complete agreement with the value at 1873 K (–185.0±8.0 kC/mol) in Ref. [36].

The integral enthalpy of mixing of the components is expressed as concentration dependence, kC/mol:

$$\Delta H = x_{Ti}\left(1 - x_{Ti}\right) \left(\begin{array}{l} -194.89 - 74.16x_{Ti} - 462.33x_{Ti}^2 + 4710.12x_{Ti}^3 - \\ -8881.36x_{Ti}^4 + 5010.65x_{Ti}^5 \end{array} \right).$$

The minimum integral enthalpy of mixing is at $x_{Ti} = 0.37$: 41.6±1.1 kC/mol. The enthalpies of mixing obtained in Refs. [19, 33] at 1741 and 1838 K, respectively, agree with our results within the experimental error. However, the results of Refs. [22, 36] show a higher exothermic value at 2000 K. In our opinion, such a picture does not correctly reflect the nature of the temperature dependence of the enthalpy of mixing in the Ni–Ti system, but rather indicates the inaccuracy of individual experimental studies.

Ni–Hf System. The concentration dependence of the enthalpy of mixing for the Ni–Hf system was also studied. For this purpose, two experiments were conducted with $x_{Hf} = 0–0.48$. The equation for the concentration dependence of the enthalpy of mixing of Hf, kC/mol, is as follows:

$$\Delta\overline{H}_{Hf} = \left(1 - x_{Hf}\right)^2 \left(\begin{array}{l} -246.43 + 352.33x_{Hf} - 5630.42x_{Hf}^2 + 322107.21x_{Hf}^3 - \\ -59429.21x_{Hf}^4 + 34285.09x_{Hf}^5 \end{array} \right).$$

The enthalpy of mixing of hafnium at infinite dilution is of –244.4±10.4 kC/mol. According to the results of the studies, the first enthalpy of mixing of hafnium was calculated at 1873 K and the value was determined to be of –214.0±10.0 kC/mol.

The following equation was derived to express the concentration

dependence of the integral enthalpy of mixing in the Ni–Hf system, kC/mol:

$$\Delta H = x_{\text{Hf}}\left(1 - x_{\text{Hf}}\right)\left(\begin{matrix}-244.21 + 88.04x_{\text{Hf}} - 942.52x_{\text{Hf}}^2 + 3951.07x_{\text{Hf}}^3 - \\ -3898.18x_{\text{Hf}}^4\end{matrix}\right).$$

In the composition of hafnium $x_{\text{Hf}} = 0.1$, the integral enthalpy of mixing takes a minimum value of -49.6 ± 1.8 kC/mol.

The analysis of the conducted research and literature data [20–25] shows that the enthalpies of mixing in the Ni–Ti and Ni–Hf systems take anomalously large (for metal–metal type systems) exothermic values. When passing from titanium-containing alloys to hafnium-containing alloys, the magnitude of their exothermicity is observed. This regularity is confirmed for the first enthalpy of mixing of the components and the minimum values of the enthalpies of mixing.

It is obvious that the mentioned regularity is also reflected in the interaction of these elements in the crystalline state, which is expressed by the increase in the thermal stability of the intermetallic phases in this (Ni–Ti) → (Ni–Hf) system. The change in the energetic characteristic of alloy formation of the system and the electrochemical factor, which we used the phasor of the square of the electronegativities of the components, correlates with the change in its character.

The large difference between the electronegativities of the components, the high exothermic heat of their alloy formation, the finding of the minimum integral enthalpy of mixing in the density interval where the most difficult-to-melt intermetallics are present, allow us to speculate about the possibility of localization of chemical bonding in the studied metallic alloys and, as a result, the occurrence of structure-density diversity in the type of chemical combination in them.

A quantitatively similar (identical) hypothesis can be carried out by modelling the thermodynamic properties of alloys within the framework of the theory of associated ideal solutions.

It should be noted that the interest of researchers in the thermodynamic properties of alloys formed by nickel with Ti and Hf is primarily related to their high amorphous formation properties. Within the framework of experimental studies and the results of the proposed (applied) modelling, it can be assumed that the thermodynamic parameters of the alloy formation processes are such that the strong interaction of the components and the tendency of the alloy to form associates allow the alloy to become amorphous during rapid cooling.

3.2. Structure of Rapidly Quenched Alloys of the $(TiHf)_{50}(NiCu)_{50}$ System

As mentioned above, one of the main reasons for the formation of amorphous phases during rapid annealing of metallic alloys is the spe-

cific nature of the interaction between the components of liquid solutions. By studying the thermodynamic properties of amorphous formation systems, for example, the integral formation enthalpy of interparticle interaction of components in different aggregate states, we were able to determine the composition of the alloys [16–20, 22, 25, 37–39].

Although the total length of the layers for each alloy was 15–16 meters, the thickness varied depending on the annealing temperature and speed. 1 m was selected from the central part of the layer for the study, and each end of the part was examined by x-ray structural analysis. In order to clarify the difference between the parts close to the drum and free parts of the layers, the structure of both faces was studied. Then, the layers were cut into 20 cm lengths and checked for uniformity.

3.3. Structure of Rapidly Quenched $Ti_{32}Hf_{18}Ni_{50-x}Cu_x$ Alloys

The first series of $Ti_{32}Hf_{18}Ni_{50-x}Cu_x$ (x = 0, 5, 10, 15 and 25 at.%) alloys of the $(TiHf)_{50}(NiCu)_{50}$ system, which were quenched at high speed, were selected as the research object.

Initially, the rapidly quenched $Ti_{32}Hf_{18}Ni_{35}Cu_{15}$ alloy was investigated. Its x-ray structure was studied, and a diffractogram was recorded. The diffractogram was obtained using CoK_α radiation (Fig. 3). As seen in this figure, in the range of 2θ = 40–55°, a broad interference peak appears in the first coordination sphere. In the second coordination sphere, a weaker interference peak was identified in the range of 2θ = 70–85°. According to the literature, such spectra are characteristic of amorphous materials; however, in order to confirm with certainty that the alloy possesses an amorphous structure, it is also essential to examine its structure using electron microscopy.

For this purpose, the investigated $Ti_{32}Hf_{18}Ni_{35}Cu_{15}$ alloy was additionally studied by electron microscopy. The results of this investigation are presented in Fig. 4. As can be observed, the rapidly quenched

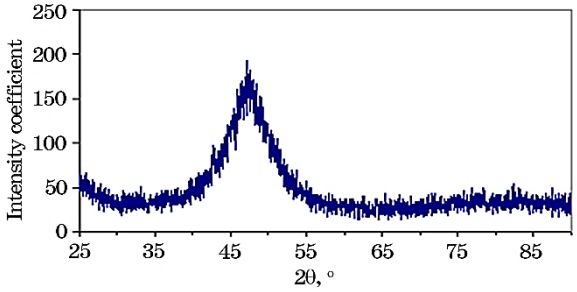

Fig. 3. Diffractogram of the initial state of the $Ti_{32}Hf_{18}Ni_{35}Cu_{15}$ alloy quenched at high speed. T = 20°C, free surface of the layer.

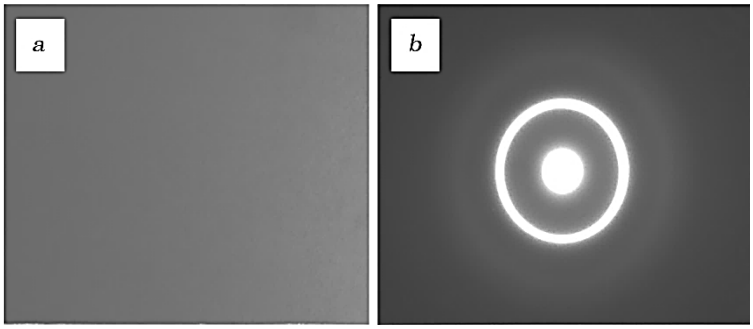

Fig. 4. Initial state image (*a*) and corresponding electron-diffraction pattern (*b*) of the high-speed quenched $Ti_{32}Hf_{18}Ni_{35}Cu_{15}$ alloy. T = 20°C, free surface of the layer.

$Ti_{32}Hf_{18}Ni_{35}Cu_{15}$ alloy has an amorphous structure (Fig. 4, *a*). The corresponding microelectron-diffraction pattern exhibits a diffraction halo, which provides further evidence of the amorphous structure.

Since the rapidly quenched $Ti_{32}Hf_{18}Ni_{45}Cu_5$ alloy was found to exhibit a different structure based on the initial results, its investigation was carried out using several additional methods. The x-ray structure of this alloy was studied over a wider range, and a diffractogram was obtained. The diffractogram was recorded using CoK_α radiation (Fig. 5). As seen in the figure, in the range of $2\theta = 40–55°$, a broad interference peak appears in the first co-ordination sphere; however, superimposed on this peak are lines characteristic of a crystalline structure. In the second co-ordination sphere, no interference peak was detected.

Table 2 lists the possible phases, which can be formed in the studied samples (NiTiHf and TiNiCu are taken as the base elements), the possible structure and lattice parameters, which can be formed in them. When the diffractogram shown in Fig. 5 is calculated to the corresponding crystal structure, the presence of two crystal structures was

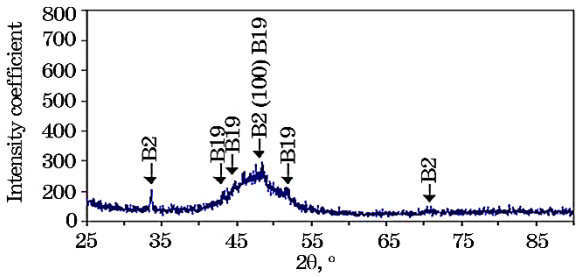

Fig. 5. Diffractogram of the initial state of the high-speed quenched $Ti_{32}Hf_{18}Ni_{45}Cu_5$ alloy. Free surface of the layer at T = 20°C.

TABLE 2. Possible phases that can be formed in the studied samples (NiTiHf and TiNiCu were taken as the base elements).

Alloy	Phase	Structure	Unit cell parameters
$Ni_{50}Ti_{32}Hf_{18}$	$B2$	CsCl type, b.c.c.	$a = 0.3075$nm
	$B19'$	monoclinic	$a = 0.304$, $b = 0.409$, $c = 0.438$, $\beta = 102.4°$
$Ti_{50}Ni_{50-x}Cu_x$	$B2$	CsCl type, b.c.c.	$a = 0.29$–0.31 nm
	$B19$	orthorhombic	$a = 0.29$, $b = 0.427$, $c = 0.451$ nm
	$B19'$	monoclinic	$a = 0.29$, $b = 0.40$, $c = 0.45$, $\beta = 100.2°$
NiTi, NiTiHf	Ti_2Ni		$a = 1.1324$ nm

TABLE 3. Calculation of the diffractogram of the initial state of the $Ti_{32}Hf_{18}Ni_{45}Cu_5$ alloy quenched at high speed. $T = 20°C$, free surface of the layer.

Line number	$d_{hkl\ \text{experimental}}$, nm	Identification
1	3.08931	$B2$ (100)
2	2.41858	$B19$ (101)
3	2.35371	$B19$ (002)
4	2.18244	$B2$ (110) + $B19$ (020,111)
5	2.05069	$B19$ (012)
6	1.54068	$B2$ (200)

revealed: $B2$ (CsCl type, b.c.c.) and $B19$ (martensite with orthorhombic crystal structure). All calculated parameters are given in Table 3.

The $Ti_{32}Hf_{18}Ni_{45}Cu_5$ alloy was also studied using a transmission electron microscope (TEM). Figure 6 shows the structure of the initial state (*a*–*c*) and the corresponding electron diffraction patterns (*d*–*e*) of the $Ti_{32}Hf_{18}Ni_{45}Cu_5$ alloy quenched at high speed. The thickness of the $B19$-martensite plates increases from $\cong 0.3$–0.4 μm (Fig. 6, *a*) to $\cong 0.75$ μm (Fig. 6, *b*). Figure 6, *b* shows a dislocation cluster in the martensite phase, such a structure is often found in crystal structures. Figure 6, *c* shows the self-assembly groups of the martensite plates. Figure 6, *d* shows the electron diffraction pattern corresponding to the (*a*) structure, and Fig. 6, *e* shows the electron diffraction pattern corresponding to the (*b*) structure. All images were taken at room temperature ($T = 20°C$), from the free surface of the layer. Images taken by an electron microscope show that the sample has an amorphous–crystalline structure.

Analogous results were obtained for the other two alloys studied: $Ti_{32}Hf_{18}Ni_{50}$ is amorphous-crystalline, and $Ti_{32}Hf_{18}Ni_{25}Cu_{25}$ alloy has an amorphous structure. All results, except for the characteristic temperatures of the martensite transformation after crystallization, are

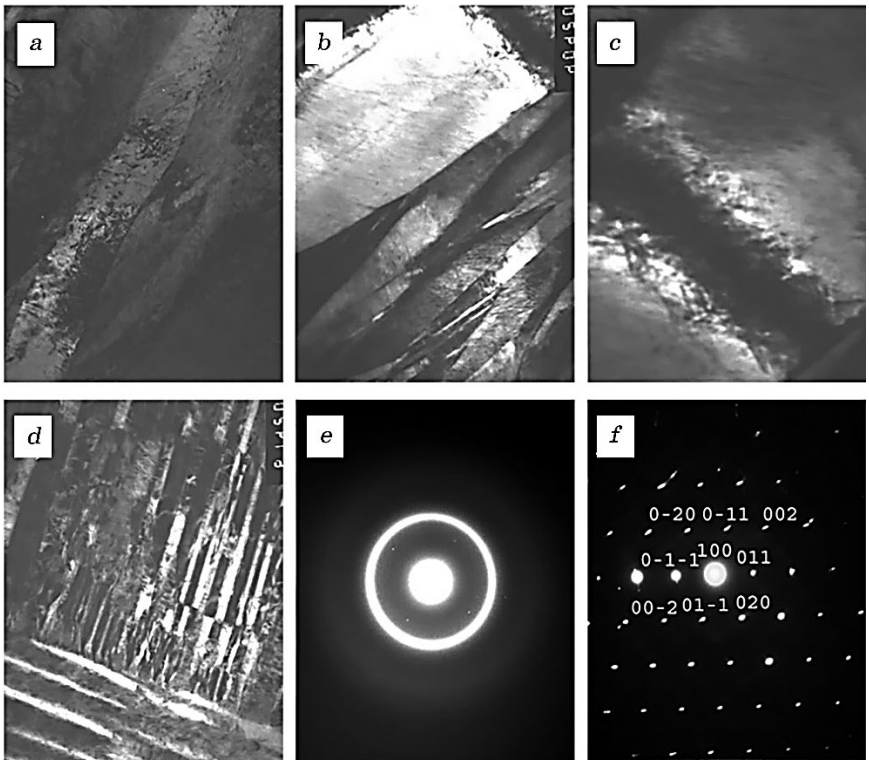

Fig. 6. Initial structure of the rapidly quenched $Ti_{32}Hf_{18}Ni_{45}Cu_5$ alloy (*a*–*c*) and the corresponding electron-diffraction patterns (*e*–*f*): (*a*) plates of *B*19 martensite (≅0.3–0.4 μm thick), (*b*) plates of *B*19 martensite (≅0.75 μm thick), (*c*) dislocation clusters in the martensitic phase, (*d*) self-accommodation groups of martensite plates, (*e*) electron-diffraction pattern corresponding to structure (*a*), (*f*) electron-diffraction pattern corresponding to structure (*b*). $T = 20$°C, free surface of the foil.

not presented in this paragraph, since they are completely repeated. In order to double-check the results of the studies, the phase transitions of $Ti_{32}Hf_{18}Ni_{50-x}Cu_x$ (x = 0, 5, 15, 25 at.%) alloys quenched at high speed were investigated in a calorimetric device.

All transformations occurring in alloys annealed at high speed with temperature changes are characterized by the graphical structure presented in Fig. 7. Figure 7 shows the calorimetric curve of the $Ti_{32}Hf_{18}Ni_{35}Cu_{15}$ alloy annealed at high speed (initial state, heating rate of 20 K/min). As can be seen from the figure, the layers with an amorphous structure have a number of special properties. Such properties can be better recorded by the calorimetric study method. When the sample is heated from $T = 200$°C to T_g (glass transition temperature), an exothermic reaction causes a small variation in the heat flux, which

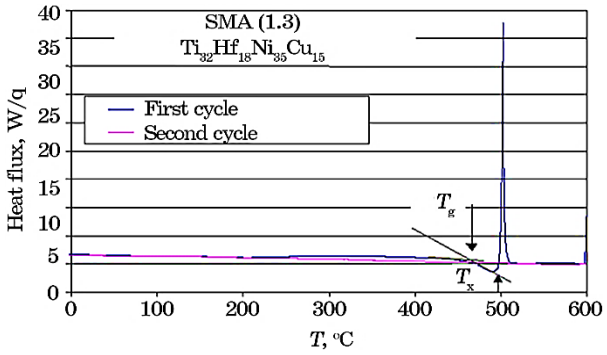

Fig. 7. Calorimetric curve of $Ti_{32}Hf_{18}Ni_{35}Cu_{15}$ alloy, high-speed annealing, heating rate of 20 K/min, initial state (first and second cycles).

in turn leads to structural relaxation in the amorphous phase.

The T_g parameter was determined to explain the temperature transition 'supercooled liquid–solid glass' in glasses and polymers. In our research objects, the T_g parameter is intended as a parameter indicating the approach of a supercooled liquid to a crystalline state in metallic amorphous alloys, a change in linear dependence. The T_x parameter is marked as the initial temperature of crystallization. As is known from the literature, at the beginning of crystallization, a smaller volume crystallizes (10^{-4}), and only then does total crystallization occur. The T_g and T_x temperatures depend on the heating rate, which, in turn, can be controlled by thermal analysis and calorimetry methods.

It is considered important to conduct heat treatment in high-speed hardened $Ti_{32}Hf_{18}Ni_{50-x}Cu_x$ (x = 0, 5, 15, 25 at.%) alloys to study the effect of structural changes on properties.

4. CONCLUSIONS

The following main results were obtained as a result of studying the structure and properties of high-speed quenched $(TiHf)_{50}(NiCu)_{50}$ alloys.

- The physical basis for the selection of chemical composition for four-component alloys with shape-memory effect and other functional properties, which can be obtained by traditional and unconventional technologies, has been developed. In alloys of the $(TiHf)_{50}(NiCu)_{50}$ system, which are annealed at high speed, it is possible to obtain different structural states depending on the composition: amorphous–crystalline or amorphous.
- The nature of the temperature dependence of the martensite transformation on the copper concentration in alloys of the $(TiHf)_{50}(NiCu)_{50}$ system does not change in layers obtained by depo-

sition from the liquid state.

In alloys of the $(TiHf)_{50}(NiCu)_{50}$ system, partial crystallization of the amorphous phase occurs (heating rate of 20 K/min) after thermal treatment in the T_g–T_x interval.

AUTHORS' CONTRIBUTIONS

K. H. Ismayilova performed the fabrication, heat treatment, and differential scanning calorimetry (DSC) analyses of the shape-memory alloy samples. Y. A. Abdulazimova conducted the x-ray diffraction (XRD) analyses to evaluate the integral mixture enthalpy of the constituent components. H. A. Ahlatci carried out the transmission electron microscopy (TEM) investigations and provided interpretation of the microstructural evolution. N. A. Gurbanov undertook the literature review, collected and analysed the experimental data obtained under laboratory conditions, and prepared the manuscript with input from all co-authors. All authors critically reviewed and approved the final version of the manuscript.

REFERENCES

1. Z. L. Wang and Z. C. Kang, *Functional and Smart Materials: Structural Evolution and Structure Analysis* (New York: Plenum Press: 1998).
2. W. Huang, *Materials & Design*, **23**, No. 1: 11 (2002).
3. L. Sun and W. Huang, *Metal Science and Heat Treatment*, **51**, No. 11: 573 (2009).
4. D. Hartl and D. Lagoudas, *Thermomechanical Characterization of Shape Memory Alloy Materials* (Springer–ABD: 2008).
5. K. Otsuka and X. Ren, *Intermetallics*, **7**, No. 5: 511 (1999).
6. G. Song, N. Ma, and H.-N. Li, *Engineering Structures*, **28**, No. 9: 1266 (2006).
7. A. Oudich and F. Thiebaud, *Mechanics of Materials*, **102**: 1 (2016).
8. B. Li, Y. Shen, and Qi. An, *Acta Mater.*, **199**: 240 (2020).
9. A. Shuitcev, R. N. Vasin, X. M. Fan, A. M. Balagurov, I. A. Bobrikov, L. Li, I. S. Golovin, and Y. I. Tong, *Scripta Materialia*, **178**: 67 (2020).
10. C. Ottavia, *Simulation Modelling Practice and Theory*, **11**: 5 (2003).
11. L. Yong, X. Zeliang, and J. V. Humbeeck, *Mater. Sci. Eng. A*, **273**: 673 (1999).
12. T.H. Grgurić, D. Manasijević, S. Kožuh, I. Ivanić, I. Anžel, B. Kosec, M. Bizjak, E. Govorčin Bajsić, Lj. Balanović, and M. Gojić, *J. Alloys and Compounds*, **765**: 664 (2018).
13. M. J. Jaronie, M. Leary, A. Subic, and M. A. Gibson, *Materials & Design*, **56**: 1078 (2014).
14. K. M. Knowles and D. A. Smith, *Acta Metall.*, **29**, Iss. 1: 101 (1981).
15. N. J. Aslanov, K. S. Mammadov, and N. A. Zeynalov, *IJATEE*, **9**, Iss. 87: 155 (2022).
16. K. Otsuka and X. Ren, *Prog. Mater. Sci.*, **50**, Iss. 5: 511 (2005).
17. J. Mohd Jani, M. Leary, A. Subic, and M. A. Gibson, *Mater. Des.*, **56**: 1078 (2014).

18. M. H. Elahinia, M. Hashemi, M. Tabesh, and S. B. Bhaduri, *Prog. Mater. Sci.*, **57**, Iss. 5: 911 (2012).
19. G. S. Firstov, H. J. Van, and Y. N. Koval, *J. Intell. Mater. Syst. Struct.*, **17**, Iss. 12: 1041 (2006).
20. H. E. Karaca, I. Kaya, H. Tobe, B. Basaran, M. Nagasako, R. Kainuma, and Y. Chumlyakov, *Mater. Sci. Eng. A*, **580**: 66 (2013).
21. J. Ma, I. Karaman, and R. D. Noebe, *Int. Mater. Rev.*, **55**, No. 5: 257 (2010).
22. X. L. Meng, W. Cai, L. M. Wang, Y. F. Zheng, L. C. Zhao, and L. M. Zhou, *Scr. Mater.*, **45**, Iss. 10: 1177 (2001).
23. R. K. Mehtiyev and Y. A. Tanriverdiyev, *J. Mach. Manuf. Reliab.*, **54**: 586 (2025).
24. I. S. Golovin and Y.X. Tong, *Scr. Mater.*, **178**: 67 (2020).
25. B. Kockar, I. Karaman, J. I. Kim, and Y. Chumlyakov, *Scr. Mater.*, **54**, Iss. 12: 2203 (2006).
26. M. Y. Kollerov, *Metals*, **5**: 53 (2007).
27. V. I. Kolomytsev and V. A. Lobodyuk, *Metallofizika*, **7**, No. 6: 36 (1985) (in Russian).
28. G. Pang, M. Jin, S. Zuo, and X. Jin, *Intermetallics*, **112**: 106527 (2019).
29. S. S. Mohammed, K. Mediha, I. N. Qader, and F. Dagdelen, *European Journal of Science and Technology*, **17**: 1014 (2019).
30. M. Y. Hasbi, Efendi, and N. Sofyan, *Progr. Phys. Met.*, **26**, No. 1: 64 (2025).
31. V. A. Tatarenko, T. M. Radchenko, A. Yu. Naumuk, and B. M. Mordyuk, *Progr. Phys. Met.*, **26**, No. 1: 3 (2025).
32. R. I. Furunzhiev, *Komp'yuternyye Tekhnologii i Ikh Primenenie* [Computer Technology and Its Application] (Minsk: Vysshaya Shkola: 1985) (in Russian).
33. A. A. Turchanin, I. A. Tomilin, and M. A. Turchanin, *Abstracts of 10th International Conference on Liquid and Amorphous Metals (LAM-10) (30 August–4 September, 1998, Germany, Dortmund)*.
34. M. A. Turchanin and I. V. Nikolaenko, *J. Alloys and Comp.*, **236**, Iss. 1–2: 236 (1996).
35. O. V. Oliinyk and V. A. Tatarenko, *Usp. Fiz. Met.*, **13**, No. 4: 417 (2012).
36. M. A. Turchanin and I. V. Nikolaenko, *J. Alloys Comp.*, **235**, Iss. 1: 128 (1996).
37. N. M. Bilyavyna, V. Z. Turkevych, D. A. Stratiichuk, A. M. Kuryliuk, and O. I. Nakonechna, *Progr. Phys. Met.*, **25**, No. 4: 661 (2024).
38. V. A. Dekhtyarenko, T. V. Pryadko, T. P. Vladimirova, C. V. Maksymova, O. M. Semyrga, and V. I. Bondarchuk, *Progr. Phys. Met.*, **25**, No. 4: 765 (2024).
39. O. V. Oliinyk and V. A. Tatarenko, *Usp. Fiz. Met.*, **19**, No. 2: 152 (2018).

Metallophysics and Advanced Technologies
Металофіз. новітні технол.
Metallofiz. Noveishie Tekhnol.
2026, vol. 48, No. 4, pp. 383–406
https://doi.org/10.15407/mfint.48.04.0383
Reprints available directly from the publisher

PACS numbers: 61.66.Dk, 61.72.Ff, 62.20.Qp, 64.70.dj, 81.05.Bx, 81.40.Pq

Investigation of the Possibility of Cast Production of Hard- and Wear-Resistant Alloyed Iron–Carbon and 'High-Entropy' Alloys Using the CGM Process

I. A. Nebozhak, V. D. Babiuk, R. A. Sergiienko, Ye. A. Zhydkov, Ie. M. Dzevin*, O. V. Derev'yanko**, I. A. Shalevska, T. M. Chevychelova**, V. P. Shkolyarenko, O. Yo. Shinsky, and A. M. Verkhovliuk

Physico-Technological Institute of Metals and Alloys, N.A.S. of Ukraine, 34/1 Academician Vernadsky Blvd., UA-03142 Kyiv, Ukraine
**G. V. Kurdyumov Institute for Metal Physics, N.A.S. of Ukraine, 36 Academician Vernadsky Blvd., UA-03142 Kyiv, Ukraine*
***I. M. Frantsevich Institute for Problems in Materials Science, N.A.S. of Ukraine, 3 Omeljan Pritsak Str., UA-03142 Kyiv, Ukraine*

It is presented the description of the testing method of alloyed Fe–C alloys and 'high-entropy' alloys (HEAs) for wear under dry friction conditions and data of laboratory equipment. For comparison with alloyed steels and cast irons, test samples of HEAs are obtained using the cast by gas model (CGM) process, and, thus, the possibility of its cast production is proven in practice. The structural features of the test castings are identified, and their hardness is determined on the Brinell's scale. The tribotechnical properties of the cast samples are also investigated, and it is established experimentally that these

Corresponding author: Ivan Anatoliyovych Nebozhak
E-mail: nebozhak@ukr.net

Citation: I. A. Nebozhak, V. D. Babiuk, R. A. Sergiienko, Ye. A. Zhydkov, Ie. M. Dzevin, O. V. Derev'yanko, I. A. Shalevska, T. M. Chevychelova, V. P. Shkolyarenko, O. Yo. Shinsky, and A. M. Verkhovliuk, Investigation of the Possibility of Cast Production of Hard- and Wear-Resistant Alloyed Iron–Carbon and 'High-Entropy' Alloys Using the CGM Process, *Metallofiz. Noveishie Tekhnol.*, **48**, No. 1: 383–406 (2026). DOI: 10.15407/mfint.48.04.0386

characteristics are not affected by their hardness, which is determined on the Brinell's scale. The dependences of the slide friction force and the slide friction coefficient of the pair 'cast (liner)–counter body (shaft)' on the friction path are analysed, and functional relations of the type $I_q = f(\tau)$ and $i_q = \varphi(\tau)$ are derived, which describe analytically how the wear and wear rate of the test material change, respectively, on an arbitrary segment of the time interval. The microstructure of the of cast iron is characteristic of the microstructure of alloyed cast irons with special properties, and the microstructure of cast steel samples depends on microalloying and the regime of their heat treatment. The main structural components of the experimental HEAs are single-phase (b.c.c., f.c.c.) and multiphase (b.c.c. + f.c.c.) solid solutions, which further determine their properties. Graphical interpretation and mathematical processing of experimental data show that the structure and properties of the obtained HEAs primarily determine its chemical composition.

Key words: 'high-entropy' alloys, cast, wear, sliding friction coefficient, counter body, hardness, tribotechnical properties, wear rate.

Описано методику випробування леґованих Fe–C-стопів і «високоентропійних» стопів (ВЕС) на зношування в умовах сухого тертя та наведено дані про лабораторну установку. Для порівняння із леґованими крицями та чавунами за ЛҐМ-процесом (лиття за газифікованими моделями) одержано тестові зразки ВЕС, а тим самим на практиці доведено можливість їхнього ливарного виробництва. Із застосуванням металографічної аналізи виявлено особливості структуроутворення піддослідних виливків, а також визначено їхню твердість за Брінеллевою шкалою. Досліджено триботехнічні властивості литих зразків та експериментально встановлено, що на ці характеристики не впливає їхня твердість, яку було визначено за Брінеллевою шкалою. Проаналізовано залежності сили тертя ковзання й коефіцієнта тертя ковзання пари «виливок (вкладиш)–контртіло (вал)» від шляху тертя та виведено функціональні співвідношення типу $I_q = f(\tau)$ й $i_q = \varphi(\tau)$, що аналітично описують як змінюються зношування та швидкість зносу піддослідного матеріялу, відповідно, на довільному відрізку часового інтервалу. Результати металографічної аналізи чавунних виливків показали, що мікроструктура матеріялу є характерною для мікроструктури леґованих чавунів зі спеціяльними властивостями, а мікроструктура литих зразків з криці залежить від мікролеґування та режиму їхнього термічного оброблення. Основними структурними складовими піддослідних ВЕС є однофазні (ОЦК, ГЦК) та багатофазні (ОЦК + ГЦК) тверді розчини, які у подальшому визначають їхні властивості. Графічна інтерпретація та математичне оброблення експериментальних даних показали, що структуру та властивості одержаних ВЕС, у першу чергу, визначає їхній хемічний склад.

Ключові слова: «високоентропійні» стопи, лиття, коефіцієнт тертя ковзання, контртіло, твердість, триботехнічні властивості, швидкість зносу.

(Received 28 May, 2025; in final version, 15 October, 2025)

1. INTRODUCTION

In many branches of the national economy, in particular in the machine-building sector of the economy, for the implementation of modern technological processes, products made of metals and alloys based on them with high physical and mechanical, special, technological properties are often required. This is due, first of all, to the operating conditions of the detail, its cost and other factors. Such a set of characteristics, today, can only be provided by high-alloy steels and alloys, among which high entropy alloys (HEAs) occupy a worthy place.

It is known [1–16] that HEAs have an optimal microstructure and high physical, mechanical and special properties. There are the factors that ensure, in particular, the mechanical characteristics of HEAs, which are [3, 5, 11]: temporary resistance to fracture (σ_v, MPa), relative elongation (δ_5, %), Brinell's hardness (HB, kgf/mm^2) and impact toughness (a_n, J/cm^2), which will be discussed further in the text. Such factors include significant distortion of the crystal lattice, which occurs due to the presence of atoms of chemical elements with different electronic configuration, sizes and thermodynamic characteristics, slow diffusion of atoms of components that are part of the HEAs and their cooperative movement ensure the stability of its phase composition during heat treatment (HT), interaction of impurity atoms, which form, among other things, hybrid bonds in the crystal lattice of the solid solution, which provides a compositional effect of strengthening the HEAs at the atomic level [3]. At the same time, HEAs have the prospect of practical application as a coating of the working surface of a tool for metal cutting, casting moulds, stamps, moulds and spinnerets [5], and can also be used as diffusion barriers and targets for magnetron sputtering.

However, the production of HEAs by traditional methods [3–5, 10–14] is generally a low-productivity and uneconomical process. In addition, the mass-dimensional parameters of such products are limited. The production of workpieces from HEAs by casting allows avoiding the above-mentioned disadvantages [2, 7–9, 15, 16]. The most promising method of cast production of HEAs, which combines high dimensional accuracy with low cost of suitable casting, is the cast by gas model (CGM) process [17].

Based on these and other considerations, the goal of this research was formulated and set, which was to select a HEAs with such chemical composition that would allow it to be effectively used for operation in dry friction conditions. Since the main characteristics of such material are its hardness in combination with high tribotechnical properties, when performing the task, it was necessary to investigate, first of all, the hardness of cast samples, determined by the Brinell scale, their wear and/or wear rate, wear of the counter body material (CBM) and the coefficient of sliding friction of the 'HEAs–CBM' pair. To justify

the economic feasibility of the research, a parallel can be drawn between the tribotechnical characteristics of the studied HEAs and similar properties of traditional wear-resistant materials (cast steels and cast irons), as well as to work out the progressive technology of its cast production.

The object of investigation was the analysis of the structure of cast samples and the analysis of the dependence of the tribotechnical properties of Fe–C alloys and HEAs on their hardness and friction path, as well as the determination of the type and nature of the relationship of an arbitrary segment of the time interval with wear and wear rate of the test material during its wear testing under dry friction conditions. The microstructure, hardness and wear resistance of non-standard high-alloy cast irons with special properties of alloy 1 and alloy 2, wear-resistant low-alloy steels of alloy 3 and alloy 4 (Table 1), as well as a number of HEAs are the subject of this research.

The research methods were: optical microscopy analysis of the structure of steels and alloys, determination of the hardness of castings on the Brinell's scale and testing of cast samples for wear under dry friction conditions, which involved computer processing of the functional dependencies $f = f_1(l_f)$ and $F = f_2(l_f)$. The reliability of the obtained results was ensured by graphical interpretation and mathematical processing of the experimental data. The type and character of the influence of an arbitrary segment of the time interval on the wear and wear rate of the tested material during its testing for wear resistance under dry friction conditions were found out using the provisions of the theory of differential and integral calculus.

The methodology for testing alloys of ferrous and non-ferrous metals for wear under dry friction conditions, proposed by the authors, should be attributed to scientific novelty and practical value. The idea of cast production of HEAs can also be considered scientific novelty, as well as an analytical description of the influence of the duration of testing of the tested steels and alloys on its wear, wear rate and wear of the HEAs.

2. GENERAL TERMS AND DEFINITIONS

In this section made an emphasis on the tribotechnical characteristics of HEAs and their hardness, and also clarifies the type and nature of the bond between its.

2.1. HEAs

HEAs, by formal criteria, are nothing more than baseless alloys containing 5 or more metal elements and it is worth noting that the concentration of each of its should range from 5% to 35% (atomic frac-

tion). From the standpoint of classical physical chemistry, any multicomponent alloy will be high-entropic one, if its entropy factor ($T\Delta S$) in the Gibbs phase equation, which from a mathematical point of view can be represented as dependence [19]

$$\Delta G = \Delta H - T\Delta S, \quad (1)$$

where ΔG is the change in the isobaric-isothermal potential (Gibbs free energy) of the system [J], ΔH is the enthalpy of formation (enthalpy factor) of the chemical compound [J], T is the temperature of the system [K], ΔS is the change in the entropy of the alloy [J/K], is greater than the enthalpy of formation (ΔH) of the most stable chemical compound on the binary or ternary phase diagrams of the elements forming this system [18], *i.e.*,

$$T\Delta S > \Delta H. \quad (2)$$

The types of HEAs known to materials scientists today [19]: amorphous, single-phase (b.c.c., f.c.c.), multiphase (b.c.c. + f.c.c.), and also ordered solid solutions. Multicomponent intermetallic systems deserve special attention of researchers. Such intermetallics are usually: Laves phases (hexagonal $MgZn_2$ ($C14$), cubic $MgCu_2$ ($C15$)), σ phases (such as FeCr), μ phases (such as Fe_7Mo_6), R phases (such as $Mo_3Fe_5Cr_2$).

2.2. Tribology Studies

Tribology studies the processes of contact interaction of solid bodies that are deformed. In other words [18–20], tribology studies the processes of interaction of solid bodies during their relative movement. The field of tribological research is, in particular, the processes of friction and wear. Tribology directly studies friction processes, and tribotechnical studies its application in practice in machine and mechanism assemblies.

Today, the well-known cast HEAs [8], which operate on wear under dry friction conditions in contact with other structural materials, for example, CBM, form a tribological system with its. The physical admeasurements that quantitatively characterize this system [18] in practice are the coefficient of slide friction of the pair 'HEAs–CBM', the wear rate and/or wear of the cast sample, as well as the wear of the CBM. The physical meaning of these admeasurements, from the standpoint of classical tribology and tribotechnics, is described in detail in the works [18–22].

A special case of tribosystems are antifriction systems [18, 19]. A distinctive feature of such systems is low tribotechnical characteristics [8]: wear I_q and wear rate i_q of the material of the experimental

cast, wear I_{CBM} and wear rate i_{CBM} of the CBM, as well as the coefficient of sliding friction f of the pair 'cast sample–counter body'.

Antifriction systems largely ensure the engine life, safety, reliability and durability of all technical equipment and they are among the main objects of research in tribology [2]. During these studies, problems arise that are associated with the lack of equilibrium and the dynamics of states in tribological contact, as well as the complexity of the measurement process, which is connected not only with low resolution of devices and tools, but also with the internal mechanism of tribological processes [20]. Friction and wear are generally considered as types of the destruction process [2], in particular, friction is the overcoming of resistance to the destruction of cold-welding bridges and surface deformation by irregularities of the counter body, and wear is the result of microcutting, cohesive fatigue detachment of particles from the surface of a solid body or brittle destruction of films of chemical compounds on its surface [2]. Such mechanistic representations [20] do not correspond to real processes in antifriction systems. Even under the condition of constancy of the initial dimensions and mass of solids, in heavily loaded tribological systems complex physical-and-chemical and thermal-and-physical processes occur, synthesis of new substances and formation of structures occurs, and any forms of destruction and deformation of the friction surface are considered as signs of their future failure [18]. The author of Ref. [20] showed that in the process of wear in tribological contact tribostructures are spontaneously formed, which fluctuate near the average value in the stationary regime. At the same time, at certain time intervals the dimensions of solids can even increase due to the temporary growth of tribological structures, therefore, due to the limited test time, unreliable results can be obtained [2, 18, 20].

The mathematical apparatus underlying practical calculations of tribotechnical properties of materials and friction pairs (I_q, I_{CB}, i_q, i_{CB}, f) was reflected in a number of publications [7, 8, 23–26]. The authors made their calculations with reference to the scientific works of domestic authors [18–22].

2.3. Mechanical Properties of Materials

The conditional maximum possible mechanical stress [27] that occurs in the material under the influence of an external load on the sample during deformation leads to the destruction of the tested material (rupture of the sample), and corresponds to the maximum on the deformation diagram [27]. The ultimate strength or temporary resistance to fracture [MPa] is determined by the formula [28]

$$\sigma_{в} = R_{m} / S_{0}, \tag{3}$$

where R_m is the fracture force (load) of the test material [N], S_0 is the initial value of the cross-sectional area of the cast sample [mm^2].

The next important mechanical characteristic of the material is its relative elongation (%)—a quantitative measure of deformation, which is given by the relation [28]:

$$\varepsilon = \Delta l / l_0 , \tag{4}$$

where l_0 is the length of the body (rod) before deformation [mm], Δl is the increase or decrease in this length during tension or compression [mm].

Relative elongation is a simplified characteristic of body deformation (4), which is usually used for long thin bodies, *i.e.*, rods. In the general case, the deformation should be characterized by the deformation tensor, since elongation is usually accompanied by a change in the transverse dimensions of the body, and therefore in the notation of the deformation tensor [28]:

$$\varepsilon_{xx} = \Delta l / l_0 . \tag{5}$$

A distinction is made between engineering elongation and true elongation. Engineering elongation is given by formula (4), while true elongation is determined from the relationship given below [29]:

$$d\varepsilon_\tau = \Delta l / l , \tag{6}$$

where l is the length of the body at any moment of deformation [mm].

Therefore, for finite deformation the following mathematical transformation is valid [29]:

$$d\varepsilon_\tau = \int_{l_0}^{l_0+\Delta l} (dl / l) = \ln\left|1 + dl / l_0\right| = \ln\left|1 + \varepsilon\right| . \tag{7}$$

At small deformations, the true and engineering elongations coincide, and at large deformations, the true elongation is usually less than the engineering one.

In cast production, the most widespread method of determining the hardness of the test material is the Brinell scale. The Brinell hardness value is mathematically the ratio of the load acting on the ball to the surface area of the resulting imprint:

$$HB = P / F , \tag{8}$$

where P is the applied load [kgf], F is the surface area of the ball segment [mm^2]:

$$F = \pi D h , \tag{9}$$

where D is the diameter of the ball [mm], h is the depth of the impression (hole) [mm]:

$$h = \frac{D - \sqrt{D^2 - d^2}}{2}, \tag{10}$$

where d is the diameter of the imprint (hole) [mm].

Then, the surface of the spherical segment will be given as

$$F = \frac{\pi D}{2}(D - \sqrt{D^2 - d^2}), \tag{11}$$

and the formula for determining the hardness value on the Brinell's scale will have the following form:

$$HB = \frac{2P}{\pi D(D - \sqrt{D^2 - d^2})}. \tag{12}$$

Knowing the hardness by the Brinell's scale, it is possible to determine the strength limit by the formula

$$\sigma_{\text{в}} = KHB, \tag{13}$$

where K is the proportionality coefficient, which is a constant value for a particular material depending on the hardness of tested cast (for carbon steels, $K = 0.36$ at $HB > 175$ kgf/mm^2; for alloyed steels, $K = 0.34$ at $HB < 175$ kgf/mm^2).

When calculating the temporary resistance to fracture of grey cast irons, in practice, a dependence of the following form is used:

$$\sigma_{\text{в}} = (HB - 40)/6. \tag{14}$$

Impact toughness is estimated by the work done to break a notched specimen during impact bending, related to its cross-sectional area at the notch [3, 5, 11, 28].

The specific impact toughness at bending is defined as the ratio of the work required to break a special specimen by impact to the cross-sectional area at the notch:

$$a_{\text{н}} = A/S, \tag{15}$$

where A is the work spent on the destruction (breaking) of the sample upon impact [J], S is the cross-sectional area of the cast sample at the incision site [cm^2].

The work spent on the destruction of the test sample upon bending is defined as

$$A = mg(H - h), \tag{16}$$

where m is the mass of the pendulum [kg], g is the acceleration of gravity, H is the height of the pendulum centre of gravity before impact [m], h is the height of the pendulum centre of gravity after impact [m].

3. METHODS

This section includes a description of the method of melting and casting cast iron, steel and HEAs, methods of experimental castings for wear under dry friction conditions testing and mechanical testing of cast samples.

The laboratory equipment is descripted below.

3.1. Melting and Cast of Steels and Alloys

The metal was melted in an induction furnace of the IST type with a frequency of 20 kHz and a capacity of 6 kg. The schematic diagram of the melting unit is described in Ref. [8].

The charge was calculated using the program 'Charge' (version 2.0) which was created by specialists of the Physico-Technological Institute of Metals and Alloys, N.A.S. of Ukraine in 2000.

The chemical composition of wear-resistant low-alloy steels of alloy 3 and alloy 4 is regulated by ТУ 4112-78269737-001-2005. The composition of the experimental HEAs is described in Ref. [8], and the chemical composition of high-alloy cast iron and steels with special properties are given in Table 1.

The experimental castings were obtained by the CGM process. The parameters of the CGM process were described by V. S. Shulyak in Ref. [17].

Samples for testing cast steels and alloys for wear resistance were made by cutting. The HT regime of wear-resistant complex Alloy 4 is given in Ref. [30].

TABLE 1. Chemical composition (% wt.) of high-alloy cast iron with special properties.

Alloy	Alloyed elements (Fe—base) (% wt.)									
	C	Si	Mn	Cr	Ni	Cu	V	Ti	P	S
1	3.00	2.00	1.00	02.00	16.00	3.00	–	–	0.035	0.025
2	2.96	0.615	2.005	22.358	01.95	0.00	0.252	0.241	0.10	0.08
3 (70ХЛ)	0.751	0.434	0.852	0.958	–	–	–	–	0.029	0.020
4(75ХФТЛ)	0.782	0.487	0.906	0.953	–	–	0.075	0.115	0.030	0.021

3.2. Metallographic and Phase Analysis of Casting Alloys

The microstructure of the experimental cast irons, casting steels and HEAs was studied using an automatic microscope-analyser 'Epiquant'. The method of making metallographic sections of steel and alloys is described in Ref. [8]. The microhardness of the phases was determined using a microhardness tester ПМТ-3.

Using an x-ray microprobe MS-46 from Cameca, the chemical composition of individual phases was studied. Phase analysis was carried out by x-ray diffractometer 'ДРОН-3' using radiation CoK_α and MoK_α. Measurements were carried out in the angular range of 10–60° with a step of 0.02° and a pulse acquisition time of 2 s [8]. To determine accurately the crystal lattice parameters in the region of distant peaks at large angles, a step of 0.01° and a pulse acquisition time equivalent to 12–16 s were chosen, depending on the type of sample [8].

3.3. Mechanical Testing Methods

Mechanical testing of cast specimens (tensile strength, relative elongation, Brinell's hardness, impact toughness) was carried out according to standard methods. For this purpose, universal equipment was used.

Static tensile tests of steels and alloys were carried out using a universal hydraulic tensile machine P-50. For this purpose, standard samples were used to determine the temporary resistance to fracture and relative elongation of cast alloys. The optimal test temperature is 20 ± 15°C, the highest limit load of the machine is 50 tf, which is equivalent to 500 kN and the power consumption is 2.8 kW.

The hardness of the castings from high-alloyed cast irons, low-alloyed steels and HEAs was determined by the standard Brinell method. The most advanced device for determining the hardness of metals and alloys by the Brinell's scale is the lever-mechanical device of the ТШ-2 model.

Impact testing of cast samples from high-alloy cast irons, low-alloy steels and a number of HEAs was carried out on a pendulum-type of МК-30 model. The limiting energy of a pendulum die is 300 J. The speed of the blade of such a die varies from 4 to 7 m/s, which corresponds to raising the blade of the pendulum to a height of 0.8 to 2.6 m.

3.4. Methods for Testing Steels and Alloys for Wear under Dry Friction Conditions

The study of cast samples for wear under dry friction conditions was carried out according to the original methodology proposed by specialists of the Physico-Technological Institute of Metals and Alloys, N.A.S. of Ukraine. For this purpose, in the Department of Al and tech-

nological processes of casting of aluminium alloys at the Physico-Technological Institute of Metals and Alloys, N.A.S. of Ukraine laboratory equipment (friction machine) was designed and manufactured for testing cast alloys for wear resistance (Fig. 1).

This equipment provides for computer processing of experimental data ($F_f = \varphi_1(l_f)$, $f = \varphi_2(l_f)$) and the principle of its operation is similar to the principle of the friction machine of the model M-22M [31]. Testing of experimental castings for wear under dry friction conditions was carried out according to the scheme 'sample–counter body (shaft)', which is described in [32–36]. The algorithm for mathematical processing of the results of experiment, which is the basis of the methodology for calculating the tribotechnical characteristics, is given in Refs. [31, 33, 34, 36]. As a counter body material in the research, tool steel alloyed with Cr, W and Mn of the 01 AISI was used, the hardness of which after HT was about 66 *HRC*. Overall dimensions of the counter body [mm]: diameter is of 40, thickness is of 12, overall dimensions of the cast sample [mm]: diameter is of 8, height is of 24 ± 1. Parameters of the friction process: test duration is of 6000 s, contact area of the pair 'sample (liner)–counter body (shaft)' is of $5.024 \cdot 10^{-1}$ cm^2, counter body rotation frequency is of 1000 rpm, linear speed of rotation of the counter body is of 2.1 m/s, the normal reaction force of the support (load)

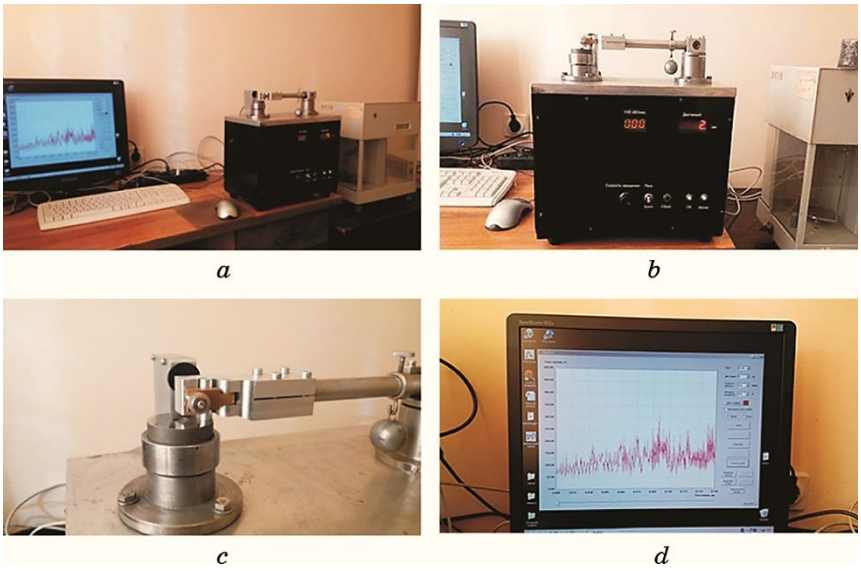

Fig. 1. Laboratory equipment (friction machine) for testing of the cast alloys for wear under conditions of dry friction: general view of the equipment for testing samples for wear resistance [8] (*a*), control unit and measurement of loading and coefficient of sliding friction (*b*), mounting unit of test sample (*c*), program interface for recording the sliding friction force (*d*).

is of 0.25 kgf (except for wear-resistant high-alloy cast iron of alloy 1, for which this parameter is of 0.5 kgf), the friction path (distance) is of 10 km. The change in the mass of the counter body and cast samples at the beginning and end of the studied interval was controlled by weighing on an analytical balance of the Radwag XAS 100/C.

The amount of wear of the casting alloy, as well as the wear of the tool chromium–tungsten–manganese of 01 AISI steel (CBM), is determined as the ratio of the mass loss of the material of the investigated cast sample and counter body, respectively, to the product of the nominal contact area of the pair 'sample–counter body (shaft)' and the friction path [31, 33, 34, 36]:

$$I_{\text{q}}, I_{\text{CB}} = \Delta m / Sl_{\text{f}}, \tag{17}$$

where Δm is the mass loss of the cast sample and counter body [mg], S is the contact area of the pair 'sample–counter body' [cm^2], l_{f} is the friction path [km].

The mass loss of the material by both the test casting and the counter body, in turn, can be determined as

$$\Delta m = m - m_{\text{f}}, \tag{18}$$

where m_0, m_{f} are masses of casting and counter body before and after testing, respectively [mg].

Both wear rate of the cast steels and alloys (cast irons, HEAs), and the wear rate of CBM, *i.e.*, tool steel alloyed with Cr, W and Mn, can be determined, if necessary, using the ratio (13) given in Ref. [26]. The sliding friction coefficients of pairs 'HEAs–01 AISI steel' as well as the sliding friction force were obtained experimentally.

4. RESULTS AND DISCUSSION

This section studies the structure and properties of high-alloy cast irons of alloy 1 and alloy 2 (Table 1), wear-resistant low-alloy steels of alloy 3 and alloy 4, as well as the HEAs of systems $Fe_{24}Ni_{18}Cr_{20}Mn_{15.5}Cu_{17}C_{3.7}Si_{1.8}$, $Fe_{24}Ni_{19.5}Cr_{18}Al_{12}Cu_{21}Mn_{0.3}C_{3.2}Si_2$, $Fe_{20.5}Ni_{19.4}Cr_{16.5}Cu_{20}Mn_{19}C_{2.3}Si_{2.3}$, $Fe_{24}Ni_{19}Cr_{15.5}Cu_{20.5}Al_{15}Mn_{0.5}C_{3.5}Si_2$, $Fe_{22}Ni_{21}Cr_{14}Cu_{23}Al_{19.5}Mn_{0.5}$, $Fe_{24}Ni_{20}Cr_{15}Mn_{18}Cu_{22}Si$, respectively. Working formulas for calculating the wear and wear rate of the material of cast samples from the duration of their testing, *i.e.*, $I_{\text{q}} = f(\tau)$ and $i_{\text{q}} = \varphi(\tau)$ are also derived.

4.1. Microstructure of Steels and Alloys

Typical microstructures (Fig. 2) of alloy 1 and low-alloy alloy 4 steel,

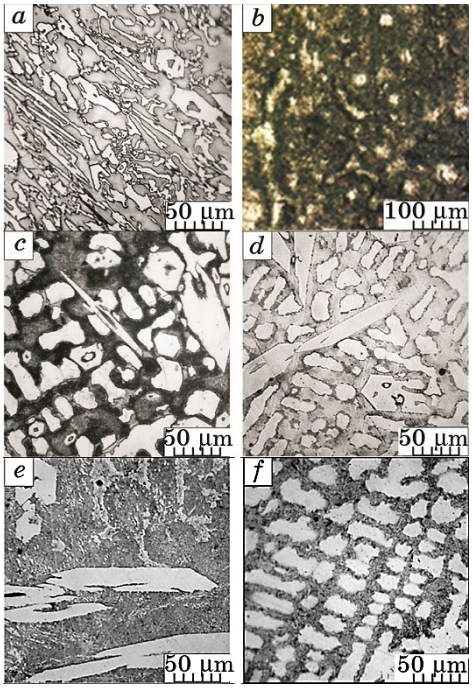

Fig. 2. Microstructure (×500 (*a*, *c*, *d*, *e*, *f*), ×100 (*b*)) of steel and alloys: high-alloy cast iron of the alloy 1 (*a*), low-alloy steel of the 75ХФТЛ type (*b*), HEAs of systems $Fe_{24}Ni_{18}Cr_{20}Mn_{15.5}Cu_{17}C_{3.7}Si_{1.8}$, $Fe_{20.5}Ni_{19.4}Cr_{16.5}Cu_{20}Mn_{19}C_{2.3}Si_{2.3}$, $Fe_{24}Ni_{19}Cr_{15.5}Cu_{20.5}Al_{15}Mn_{0.5}C_{3.5}Si_2$, $Fe_{24}Ni_{20}Cr_{15}Mn_{18}Cu_{22}Si$ (*c*–*f*).

as well as the HEAs systems of the Fe–Ni–Cr–Cu–Al and Fe–Ni–Cr–Cu–Mn are given below. The structure of alloy 1 (Fig. 2, *a*) consists of an austenitic matrix and acicular high-chromium carbides of the (Cr, Fe)$_7C_3$ type. The influence of HT on the microstructure of wear-resistant low-alloy alloy 4 steel was also investigated. For this purpose, the steel samples were heated for quenching to 1333 K, held at this temperature for 1200 s and subsequently cooled through water into oil. To remove residual stresses material was subjected to low tempering. The tempering temperature of the steel castings was 473 K, and the duration of the isothermal holding was 3600 s. After that, the samples of alloy 4 steel were cooled together with the furnace. The composition of the studied material includes martensite and retained austenite, and also Me_mC_n inclusions occur (Fig. 2, *b*).

The amount of retained austenite in the structure of the steel castings is 45–50% (by area). Alloys of the Fe–Ni–Cr–Cu–Mn system have a two-phase structure which consists of primary dendrites and a second phase (Fig. 2, *c*, *d*, *e*), which is formed from the residual liquid and forms the interdendritic space. The branches of the dendrites have an

elongated oval shape. In the HEAs samples of the Fe–Ni–Cr–Cu–Al system, granular dendrites and lamellar eutectic (Fig. 2, *e*) are observed in the interdendritic space. The formation of needle-shaped Me_mC_n, which in cross section have a hexagonal shape (Fig. 2, *c*, *d*, *e*), is due to the high content of C and Cr. C appeared in the HEAs, since cast iron was used as the source of Fe. In the cast structure of the sample presented in Fig. 2, *e*, Me_mC_n does not occur due to the low content of C in the starting materials. The charge material used was stainless Cr–Ni steel (Fe–10% wt. Cr–18% wt. Ni–L (cast steel)). Preliminary microprobe analysis of the HEAs of both systems showed that in the branches of the dendrites there are more refractory elements such as Fe and Cr, and in the interdendritic space there are elements with a lower melting point: Cu, Mn, Al, and Ni in equal concentrations is distributed between the 2 phases. The concentration of valence electrons indicates the probability of the formation of 2 solid solutions with f.c.c. and b.c.c. lattices in the HEAs of the Fe–Ni–Cr–Cu–Al system, and 2 f.c.c. lattices with different atomic lattice parameters: f.c.c.-1 (structure similar to the γ-Fe structure), f.c.c.-2 (structure similar to the Cu structure).

4.2. Hardness of the Test Castings

The hardness (Table 2) of the cast samples (Fig. 3) by the Brinell's scale is in the range from 156.0 kgf/mm^2 to 635.3 kgf/mm^2. Such a 'fluctuation' of this characteristic is due, first of all, to the structure of the test materials, which, in turn, depends on their chemical composition and HT regime.

For example, in the structure of steel castings, such a metastable phase as residual austenite during operation transforms into deformation martensite. At the same time, the microstructure of high-alloy cast irons and HEAs has been sufficiently considered and described in [8].

4.3. Wear Resistance of Cast Samples

It was studied the tribotechnical characteristics (Table 2) of cast irons, steels and HEAs. These characteristics were as follow: wear of the test casting, wear of the CBM and the coefficient of sliding friction of the contact pair 'cast sample–01 AISI Steel'.

Graphical interpretation of the experimental data (Fig. 4) made it possible to find out that the wear of the test casting (Fig. 4, *a*) is in the range from –0.106 mg/(cm^2·km) to +1.358 mg/(cm^2·km), wear of the MCT (Fig. 4, *b*) varies from 0.060 mg/(cm^2·km) to 1.781 mg/(cm^2·km), and the coefficient of sliding friction (Fig. 4, *c*) of the contact pair 'cast sample–01 AISI Steel' is 0.243–0.904.

As in the previous case, this is due to the structure of the material, which is described in [7, 8, 30].

TABLE 2. Hardness and wear resistance of cast irons, steels and HEAs, where WHT—without heat treatment, QOLT—quenching with oil cooling and low-temperature tempering.

Sample	Alloy	HB, kgf/mm^2	I_q, mg/(cm^2·km)	I_{CBM}, mg/(cm^2·km)	f
001	Alloy 1	410.5	+0.740	0.361	0.637
002	Alloy 3 (WHT)	362.5	+0.995	0.348	0.609
003	Alloy 4 (WHT)	415.4	+0.786	0.119	0.666
004	Alloy 4 (QOLT)	635.3	+0.438	0.617	0.589
005	$Fe_{24}Ni_{18}Cr_{20}Mn_{15.5}Cu_{17}C_{3.7}Si_{1.8}$	227.0	–0.106	1.380	0.904
006	$Fe_{24}Ni_{19.5}Cr_{18}Al_{12}Cu_{21}Mn_{0.3}C_{3.2}Si_2$	363.0	+0.352	1.781	0.798
007	$Fe_{20.5}Ni_{19.4}Cr_{16.5}Cu_{20}Mn_{19}C_{2.3}Si_{2.3}$	207.0	–0.106	0.647	0.813
008	Alloy 2	158.0	+1.111	0.318	0.831
009	$Fe_{24}Ni_{19}Cr_{15.5}Cu_{20.5}Al_{15}Mn_{0.5}C_{3.5}Si_2$	336.0	+0.113	0.727	0.900
010	$Fe_{22}Ni_{21}Cr_{14}Cu_{23}Al_{19.5}Mn_{0.5}$	228.0	+1.358	0.524	0.620
011	$Fe_{24}Ni_{20}Cr_{15}Mn_{18}Cu_{22}Si$	156.0	+0.033	0.060	0.243

4.4. Dependence of Sliding Friction Force and Sliding Friction Coefficient on Sliding Friction Path, the Influence of Sliding Friction Force on Sliding Friction Coefficient

It has been experimentally proven (Fig. 5) that the sliding friction force and sliding friction coefficient of the contact pair 'HEAs system $Fe_{24}Ni_{20}Cr_{15}Mn_{18}Cu_{22}Si$–01 AISI Steel' depend on the friction path. For example, Figure 5, a clearly demonstrates the presence of insignificant peaks on the filtration line $F_f = \varphi_1(l_f)$, which indicates, hypothetically, the chemical and, as a consequence, the structural heterogeneity of the HEAs in the zone of its contact with the CBM. The same can be said about the functional dependence of the sliding friction coefficient of the pair under consideration on the sliding friction path (Fig. 5, *b*), *i.e.*, $f = \varphi_2(l_f)$.

Graphical interpretation (Fig. 5, *c*) of the ratio of physical quantities $f = \varphi_3(F_f)$, which were initially given in tabular form and its mathematical processing allowed us to derive, as a result, an empirical equation that analytically describes the influence of the sliding friction force on the sliding friction coefficient of the contact pair 'HEAs $Fe_{24}Ni_{20}Cr_{15}Mn_{18}Cu_{22}Si$ system–01 AISI Steel'. This equation, with the maximum possible value of the approximation reliability ($R^2 = 1$):

$$f = 4 \cdot 10^{-3} F_f + 2 \cdot 10^{-5}. \quad (19)$$

The long process of testing materials ($\tau_f = 6000$ s), which took place under conditions of dry sliding friction without a running-in stage, and the hardness and wear resistance indicators (Table 2) of the com-

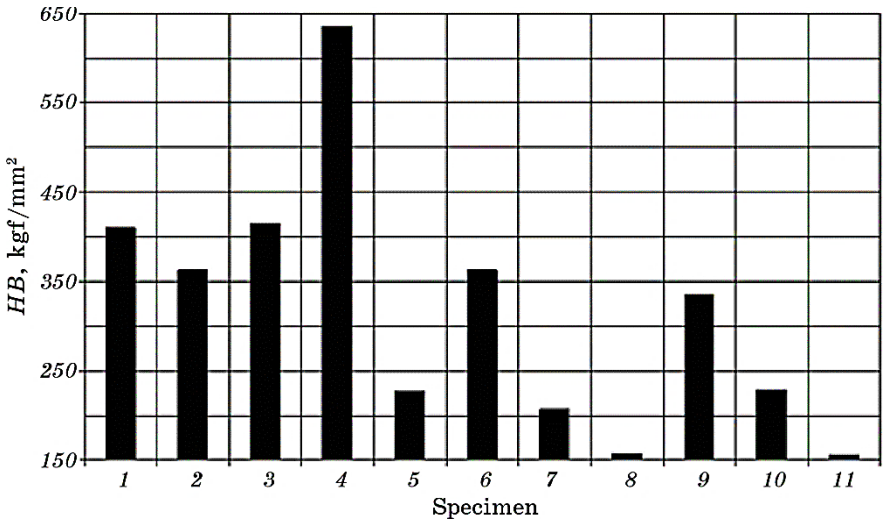

Fig. 3. Hardness of cast steels and alloys: *1*—high-alloy cast iron alloy 1, *2*—low-alloy steel alloy 3 (WHT), *3*—low-alloy steel alloy 4 (WHT), *4*—low-alloy steel alloy 4 (QOLT), *5*—HEAs system $Fe_{24}Ni_{18}Cr_{20}Mn_{15.5}Cu_{17}C_{3.7}Si_{1.8}$, *6*—HEAs system $Fe_{24}Ni_{19.5}Cr_{18}Al_{12}Cu_{21}Mn_{0.3}C_{3.2}Si_2$, *7*—HEAs system $Fe_{20.5}Ni_{19.4}Cr_{16.5}Cu_{20}Mn_{19}C_{2.3}Si_{2.3}$, *8*—high-alloy cast iron Alloy 2, *9*—HEAs system $Fe_{24}Ni_{19}Cr_{15.5}Cu_{20.5}Al_{15}Mn_{0.5}C_{3.5}Si_2$, *10*—HEAs system $Fe_{22}Ni_{21}Cr_{14}Cu_{23}Al_{19.5}Mn_{0.5}$, *11*—HEAs system $Fe_{24}Ni_{20}Cr_{15}Mn_{18}Cu_{22}Si$.

ponents of the contact pair indicate high mechanical and tribotechnical characteristics (I_q, I_{CBM}, f) of the cast samples. Based on these and other considerations, the HEAs system $Fe_{24}Ni_{20}Cr_{15}Mn_{18}Cu_{22}Si$ can be used in tribotechnics as an antifriction material.

4.5. The Influence of the Duration on Wear and Wear Rate

Since the wear rate of the tested material, in the general case [22], is nothing more than the first derivative of its wear with respect to time, *i.e.*:

$$i_q = dI_q / d\tau, \tag{20}$$

and the wear of cast specimens [35, 40, 41, 43] can be represented in the form of dependence (17), then given as

$$l_f = v_f \tau, \tag{21}$$

where v_f is the linear speed of rotation of the counter-body (friction speed), m/s, τ is the current time, s, at the output we obtain the following relation:

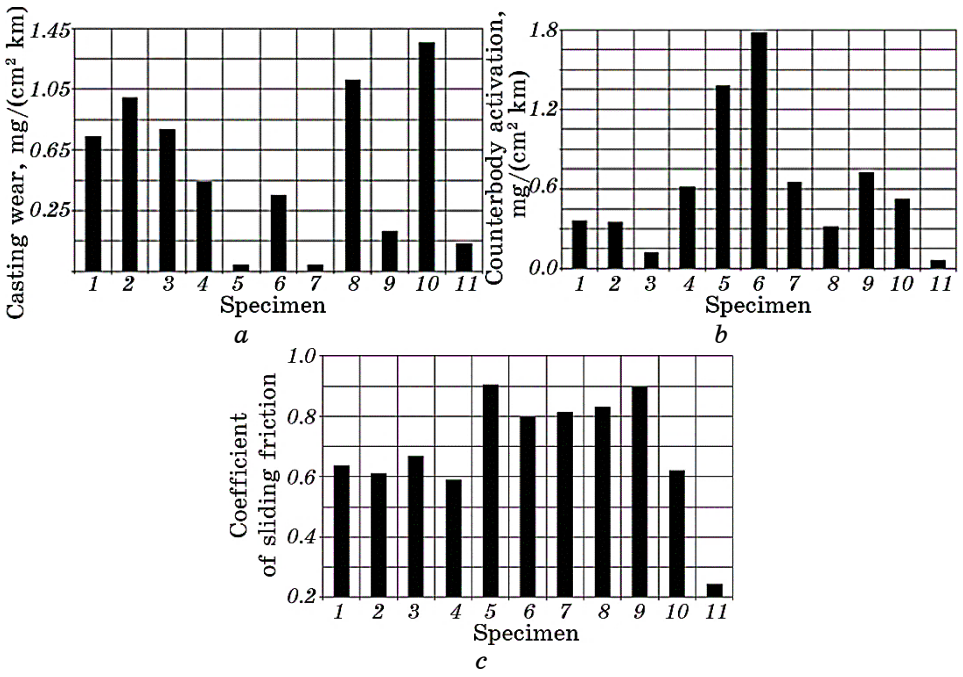

Fig. 4. Tribotechnical properties of cast alloys [8]: *1*—cast iron alloy 1, *2*—steel grade alloy 3 (WHT), *3*—alloy 4 (WHT), *4*—alloy 4 (QOLT), *5*—HEAs system $Fe_{24}Ni_{18}Cr_{20}Mn_{15.5}Cu_{17}C_{3.7}Si_{1.8}$, *6*—HEAs of $Fe_{24}Ni_{19.5}Cr_{18}Al_{12}Cu_{21}Mn_{0.3}C_{3.2}Si_2$ system, *7*—HEAs system $Fe_{20.5}Ni_{19.4}Cr_{16.5}Cu_{20}Mn_{19}C_{2.3}Si_{2.3}$, *8*—Alloy 2, *9*—HEAs of $Fe_{24}Ni_{19}Cr_{15.5}Cu_{20.5}Al_{15}Mn_{0.5}C_{3.5}Si_2$ system, *10*—HEAs of $Fe_{22}Ni_{21}Cr_{14}Cu_{23}Al_{19.5}Mn_{0.5}$ system, *11*—HEAs of $Fe_{24}Ni_{20}Cr_{15}Mn_{18}Cu_{22}Si$ system, the wear of the test casting (*a*), the wear of the MCT (*b*), the coefficient of sliding friction (*c*).

$$I_q = \Delta m/(Sv_f\tau)\,. \tag{22}$$

If we determine the first derivative of the wear of the test material with respect to time:

$$\frac{dI_q}{d\tau} = \frac{\Delta m^{I}(Sv_f\tau) - \Delta m(Sv_f\tau)^{I}}{(Sv_f\tau)^2} = \frac{\Delta m S v_f}{(Sv_f\tau)^2} = \frac{\Delta m}{Sv_f\tau^2}\,, \tag{23}$$

then, the wear rate of cast samples (cast irons, cast steels and HEAs) and their wear can be represented using mathematical expressions, respectively:

$$i_q = \frac{\Delta m}{Sv_f\tau^2}\,, \tag{24}$$

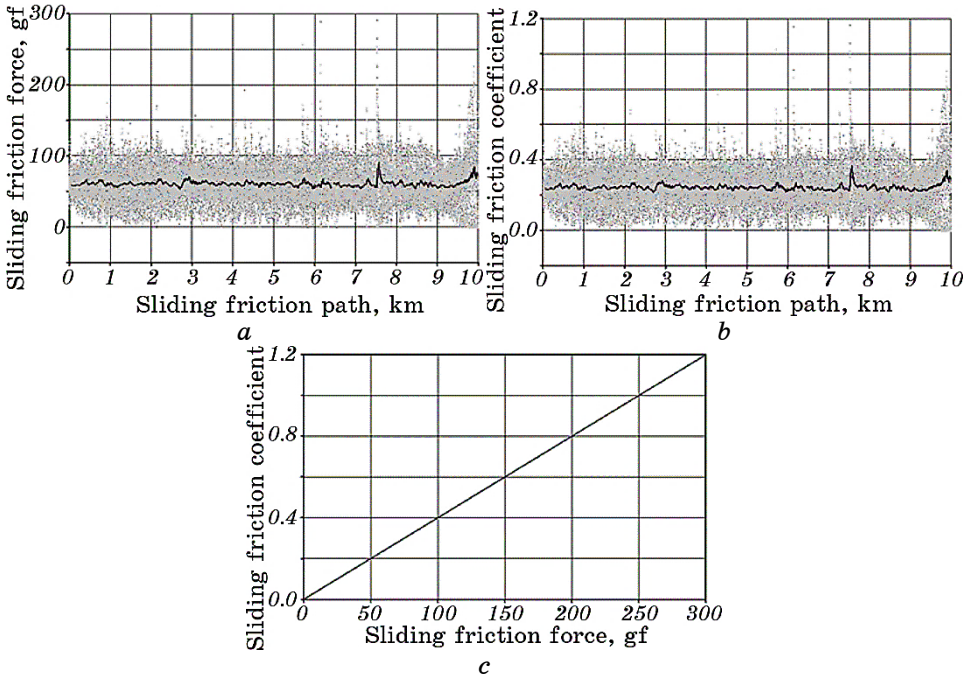

Fig. 5. Dependence of the sliding friction force (*a*) and the sliding friction coefficient (*b*) of the contact pair 'HEAs system $Fe_{24}Ni_{20}Cr_{15}Mn_{18}Cu_{22}Si$–01 AISI steel' on the sliding friction path, as well as the influence of the sliding friction force on the sliding friction coefficient (*c*) of the contact pair 'HEAs system $Fe_{24}Ni_{20}Cr_{15}Mn_{18}Cu_{22}Si$–01 AISI steel'.

$$dI_{\text{q}} = -\frac{\Delta m d\tau}{S v_{\text{f}} \tau^2}. \tag{25}$$

Integrating relation (25) and given Δm [35, 40, 41, 43], we obtain as a result

$$I_{\text{q}} = -\frac{\Delta m}{S v_{\text{f}}} \int_{\tau_{\text{f}}}^{\tau_0} \frac{d\tau}{\tau^2} = -\frac{\Delta m}{S v_{\text{f}}} \left(-\frac{1}{\tau_0} + \frac{1}{\tau_{\text{f}}} \right) = \frac{\Delta m}{S v_{\text{f}}} \left(\frac{1}{\tau_0} - \frac{1}{\tau_{\text{f}}} \right), \tag{26}$$

where τ_0, τ_{f} are the initial and final moments of the casting wear test, respectively, s,

$$\Delta m = m_0 - m_{\text{f}}, \tag{27}$$

where m_0, m_{f} are mass of the cast sample before and after testing it for wear, respectively, mg, and also semi-empirical equations that analytically describe the dependence of the wear rate and wear of steels and

alloys on the duration of their testing under dry friction conditions, respectively:

$$i_{\mathrm{q}} = -\left.\frac{m_0 - m_{\mathrm{f}}}{S v_{\mathrm{f}} \tau^2}\right|_{\tau \neq 0}, \tag{28}$$

$$I_{\mathrm{q}} = \left.\frac{m_0 - m_{\mathrm{f}}}{S v_{\mathrm{f}}} (\tau_0^{-1} - \tau_{\mathrm{f}}^{-1})\right|_{\tau_0 \neq 0, \tau_{\mathrm{f}} \neq 0}. \tag{29}$$

The mathematical relations (20)–(29) presented above can also be applied to the CBM material, *i.e.*, tool alloy HVG steel after its heat treatment. For this, in formulas (20), (22)–(26), (28), (29) it is necessary to replace the symbols of physical quantities, such as 'i_{q}' and 'I_{q}', with the symbols 'i_{CBM}' and 'I_{CBM}', respectively.

4.6. Studies of the Tribostructure of Sliding Friction Pair Components

The results of metallography showed (Fig. 6, *a*) that the microstructure of $Fe_{24}Ni_{20}Cr_{15}Mn_{18}Cu_{22}Si$ without HT is typical for the microstructure of HEAs of this class. HEAs of the 'Fe–Ni–Cr–Mn–Cu' system, which include C as an impurity, have a heterogeneous two-phase structure. The main structural components of these alloys are primary dendritic-type crystals and a secondary phase that is released after the formation of dendrites and forms the interdendritic space. The branches of the dendrites have an elongated oval shape. It was showed (Fig. 6, *a*) that relatively refractory elements (Fe, Cr) are present in

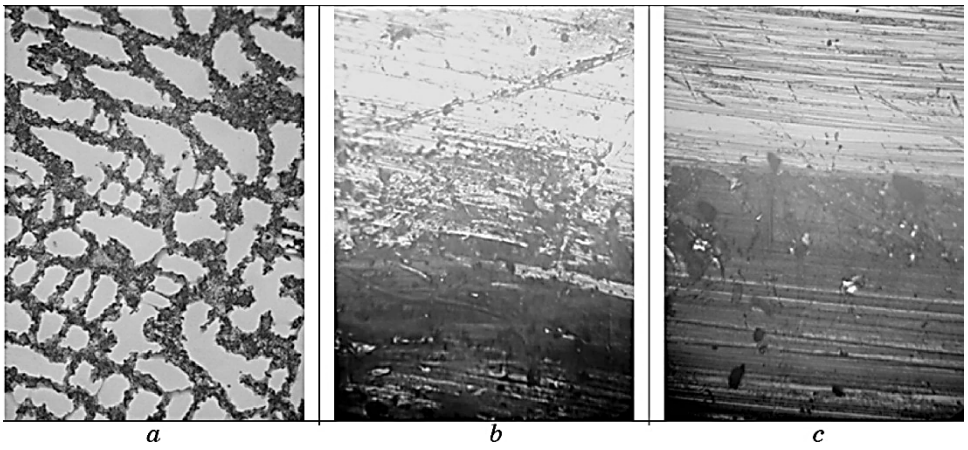

Fig. 6. Micro- (×500 (*a*)) and tribostructure (×200 (*b*, *c*)) of friction pair components: HEAs $Fe_{24}Ni_{20}Cr_{15}Mn_{18}Cu_{22}Si$ (*a*, *b*), 01 AISI steel (*c*).

significant quantities in the branches of the dendrites, and elements with a lower melting point (Cu, Mn) are present in the interdendritic space, while Ni is distributed in equal concentrations between the two phases. The increased concentration of Cr and Fe in the branches of the dendrites led to the fact that their microhardness is approximately in 1.1 times higher than the microhardness of the substance of the interdendritic space. The concentration of valence electrons indicates the probability of the existence of 2 solid solutions based on phases that have an f.c.c. lattice (f.c.c.-1 is similar to γ-Fe in its crystal structure), and f.c.c.-2 in the branches of the dendrites and the interdendritic space is close in structure to the Cu crystal lattice, which is confirmed by the results of x-ray diffraction.

In the process of synthesis of the compositions, a microheterogeneous structure was formed, which is presented below (Fig. 6, *b*, *c*), and which is the subject of future research: the plastic component of casting alloys—thermally stable solid solutions of the elements of the studied alloy, with b.c.c. or f.c.c. lattices; the strengthening phase of the experimental castings is intermetallics ($Me^{I}_{m}Me^{II}_{n}$) and possibly a mixture of solid solutions of the components of the HEAs and intermetallics, *i.e.*, an eutectic, which is allocated in the form of a closed network at the boundaries of crystal grains.

During the wear test of a material under dry friction conditions, on the one hand, its plastic deformation and fracture occur, and on the other hand, the interaction of the environment with its surface occurs, which change the chemical and phase composition, as well as the structure of the friction surface material and play a significant role in the process of testing the contact pair 'HEAs $Fe_{24}Ni_{20}Cr_{15}Mn_{18}Cu_{22}Si$ system–01 AISI steel'. Accordingly, in the friction process, the determining factor is not so much the initial state of the material structure (Fig. 6, *a*), but the structure of its surface layer (Fig. 6, *b*). The latter depends on the primary structure of the material, the formation and occurrence of which is characteristic of the complex conditions of the friction process. Based on these and other considerations, it is necessary to investigate not only the initial structure and phase composition of the tested material, but also the structure and phase composition of the friction surface.

Under the influence of sliding speed, pressure from the applied load and temperature in the dry friction zone during the wear test of the contact pair 'HEAs $Fe_{24}Ni_{20}Cr_{15}Mn_{18}Cu_{22}Si$ system–01 AISI steel', complex physics-and-chemical processes occur in the studied HEAs system, which lead to the formation of a tribological structure on the friction surface (Fig. 6, *b*, *c*). We are talking about the so-called secondary structure, that is, a fundamentally new structure of the material that is formed on its surface during the tribosynthesis process. This is usually a thin deformed layer of material, the chemical compo-

sition of which, structural state, physical-and-mechanical and special properties are radically different from those they were before the friction process began. In this case, we are talking about oxide films on the surface of both the HEAs $Fe_{24}Ni_{20}Cr_{15}Mn_{18}Cu_{22}Si$ system and the CBM (Fig. 6, *c*), *i.e.* high-carbon tool 01 AISI steel, which determine the tribotechnical and operational properties of this friction pair.

5. CONCLUSIONS

An original and progressive method for testing steels and alloys for wear under dry friction conditions was proposed. The possibility of cast production of hard and wear-resistant cast irons, cast steels and HEAs using the LGM process was proven.

The peculiarities of the structure formation of high-alloyed cast iron with special properties of the alloy 2, wear-resistant low-alloy alloy 4 steel after heat treatment, as well as cast HEAs $Fe_{24}Ni_{18}Cr_{20}Mn_{15.5}Cu_{17}C_{3.7}Si_{1.8}$, $Fe_{20.5}Ni_{19.4}Cr_{16.5}Cu_{20}Mn_{19}C_{2.3}Si_{2.3}$, $Fe_{24}Ni_{19}Cr_{15.5}Cu_{20.5}Al_{15}Mn_{0.5}C_{3.5}Si_2$, $Fe_{24}Ni_{20}Cr_{15}Mn_{18}Cu_{22}Si$ were clarified.

The main structural components of wear-resistant high-alloy cast iron of the alloy 2 are hard needle-like inclusions of high-chromium carbides of the $(Cr, Fe)_7C_3$ type in a soft austenitic matrix, and the composition of the wear-resistant low-alloy steel of the alloy 4 includes martensite and residual austenite (45–50% (by area)) after heat treatment and single inclusions of Me_mC_n, while the HEAs structure is formed by solid solutions of the elements included in its composition, with b.c.c. and f.c.c. lattices, as well as $Me_m^{I}Me_n^{II}$ type intermetallics and a mixture of solid solutions of HEAs components and intermetallics, *i.e.* eutectic, which is separated in the form of a closed network at the boundaries of crystal grains.

Mechanical tests of cast samples made it possible to find out that the hardest of all the test materials is the wear-resistant low-alloy alloy 4 after heat treatment—its hardness according to the Brinell scale is equivalent to 635.3 kgf/mm^2.

An original and progressive method of testing steels and alloys for wear under conditions of dry sliding friction is proposed, which allows computer processing of the results of experiment in real time.

The HEAs of $Fe_{24}Ni_{20}Cr_{15}Mn_{18}Cu_{22}Si$ system can be used as an antifriction material in tribotechnics, since its wear (0.033 mg/(cm^2·km)), the wear of the CBM (0.060 mg/(cm^2·km)) working with it in a pair, and the sliding friction coefficient of this pair (0.243) are the lowest among all the tested materials.

The sliding friction force and the sliding friction coefficient of the contact pair 'HEAs of $Fe_{24}Ni_{20}Cr_{15}Mn_{18}Cu_{22}Si$ system–01 AISI steel' depend on the friction path, which indicates the chemical and structural heterogeneity of the HEAs in the area of its contact with the CBM.

In the process of dry sliding friction, the determining factor is not so much the initial state of structure of the material under test, but the structure of its surface layer, because it is the surface layer that absorbs deformation energy, which determines the ability of the material to resist wear.

AUTHORS' CONTRIBUTIONS

I. A. Nebozhak: introductory part, research methodology, planning and setting up of the experiment in the part of foundry production, analysis of the results of research, conclusions. V. D. Babiuk: testing of cast samples for wear under dry friction conditions. R. A. Sergiienko: justification of the choice of materials and methods of testing for wear under friction conditions without lubrication. Ye. A. Zhydkov: methodology for testing the test material for wear under dry friction conditions. Ie. M. Dzevin: graphic interpretation of experimental data, conclusions. O. V. Derev'yanko: obtaining micro- and tribostructures of cast samples. I. A. Shalevska: analysis of results, editing. T. M. Chevychelova: metallographic analysis of the material. V. P. Shkolyarenko: justification, conclusions. O. Yo. Shinsky: research tasks in the field of foundry production, conclusions. A. M. Verkhovliuk: formulation of the task of metallographic analysis and testing of cast samples for wear, conclusions.

REFERENCES

1. M. V. Karpec, O. M. Myslyvchenko, O. C. Makarenko, M. O. Krapivka, V. F. Gorban, and A. V. Samelyuk, *Problems of Friction and Wear*, No. 2: 103 (2014) (in Ukrainian).
2. M. V. Karpec, V. F. Gorban, O. M. Myslyvchenko, S. V. Marchenko, and M. O. Krapivka, *Electrometallurgy Today*, No. 1: 560 (2015) (in Russian).
3. M. V. Karpec, O. M. Myslyvchenko, O. C. Makarenko, M. O. Krapivka, and V. F. Gorban, *Fizyka i Khimiya Tverdoho Tila*, **15**, No. 3: 661 (2014) (in Ukrainian).
4. N. A. Shaburova, M. A. Ostovari, S. N. Veselkov, M. V. Sudarikov, O. V. Samoylova, and E. A. Trofimov, *Physical Mesomechanics*, **24**, No. 4: 28 (2021) (in Russian).
5. M. V. Karpec, O. M. Myslyvchenko, O. C. Makarenko, V. F. Gorban, and M. O. Krapivka, *Powder Metallurgy*, No. 5–6: 118 (2015) (in Ukrainian).
6. R. A. Sergienko, O. A. Schereckij, A. M. Verkhovlyuk, and D. Yu. Matkovskij, *Proc. of Symp. 'Perspective Technologies, Materials and Equipment in Cast Production' (Sept. 25–27, 2023)* (Kramatorsk: 2023), p. 105 (in Ukrainian).
7. I. A. Nebozhak, R. A. Serhiyenko, A. M. Verkhovlyuk, O. A. Shcherets'kyy, Ye. H. Byba, D. S. Kanibolots'kyy, V. D. Babyuk, and Ye. A. Zhydkov, *Abstr. XIII Int. Conf. 'Processec of Mechanical Treatment, Machines and Instruments' (November 9–10, 2023)* (Zhytomyr: Zhytomyrska Politehnika: 2023),

p. 19 (in Ukraine).
8. *Fizyko-Khimichni Zakonomirnosti Protsesiv Oderzhannya Vylyvkiv z Vysokoehntropiynykh Splaviv* [Physical and Chemical Regularities of the Processes of High Entropy Alloys Casts Obtaining] (Kyiv: FTIMS: 2023) (in Ukrainian).
9. T. L. Kuznetsova and N. P. Brodnikovskij, *Casting Proc.*, **154**, No. 4: 58 (2023) (in Ukrainian).
10. J. W. Yeh, Y. L. Chen, and S. J. Lin, *Mater. Sci. Forum*, **560**: 1 (2007).
11. E. D. Tabachnikova, M. A. Laktionova, U. A. Semerenko, C. E. Shumilin, A. V. Podolskij, M. A. Tikhonovskij, J. Mishkuf, and K. Chah, *Low Temp. Phys.*, **43**, No. 9: 1381 (2017) (in Russian).
12. M. V. Karpec, O. M. Myslyvchenko, O. S. Makarenko, V. F. Gorban, M. O. Krapivka, and A. I. Degula, *J. Superhard Mater.*, No. 3: 52 (2015) (in Ukrainian).
13. I. V. Luniov, *Vysokoehntropiyni Splavy* [High-Entropy Alloys] (Kharkiv: KhAI: 2024) (in Ukrainian).
14. D. G. Duhota, *Formuvannya Struktury Bahatokomponentnoho Splavu AlFeCrTiMoCoNi pid Chas Mekhanichnoho Leguvannya* [Formation of the Structure of a Multicomponent AlFeCrTiMoCoNi Alloy During Mechanical Alloying] (Thesis of Disser. for Bachelor) (Kyiv: NTUU KPI: 2021) (in Ukrainian).
15. I. F. Lihackij, *Casting Proc.*, **157**, No. 3: 53 (2024).
16. I. F. Lihackij and M. M. Voron, *Metal and Casting of Ukraine*, **30**, No. 3: 102 (2022) (in Ukrainian).
17. V. S. Shuliak, *Lit'e po Gazifitsiruemym Modelyam* [Gas Model Casting] (Saint Petersburg: Professional: 2007) (in Russian).
18. D. I. Garkunov, *Tribotekhnika* [Tribotechnics] (Moskva: Mashinostroenie: 1985) (in Russian).
19. M. V Kindrachuk, E. A. Kulgavij, O. L. Shevchenko, and A. P. Danilov, *Proc. of NAU*, **1**, No. 1: 102 (2009) (in Ukrainian).
20. E. A. Kulgavij, *Problems of Tribology*, No. 3: 51 (2003) (in Russian).
21. M. V Kindrachuk and E. A. Kulgavij, *Proc. of NAU*, No. 4: 67 (2005) (in Russian).
22. M. V Kindrachuk, E. A. Kulgavij, D. I. Perro, and V. O. Podlesnij, *Proc. of NAU*, **4**, No. 4: 32 (2009) (in Ukrainian).
23. I. A. Nebozhak, V. G. Novyckij, O. J. Shinskij, and V. P. Gavryliuk, *Sci. Treatment Metal.*, No. 2: 62 (2004) (in Russian).
24. I. A. Nebozhak, Ya. I. Nebozhak, V. V. Peresenchuk, and O. Y. Shynskyy, *Metal and Casting of Ukraine*, **29**, No. 4: 30 (2021).
25. I. A. Nebozhak, V. H. Novyts'kyy, O. V. Derev'yanko, D. S. Kanibolots'kyy, and A. M. Verkhovlyuk, *Metal and Casting of Ukraine*, **31**, No. 3: 8 (2023).
26. I. A. Nebozhak, V. G. Novytskyi, Ie. M. Dzevin, and A. M. Verkhovliuk, *Metallofiz. Noveishie Tekhnol.*, **46**, No. 5: 385 (2024).
27. *DSTU 2825-94. Rozrakhunky Mitsnosti ta Vyprobuvannya. Terminy ta Vyznachennya Osnovnykh Ponyat'* [Strength Calculations and Tests. Terms and Definitions of Basic Concepts] (in Ukraine).
28. G. S. Pisarenko, O. L. Kvitka, and E. S. Umanskij, *Opir Materialiv* [Resistance of Materials] (Kyiv: Vyshcha Shkola: 1993) (in Ukrainian).
29. O. V. Mylnikov, *Opir Materialiv* [Resistance of Materials] (Ternopil: Vydavnyctvo THTU: 2022) 257p.

30. L. S. Malinov, N. A. Solidor, and V. A. Milentiev, *Vliyanie Mikrolegirovaniya i Razlichnykh Rezhimov Termoobrabotki Stali 70KhL, Obespechivayushchikh Povyshenie eyo Mekhanicheskikh Svoystv i Abrazivnoy Iznosostoykosti* [The Influence of Microalloying and Various Modes of Heat Treatment of 70XJI Steel, Which Provide an Increase in its Mechanical Properties and Abrasive Wear Resistance] (Rostov-na-Donu: GOU RGASHM: 2008) (in Russian).
31. V. P. Gavryliuk and V. G. Novickij, *Metodika Opredeleniya Iznosostoykosti Materialov v Usloviyakh Treniya Skol'zheniya na Mashine Treniya M22M* [Methodology for Determining Wear Resistance of Materials under Sliding Friction Conditions on a M22M Friction Machine] (Kyiv: FTIMS: 2002) (in Russian).
32. V. G. Hyshnijak and V. I. Korol, *Fizyka i Khimiya Tverdoho Tila*, **4**, No. 1: 161 (2003) (in Ukrainian).
33. L. I. Kuksenova, V. G. Lapteva, A. G. Kolmakov, and L. M. Rybakova, *Metody Ispytaniya na Trenie i Iznos* [Friction and Wear Test Methods] (Moskva: Intermet Ingeneering: 2001) (in Russian).
34. O. V. Zakalov and I. O. Zakalov, *Osnovy Tertya y Znoshuvannya v Mashynakh* [Basics of Friction and Wear in Machines] (TNT Puliyja: 2011) (in Ukraine).
35. E. T. Mamykin and A. I. Yuga, *Powder Metallurgy*, No. 1: 67 (1973) (in Russian).
36. I. V. Kargelskij, M. N. Dobychin, and V. S. Kombalow, *Osnovy Raschetov na Trenie i Iznos* [Basics of Friction and Wear Calculations] (Moskva: Mashinostroenie: 1977) (in Russian).

Metallophysics and Advanced Technologies
Металофіз. новітні технол.
Metallofiz. Noveishie Tekhnol.
2026, vol. 48, No. 4, pp. 407–417
https://doi.org/10.15407/mfint.48.04.0407
Reprints available directly from the publisher

PACS numbers: 52.77.-j, 61.72.Ff, 62.20.Qp, 68.35.Dv, 81.40.Ef, 81.65.Lp, 81.70.Bt

Effect of Plasma Nitriding on Mechanical Properties of Tensile Specimen of 25Cr2Ni4W Low Alloy Steel

O. Hamidane[*,**], B. Chermime[*,**], M. M. Alim[*,**], and M. Fellah[*]

[*]*Department of Mechanical Engineering,*
University Abbes Laghrour,
Khenchela-40000, Algeria
[**]*Advanced Materials Science and Engineering Laboratory ISMA,*
Khenchela-40000, Algeria
[***]*Centre for the Development of Advanced Technologies (CDTA),*
City 20 August 1956, B. P. 17, Baba Hassan,
Algiers, Algeria

This study investigates the effect of plasma nitriding on the tensile specimens of 25Cr2Ni4W low-alloy steel, aiming to enhance their mechanical and tribological surface properties. The experimental analysis compares treated and untreated specimens to evaluate the influence of nitrogen diffusion on the material performance. Results reveals that plasma nitriding led to an increase in elastic resistance (R_e) and a decrease in plastic resistance (R_p), attributed to self-induced heating during treatment. Optical microscopy (OM) confirmed the formation of a distinct nitride layer on the treated surface. The enhancement of the elastic phase contributes to an increase in elongation (L_1), indicating improved ductility. Furthermore, nanoindentation tests demonstrate a significant rise in nanohardness for the nitrided samples compared to the untreated ones, confirming the strengthening effect of nitrogen incorporation and nitride phase formation.

Key words: plasma nitriding, tensile specimen, plastic resistance, elastic resistance, nanohardness, low-alloy steel.

Corresponding author: Brahim Chermime
E-mail: chermime.brahim@univ-khenchela.dz

Citation: O. Hamidane, B. Chermime, M. M. Alim, and M. Fellah, Effect of Plasma Nitriding on Mechanical Properties of Tensile Specimen of 25Cr2Ni4W Low Alloy Steel, *Metallofiz. Noveishie Tekhnol.*, **48**, No. 4: 407–417 (2026). DOI: 10.15407/mfint.48.04.0407

У цьому дослідженні вивчається вплив плазмового азотування на зразки низьколеґованої криці 25Cr2Ni4W, що піддаються розтягуванню, з метою поліпшення їхніх механічних і трибологічних властивостей поверхні. В експериментальній аналізі порівнюються оброблені та необроблені зразки для оцінки впливу дифузії Нітроґену на характеристики матеріялу. Результати показують, що плазмове азотування привело до збільшення пружнього опору (R_e) і зменшення пластичного опору (R_p), що пояснюється самоіндукованим нагріванням під час обробляння. Оптична мікроскопія підтвердила утворення чіткого нітридного шару на обробленій поверхні. Приріст пружньої фази сприяє збільшенню подовження (L_1), що свідчить про поліпшення пластичности. Крім того, випробування на наноіндентацію демонструє значне підвищення нанотвердости для азотованих зразків у порівнянні з необробленими, що підтверджує зміцнювальний ефект включення Нітроґену й утворення нітридної фази.

Ключові слова: плазмове азотування, зразок на розтяг, пластичний опір, пружній опір, нанотвердість, низьколеґована криця.

(Received 14 October, 2025; in final version, 10 March, 2026)

1. INTRODUCTION

Surface modification of metallic materials is essential for improving their service performance in mechanical, tribological, and corrosive environments. Among various surface engineering techniques, plasma nitriding has gained significant attention due to its ability to enhance surface hardness, wear resistance, fatigue strength, and corrosion resistance without compromising the bulk properties of the substrate [1–3]. The process involves the diffusion of nitrogen atoms into the surface of a metallic material under low-pressure plasma at elevated temperatures, typically between 450°C and 600°C, forming a nitrogen-enriched layer composed of hard nitride phases [4, 5].

Unlike conventional gas or salt bath nitriding, plasma nitriding offers several advantages such as faster diffusion kinetics, shorter treatment durations, minimal distortion, and the ability to treat components with complex geometries [6–8]. The plasma environment allows precise control of critical process parameters, including temperature, pressure, gas composition, and bias voltage, enabling the tailoring of the surface microstructure and properties to specific industrial needs [9–11]. These advantages have made plasma nitriding a preferred surface treatment in the automotive, aerospace, tooling, and energy sectors, where components are frequently subjected to severe mechanical and thermal loading [12–14].

During plasma nitriding, nitrogen diffuses into the metallic substrate, forming a compound layer (often called the ‘white layer’) composed mainly of ε-$Fe_{2-3}N$ and γ′-$Fe_{2-3}N$ phases, followed by a diffusion

zone rich in dissolved nitrogen [15, 16]. The compound layer contributes significantly to surface hardness and wear resistance, while the diffusion zone improves fatigue performance through the generation of beneficial compressive residual stresses [17, 18]. These residual stresses act to inhibit crack initiation and propagation, thereby enhancing the fatigue life of nitrided components [6, 19]. Furthermore, the formation of stable nitride compounds and the reduction in surface porosity can improve the corrosion resistance of steels and alloys treated by plasma nitriding [2, 4]. This effect is particularly relevant for applications in aggressive environments, such as marine, chemical processing, and aerospace industries [5, 9]. The relatively low temperatures used in plasma nitriding ensure that dimensional stability is preserved, making it suitable for precision-engineered components where tight tolerances must be maintained [7, 8]. Recent research has focused on optimizing plasma nitriding parameters to achieve desired surface characteristics and to understand the relationship between process variables and resulting properties. Studies reported in 'Metallofizika i Noveishie Tekhnologii' have contributed valuable insights into the mechanisms of nitrogen diffusion, phase formation, and structural transformations under glow-discharge conditions [7, 12, 14]. For example, glow-discharge nitriding and multiplex plasma treatments have been used to improve both hardness and oxidation resistance in ferrous and titanium-based alloys. Similarly, recent investigations on low-temperature plasma nitriding of steels have demonstrated the formation of expanded austenite (S-phase) with superior wear and corrosion performance, broadening the applicability of the technique to stainless steels and other low-alloy systems [8]. In this context, the present work aims to investigate the influence of plasma nitriding parameters specifically temperature, gas composition, and bias voltage on the microstructure and mechanical properties of low-alloy steel. The study is designed to elucidate the relationship between process conditions, the morphology of the nitrided layers, and the resulting mechanical performance. The findings contribute to the broader understanding of plasma-assisted thermochemical treatments, in alignment with recent developments reported in 'Metallofizika i Noveishie Tekhnologii' and other materials science journals [12, 14].

2. EXPERIMENTAL PROCEDURE

The low-alloy steel 25Cr2Ni4W finds extensive application in the manufacturing of pipes, railroad tracks, automobile and aircraft bodies, as well as in onshore and offshore structural engineering. The chemical composition of this low alloying steel is detailed in Table 1. The presence of nickel and chromium imparts excellent tensile strength, wear resistance, and ductility to 25Cr2Ni4W, while manga-

TABLE 1. Chemical composition of 25Cr2Ni4W.

25 Cr2Ni4W	C%	Mn	Cr	Ni	W	P	S
wt.%	0.28	0.5	1.5	3.97	0.73	0.02	0.012

nese enhances its hardenability. In addition, tungsten contributes to improved thermal stability and secondary hardening, making this alloy suitable for components operating under high stress or temperature conditions. The investigation of surface treatments such as plasma nitriding provides valuable insight into the diffusion mechanisms and resulting microstructural transformations within this alloy.

2.1. Condition of treatment

Figure 1 shows the standardized tensile specimen prepared from the 25Cr2Ni4W low-alloy steel. The specimen was machined according to the standard to ensure the accuracy and repeatability of the tensile tests. Its geometry, with a reduced central section, allows uniform distribution of stress during loading and accurate measurement of elongation. The schematic diagram of the specimen is also presented to il-

Fig. 1. Tensile test specimen.

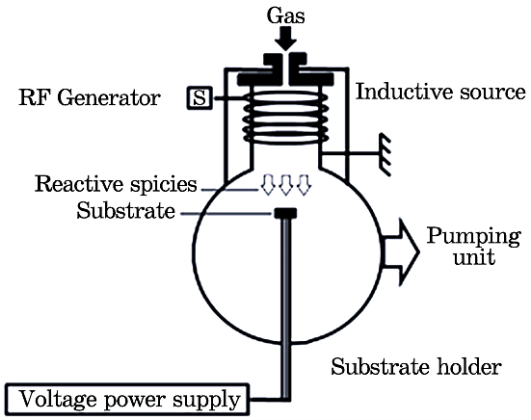

Fig. 2. Plasma nitriding system setup [13].

TABLE 2. Parameters of experience.

Parameter	Value
First pressure	$3 \cdot 10^{-5}$ mbar
W	400 W
V	3.5 kV
Holding time	60 min

lustrate its dimensions and configuration.

The standard experimental configuration of the PIII system is graphically illustrated in Fig. 2, which includes a spherical vacuum chamber of 930 mm diameter. The vacuum chamber was pressurized to $8 \cdot 10^{-6}$ mbar, then filled with nitrogen gas to $8 \cdot 10^{-2}$ mbar. Treatment time was 60 minutes. Alim and colleagues [13] optimized the PIII treatment parameters (frequency, negative bias voltage) mentioned in Table 2 using the same PIII system.

The nitriding conditions were carefully selected to ensure optimal nitrogen diffusion in the low-alloy steel. An initial pressure of $3 \cdot 10^{-5}$ mbar ensures adequate vacuum to purify the chamber before gas introduction. The applied power of 400 W and voltage of 3.5 kV promote the formation of stable and energetic plasma. Finally, a holding time of 60 minutes allows for uniform nitrogen penetration into the material's surface in Table 2.

3. RESULTS AND DISCUSSION

Table 3 summarizes the mechanical properties of the low-alloy steel 25Cr2Ni4W before and after plasma nitriding. The initial diameter ($D_0 = 10$ mm) was identical for both specimens, ensuring comparable testing conditions. After the tensile test, the final diameters were $D_1 = 6$ mm for the untreated and $D_1 = 8$ mm for the nitrided specimen, confirming that the treated steel exhibited less plastic deformation due to surface hardening. The maximum load and ultimate tensile strength increased from $61 \cdot 10^3$ N (1214 MPa) to $62 \cdot 10^3$ N (1636 MPa), indicating a significant improvement in mechanical strength after nitriding. Similarly, the yield strength rose from 995 MPa to 1402 MPa, demonstrating enhanced resistance to elastic deformation. However, the elongation at fracture decreased from 20.4% to 16.6%, reflecting the expected reduction in ductility following surface hardening.

The area of tensile specimen

$$S = \pi D^2/4. \quad (1)$$

TABLE 3. Results of treatment.

Designation	25Cr2Ni4W	
Settings	Untreated	Treated
D_0 [mm]	10	10
D_1 [mm]	6	8
F_p [N]	$61 \cdot 10^3$	$62 \cdot 10^3$
R_p [MPa]	1214	1636
F_e [N]	$50 \cdot 10^3$	$54 \cdot 10^3$
R_e [MPa]	995	1402
L_0 [mm]	50	50
L_1 [mm]	60.2	58.3
A [%]	20.4	16.6

The plastic resistance

$$R_p = F_p / S. \tag{2}$$

Elastic resistance

$$R_e = F_e / S. \tag{3}$$

Elongation on %

$$A\% = (L_1 - L_0)/L_0. \tag{4}$$

3.1. Microstructure

Figure 3, *a* and Figure 3, *b* show the microstructure of the 25Cr2Ni4W low alloy steel untreated tensile sample and after plasma nitriding treatment. As seen in Fig. 3, *a*, the untreated tensile sample consists of ferrite and pearlite phases. In Figure 3, *b*, the microstructure shows three different regions inwards from the surface. These regions consist of the diffusion layer. In our research, we have also tested the change in strength of bonded joints with different heat treatment methods on specimens that have been surface treated in different ways.

3.2. Effect of Plasma Nitriding on Strength

As shown in Fig. 4, the results illustrate the effect of the plasma nitriding treatment on the tensile behaviour of the material. The materi-

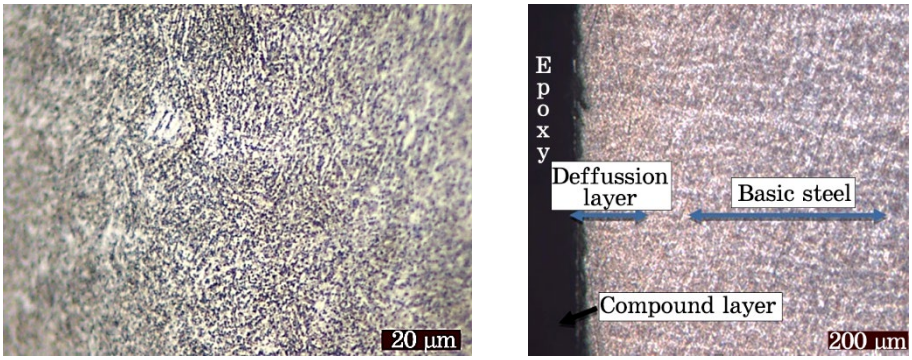

Fig. 3. Microstructure of the 25Cr2Ni4W low alloy steel treated (*b*) and untreated (*a*) tensile sample.

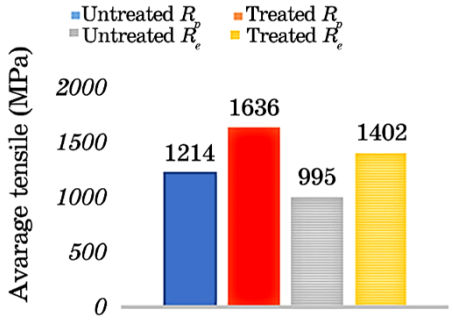

Fig. 4. Effect of nitriding treatment on the plastic resistance (R_p) and elastic resistance (R_e).

al's resistance to permanent deformation increased, as evidenced by the rise in ultimate tensile strength (R_p) from 1214 MPa in the untreated specimen to 1636 MPa after treatment. Similarly, the yield strength (R_e) improved from 995 MPa to 1402 MPa, indicating an enhanced ability of the material to withstand elastic deformation before yielding. The simultaneous increase in both R_p and R_e clearly demonstrates the effectiveness of the plasma nitriding process in strengthening the overall mechanical properties of the steel.

Figure 5 illustrates the comparison of elongation (in mm) between the tensile specimens before and after plasma nitriding. The untreated specimen exhibited a higher elongation of 60.2 mm, whereas the nitrided specimen showed a reduced elongation of 58.3 mm. This decrease in elongation indicates a loss of ductility resulting from the plasma nitriding process. Plasma nitriding, a surface hardening technique based on nitrogen diffusion into the metal surface, enhances

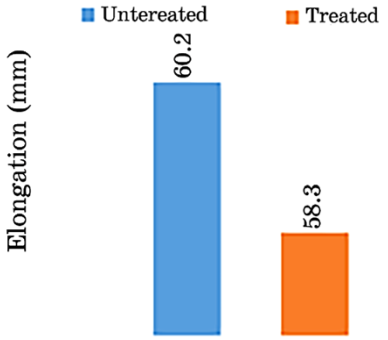

Fig. 5. Elongation of the tensile specimen.

hardness, wear resistance, and fatigue strength. However, it also restricts dislocation motion and introduces residual stresses, which can limit plastic deformation and consequently reduce elongation. Therefore, the results demonstrate that plasma nitriding under the applied conditions (3.5 kV, 60 minutes, 400 W) led to a slight reduction in elongation, reflecting the typical trade-off between increased surface hardness and decreased ductility.

3.3. Hardness Measurement

The nanohardness analysis (see Fig. 6) provides valuable insights into the effect of plasma nitriding on the mechanical behaviour of the 25Cr2Ni4W steel. The untreated specimen serves as the baseline, exhibiting the natural hardness of the core material. In contrast, the

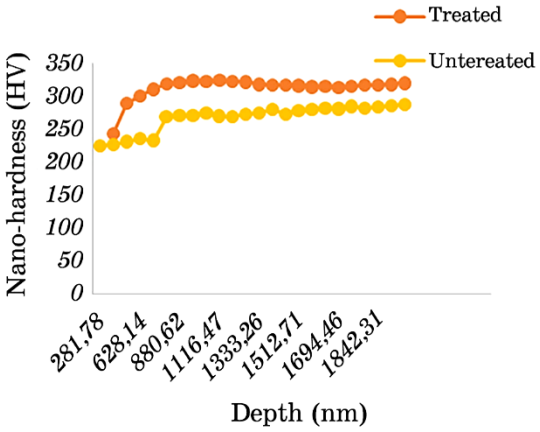

Fig. 6. Hardness measurement.

treated specimen shows significantly higher nanohardness values, confirming the formation of hard nitride phases on the surface. The hardness depth profile reveals a sharp increase near the surface corresponding to the nitride zone followed by a gradual decrease toward the core. This gradient reflects the diffusion of nitrogen atoms, which form hard nitride compounds in the outer layer. The markedly higher surface hardness of the treated specimen indicates a substantial improvement in wear resistance. Moreover, the increased hardness and the depth of the hardened layer demonstrate the effectiveness of the plasma nitriding process in enhancing surface durability and resistance to fatigue. The mechanical behaviour curves further confirm improved elastic properties, as evidenced by the increase in yield strength (R_e), allowing the material to sustain higher loads without permanent deformation. Despite the hardening effect, the material retains acceptable ductility, as shown by its elongation (L_1), ensuring a good balance between hardness and toughness. Overall, the results highlight the formation of a hard, wear-resistant nitride layer that significantly improves the material tribological performance, making it well suited for high-wear mechanical applications such as gears, cams, and other machine components.

4. CONCLUSION

As determined, the plasma nitriding treatment applied to 25Cr2Ni4W low-alloy steel significantly improves its mechanical and tribological surface performance. The systematic investigation has revealed a clear correlation between nitrogen diffusion and the resulting modification of surface properties. The analysis showed that the elastic tensile strength (R_e) increases notably after nitriding, indicating a strengthening of the elastic phase and an enhancement in the material ability to withstand higher loads without permanent deformation. Conversely, a slight decrease in plastic tensile strength (R_p) was observed, mainly attributed to the self-heating effect within the vacuum chamber during treatment.

Optical microscopy confirmed the formation of a continuous and compact nitride layer at the surface, while nanoindentation measurements evidenced a pronounced increase in nanohardness, validating the presence of hard nitride phases. The improvement in elongation (L_1) further indicates that the material retains acceptable ductility despite the surface hardening effect, ensuring a good balance between strength and toughness.

Proceeding from the performed research, it can be concluded that plasma nitriding is an efficient surface engineering process for enhancing the wear resistance, hardness, and durability of 25Cr2Ni4W steel without significantly compromising its ductility. The results

highlight the potential application of this treatment for high-wear mechanical components such as gears, cams, and precision-engineered parts operating under severe loading conditions.

The authors would like to express their sincere gratitude to the management of the Khenchela Mechanical Construction Factory for their valuable assistance and collaboration during the experimental work. Special thanks are also extended to Mr. Mohamed Alim Mounes from the CDTA Research Centre (Advanced Technology Development Centre) of Algeria for his technical support and insightful contributions throughout this study.

AUTHORS' CONTRIBUTIONS

Ouafa Hamidane performed all the experimental work, prepared the figures, and wrote the original draft of the manuscript. Brahim Chermime proposed the research topic, supervised the study, and contributed to the correction and partial writing of the manuscript. Mohamed Mounes Alim carried out the experimental work in his laboratory, and all experimental results were obtained under his supervision. Mamoun Fellah interpretation of the results. All authors read and approved the final version of the manuscript.

REFERENCES

1. M. Drouet and E. Le Bourhis, *Metals*, **16**, No. 13: 4704 (2023).
2. Z. Zhang, Z. Wang, B. Jin, B. Zhang, H. Dou, Z. Zhou, Y. Li, and Y. He, *Surf. Coat. Technol.*, **496**: 131688 (2025).
3. I. Braceras and M. M. A. Bautista, *Surf. Coat. Technol.*, **500**: 131902 (2025).
4. M. Hirano, K. Miura, and N. Ohtsu, *Materials*, **18**, No. 1: 140 (2025).
5. H. Long, X. Zhou, Y. Ma, K. Li, and J. Ren, *Metals*, **14**, No. 9: 1061 (2024).
6. F. Alvarez-Antolin, A. Gonzalez-Pocico, A. Cofico-Villar, and C. H. Alvarez-Perez, *Materials*, **15**, No. 3, 906 (2022).
7. K. Lin, J. Qiao, D. Gu, H. Wang, B. Shi, W. Zhang, J. Shan, Y. Xu, and L. Tian, *Virtual and Physical Prototyping*, **18**, No. 1: e2225490 (2023).
8. A. C. Sphair, A. M. Vianna, C. M. Lepienski, G. Biscaia de Souza, E. A. Bernardelli, and M. Mafra, *Coatings*, **15**, No. 8: 975 (2025).
9. S. Latushkina, D. Kuis, O. Posylkina, A. Kasperovich, and E. Panin, *Materials Letters*, **303**, No. 15: 130527 (2021).
10. E. Roliński and M. Woods, *J. Heat Treat. Mater.*, **76**, Iss. 1: 58 (2021).
11. L. F. Zagonel, J. Bettini, R. L. O. Basso, P. Paredez, H. Pinto, C. M. Lepienski, and F. Alvarez, *Surf. Coat. Technol.*, **207**: 72 (2012).
12. B. T. Danh and L. H. Ky, *Eng. Technol. Appl. Sci. Res.*, **13**, No. 3: 11006 (2023).
13. M. M. Alim, N. Saoula, R. Tadjine, F.Hadj-Larbi, A. Keffous, and M. Kechouane, *Eur. Phys. J. Appl. Phys.*, **75**: 30801 (2016).
14. V. A. Lebedev, O. M. Dubovyy, S. A. Loi, and S. V. Novykov, *Metallofiz. Noveishie Tekhnol.*, **44**, No. 10: 1293 (2022).

15. S. Mändl and D. Manova, *Metals*, **14**, No. 6: 659 (2024).
16. V. Melnik, D. Wolanski, E. Bugiel, A. Goryachko, S. Chernjavski, and D. Krüger, *Mater. Sci. Eng.*, **102**, Iss. 1–3: 358 (2003).
17. J. Musil, J. Vlček, and M. Růžička, *Vacuum*, **59**, No. 4: 940 (2000).
18. O. Sobol, A. Andreev, V. Stolbovoy, S. Knyazev, A. Barmin, and N. Krivobok, *East.-Eur. J. Enterp. Technol.*, **2**, No. 5(80): 63 (2016).
19. M. Naeem, Faryal Qamar Raja, B. J. S. Nolêto, P. L. C. Serra, T. H. C. Costa, J. C. Díaz-Guillén, H. M. Hdz-García, Javed Iqbal, and R. R. M. Sousa, *Mater. Sci. Technol.*, **40**, Iss. 10: 731 (2024).

Metallophysics and Advanced Technologies
Металофіз. новітні технол.
Metallofiz. Noveishie Tekhnol.
2026, vol. 48, No. 4, pp. 419–434
https://doi.org/10.15407/mfint.48.04.0419
Reprints available directly from the publisher

PACS numbers: 46.50.+a, 61.72.Hh, 62.20.F-, 81.40.Lm, 81.40.Np, 81.70.Bt, 83.50.Jf

Review of Modern Practices for Ensuring Strength and Durability Under Multiaxial Loading

M. V. Karuskevych*, T. P. Maslak*, T. V. Turchak**, and O. M. Karuskevych*

**National University 'Kyiv Aviation Institute',*
1 Lyubomyr Huzar Ave.,
UA-03058 Kyiv, Ukraine
***G. V. Kurdyumov Institute for Metal Physics, N.A.S. of Ukraine,*
36 Academician Vernadsky Blvd.,
UA-03142 Kyiv, Ukraine

The article combines theoretical and applied aspects of the multiaxial fatigue problem. It presents a brief overview of modern theories and hypotheses, as well as examples of methods, for quantitatively assessing fatigue damage in metallic structures under multiaxial loading. The necessity of conducting this analysis arises, firstly, from the importance and prevalence of the issue of multiaxial cyclic loading, and secondly, from the extensive number of attempts to address it. The analysis includes characteristics of classical approaches, contemporary models of multiaxial-fatigue damage, and examples of normative documents and methodologies, which have found broad practical application. The aim is to synthesize information on methods for determining damage accumulation under multiaxial loading to identify their potential for further development and application in ensuring the strength and durability of aerospace structural elements. As shown, existing methods for assessing accumulated fatigue damage and predicting durability under multiaxial cyclic loading can be divided into two groups: those ones effective for proportional loading and those ones effective for more complex, non-proportional loading, including in-phase and out-of-phase conditions. Although methods developed for non-proportional loading, particularly based on the critical-plane concept, take into account the geometry of the localized

Corresponding author: Mykhailo Karuskevych
E-mail: mykhailo.karuskevych@npp.nau.edu.ua

Citation: M. V. Karuskevych, T. P. Maslak, T. V. Turchak, and O. M. Karuskevych, Review of Modern Practices for Ensuring Strength and Durability Under Multiaxial Loading, *Metallofiz. Noveishie Tekhnol.*, **48**, No. 4: 419–434 (2026), DOI: 10.15407/mfint.48.04.0419

damage plane, they do not consider the crystallographic slip direction on the critical planes. Accounting for rolling texture, as shown while considering aviation aluminium alloy 2024 T3, can bring the Huber–Mises approach for multiaxial loading closer to the real processes occurring in structural materials at the microscale level.

Key words: aerospace structures, multiaxial fatigue, strength theories, proportional loading, non-proportional loading, equivalent stresses, critical plane, irregular loading, crystallographic factor.

У статті поєднано теоретичні та прикладні аспекти проблеми багатовісної втоми. Представлено короткий огляд сучасних теорій і гіпотез, а також приклади методів кількісної оцінки пошкоджень через втому у металевих конструкціях за багатовісного навантаження. Необхідність проведення цієї аналізи виникає, по-перше, через важливість і поширеність питання багатовісного циклічного навантаження, а по-друге, через велику кількість спроб його вирішення. Аналіза включає характеристики класичних підходів, сучасні моделі пошкоджень від багатовісної втоми, а також приклади нормативних документів і методологій, які знайшли широке практичне застосування. Метою є синтеза інформації про методи визначення накопичення пошкоджень за багатовісного навантаження, щоб визначити їхній потенціял для подальшого розвитку та застосування у забезпеченні міцности та довговічности елементів аерокосмічних конструкцій. Показано, що наявні методи оцінки накопичених пошкоджень від втоми та прогнозування довговічности за багатовісного циклічного навантаження можна розділити на дві групи: ефективні для пропорційного навантаження й ефективні для більш складного, непропорційного навантаження, включаючи синфазні та нефазні умови. Хоча методи, розроблені для непропорційного навантаження, зокрема засновані на концепції критичної площини, враховують геометрію площини локалізованого пошкодження, вони не враховують напрямок кристалографічного ковзання на критичних площинах. Врахування текстури кочення, як це показано за розгляду авіяційного алюмінійового стопу 2024 T3, може наблизити підхід Губера–Мізеса щодо багатовісного навантаження до реальних процесів, що відбуваються у конструкційних матеріялах на мікрорівні.

Ключові слова: аерокосмічні конструкції, багатовісна втома, теорії міцности, пропорційне навантаження, непропорційне навантаження, еквівалентні напруження, критична площина, нерівномірне навантаження, кристалографічний фактор.

(Received 23 February, 2026; in final version, 23 March, 2026)

1. INTRODUCTION

The necessity of analysing and systematizing information presented in published articles on methods for predicting the durability of structural elements operating under multiaxial loading arises from the complexity and persistent relevance of the multiaxial fatigue problem.

The complexity of multiaxial loading, damage, and failure has led to the emergence and development of numerous theories, calculation methods, and experimental studies. Existing analytical methods differ in their practical applicability, which is largely determined by their key parameters and the limitations imposed by the physical and mechanical properties of materials and the characteristics and conditions of their loading.

Multiaxial cyclic loading and the corresponding fatigue damage are classified as proportional and non-proportional, in-phase and out-of-phase. An example of a structure subjected to multiaxial cyclic loading is a modern aircraft.

Loading in aircraft components, particularly the fuselage arises from: excessive pressure in the cabin, causing axial and radial stresses; loads transferred from the wings and empennage during flight; landing gear loads not only during landing but also during ground movements.

It is noteworthy that the proportional loading caused by cabin pressurization combines with aerodynamic forces leading to bending and torsion of the aircraft structure. These loads are irregular and non-proportional.

Simultaneously, the stringent airworthiness requirements for aircraft, as reflected in relevant international airworthiness standards, must be emphasized. These standards demand detailed analysis and robust methodologies for fatigue life prediction [1].

Not all modern developments of failure and damage models under multiaxial loading have found practical application or representation in normative documents. However, their contribution to the advancement of the science of multiaxial loading undoubtedly has a cumulative effect.

2. STANDARDS AIMED AT SOLVING PRACTICAL PROBLEMS OF ENSURING STRENGTH AND DURABILITY UNDER BIAXIAL LOADING

Ensuring strength and durability under biaxial loading is a common task for strength specialists in many fields of engineering. This has led to the development and application of numerous standards for performing calculations and making decisions. Typically, these standards are based on practices that have proven their effectiveness. Below are some examples that provide an understanding of the widespread use of standardized, verified approaches to addressing multiaxial loading issues. Methods for determining equivalent and permissible stresses under static loading are covered in the Ukrainian State Standard DSTU 2464-94 [2].

The technical report of the International Organization for Standard-

ization (ISO/TR) [3] addresses the fundamental existing principles of testing and analysing fatigue damage under multiaxial loading. It presents experimental data accumulated over 80 years, with the initial studies conducted in the 1930s. The evolution of methodologies has progressed from investigating specific conditions of biaxial loading, such as torsion, bending with torsion, cantilever bending, and loading with internal pressure, to universal methods employing two standard types of specimens: tubular and cruciform, along with the corresponding designs of testing machines.

The main methods of fatigue testing under multiaxial loading are as follow.

1. Bending with torsion. This type of testing was the first methodology for combined loading in the field of high-cycle fatigue at room temperature. Between 1930 and 1950, numerous machines were developed to study the fatigue of steels used in aviation engines, particularly for crankshafts.
2. Axial loading with torsion.
3. Axial loading with internal and external pressure.
4. Axial loading combined with internal pressure, external pressure, and torsion.
5. Low-cycle loading of cruciform specimens.
6. Loading of cruciform specimens with a stress concentrator in the central zone of the specimen.

The same document discusses modern methods for analysing fatigue damage under multiaxial loading. When designing structural elements operating under multiaxial cyclic loading, the finite element method holds a well-justified and established position for determining stresses and strains.

Tresca's yield criteria (maximum shear stress criterion) and Huber–Mises criteria (octahedral shear strain criterion), combined with the linear Palmgren–Miner rule, are used to estimate fatigue life. However, these approaches are not always supported by experimental evidence.

The ASTM E2207-15 standard [4] specifies the methodology for testing materials under combined axial and torsional loading. The standard addresses strain-controlled testing for axial, torsional, combined proportional, and non-proportional combined loading using thin-walled tubular specimens under isothermal conditions, as well as at room and elevated temperatures. Figure 1 explains the terms 'in-phase' and 'out-of-phase' loading.

The recommended dimensions of the thin-walled tubular specimen are shown in Fig. 2.

It is worth noting that the standard emphasizes the geometric features in connection with the material microstructure. The wall thickness of the specimen must be sufficient to prevent stability loss under

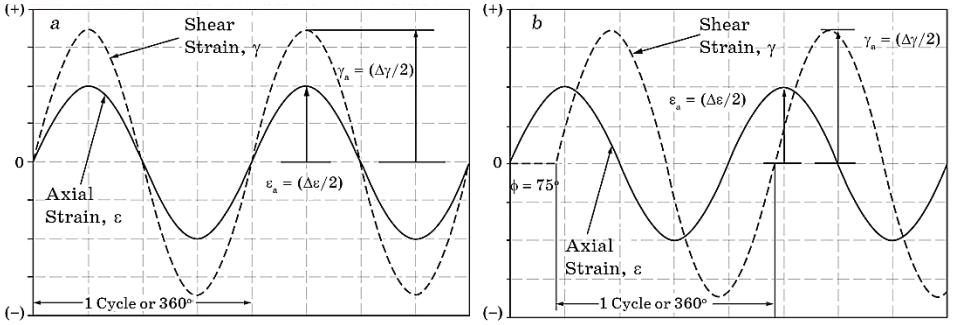

Fig. 1. The schematic of axial and shear strain for in-phase and out-of-phase loading under tensile–torsion testing conditions.

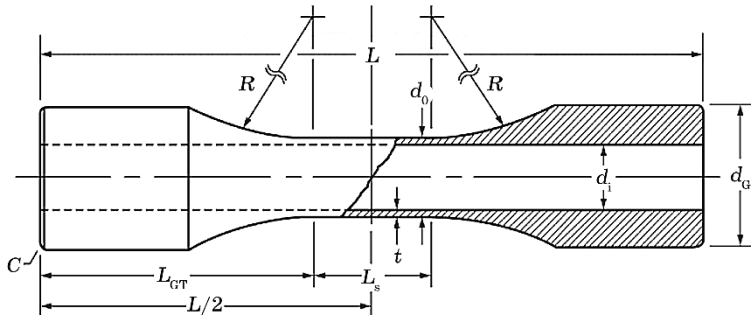

Fig. 2. Thin-walled tubular specimen for combined testing under axial force and torsion.

cyclic loading. At the same time, to meet the definition of a 'thin-walled tube', the diameter-to-wall-thickness ratio must be at least 10:1. Besides, there are microstructural requirements: the wall thickness of the tube must contain at least 10 grains, ensuring isotropy.

The standard, jointly developed by the API (American Petroleum Institute) and ASME, addresses multiaxial stresses in pipelines and pressure equipment. The standard incorporates the critical plane method proposed by Brown and Miller, the 'strain–life' equation, and the method of incremental correction of the material's stress–strain state proposed by Neuber, utilizing the nonlinear kinematic hardening model by Chaboche.

In many cases, existing standards include finite element analysis to model complex stress states, as exemplified in Refs. [10–13].

Regulatory documentation for conducting experimental studies does not provide for the implementation of all possible combinations of principal stresses, which are infinite. As a result, the task of predicting durability under multiaxial loading is addressed using various ana-

lytical methods that account for the specific characteristics of the loading and materials.

The foundation of many analytical methods lies in classical theories formulated for predicting static strength.

3. CLASSICAL STRENGTH THEORIES

The first studies and hypotheses date back to the works of outstanding scientists of the past, Leonardo da Vinci (1452–1519) and Galileo Galilei (1564–1642), who initiated research on the strength of materials and structures. With the development of materials science, strength theories and the corresponding criteria have been further developed. Today, the primary, *i.e.*, fundamental strength theories are the first, second, third, fourth, and fifth (Mohr's theory).

According to the first strength theory, strength under complex stress states is determined by the maximum normal stresses. The authors of the first strength theory are G. Galilei and W. Rankine (1820–1872). This theory does not take into account the effect of the other two principal stresses and is proved effective only for brittle materials.

The second strength theory was proposed by E. Mariotte (1620–1684) and later developed by B. Saint-Venant (1797–1886). According to the second strength theory, if the first principal strain reaches the limit value of uniaxial tension, this leads to failure. The theory was used for some time in the XIXth century, but insufficient justification and inconsistency of application results led to the search for more effective approaches to predicting the limit state.

According to the third strength theory, the limit state is caused by reaching a critical value of the maximum shear stress. The theory was proposed by Henri Tresca (1814–1885). According to the proposed maximum shear stress criterion, the condition for reaching the limit state is a critical value of the equivalent stress, which is defined as the difference between the algebraic maximum and minimum principal stresses. For plastic materials, this has been experimentally confirmed, but an obvious drawback is the neglect of the second principal stress.

The fourth strength theory has found the widest application in strength calculations under complex stress states, especially under static loading. The strength criterion is the specific potential energy of distortion accumulated during deformation. The theory was developed by Huber (1872–1950) and Mises (1883–1953). Its theoretical justification was found in the works of G. Hencky (1885–1951); so in scientific literature, this criterion is often referred logically to as the 'Huber–Mises–Hencky criterion'.

In modern computer-aided design and analysis systems, which are based primarily on the finite element method and determine the pa-

rameters of the stress–strain state of structures, the corresponding equivalent stresses are referred to as Mises's stresses.

According to the Huber–Mises theory, the critical state occurs when the potential energy of distortion reaches a critical value.

It should be noted that the Huber–Mises criterion assumes identical material properties in all directions; however, a significant number of metals are anisotropic. For example, rolled sheets of aluminium alloys exhibit anisotropy as a result of deformation during the manufacturing process of such sheets. In this case, anisotropy may be related not only to changes in the shape of metal grains but also to the formation of rolling texture, which is determined by preferred crystallographic slip directions and preferred crystallographic slip planes.

The fifth strength theory was proposed by Mohr (1835–1918). Mohr's theory is most effective for materials that exhibit different resistance to tension and compression. According to Mohr's theory, allowable stresses depend on the relationship between the components of the stress state, which is determined graphically using Mohr's circles. Mohr's theory is most effective in determining the limit state of brittle materials and requires a significant experimental database. If the allowable stresses in tension and compression are the same, the calculation results according to Mohr's theory coincide with the third strength theory.

The first studies of multiaxial stress states under monotonic loading considered the classical strength theories of Lamé and Tresca from the late XIXth century and the Huber–Mises model from the early XXth century. According to the Huber–Mises formula, the equivalent stress can be found as

$$\sigma = \sqrt{0.5[(\sigma_x - \sigma_y)^2 + (\sigma_y - \sigma_z)^2 + (\sigma_z - \sigma_x)^2]} + \sqrt{3(\tau_{xy}^2 + \tau_{yz}^2 + \tau_{zx}^2)},$$

where σ_{eq} is equivalent Huber–Mises stress; σ_x is longitudinal (axial) stress; σ_y is hoop stress; σ_z is transversal stress; τ_{xy}, τ_{yz}, τ_{zx} are shear stress components.

Unfortunately, the direct application of the aforementioned strength theories for fatigue analysis is not always sufficiently effective.

While the first combined tests date back to the work of Lanza in 1886 [14], systematic studies of multiaxial fatigue were conducted by Gough and Pollard in the 1930s [15]. Their research on fatigue under combined bending–torsion loading created the foundation for models proposed by Gough [16], Sines [17], and Findley [18] in the 1950s. In most early studies of multiaxial fatigue, plastic deformation was generally insignificant.

The study [19] demonstrated that classical yield criteria, such as the Huber–Mises distortion energy criterion, are often applied for predict-

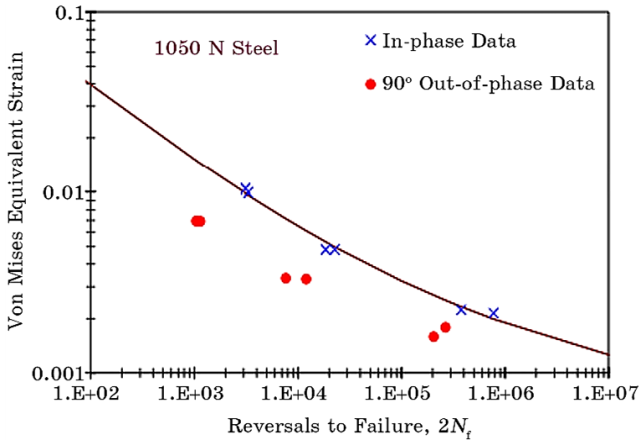

Fig. 3. Fatigue curves for 1050N steel under proportional and non-proportional cyclic loading.

ing multiaxial fatigue.

Such criteria may be effective for in-phase or proportional loading, but they do not account for the reduction in durability observed under out-of-phase or non-proportional loading. For example, in the case of out-of-phase sinusoidal axial–torsional loading with a phase shift of 90°, where axial stress is related to torsional stress through $\sqrt{3}$, the Huber–Mises equivalent stress does not change during the loading process. This should theoretically lead to unlimited durability, which highlights the limitations of this criterion and its unsuitability for out-of-phase or non-proportional loading.

The reduction in durability under non-proportional loading is explained by additional deformation-induced hardening. Under non-proportional loading, the loading components change independently. In this case, not only do the magnitudes of the principal stresses change during loading, but their directions also vary.

The comparison of fatigue durability for in-phase and out-of-phase (90°) loading of T1050 steel is shown in Fig. 3 [20]. Titanium alloys do not exhibit strengthening under non-proportional loading, whereas for steel, the strengthening is in the range of 10–15%. The dependence of the number of load cycles on the Huber–Mises equivalent stress for 1050N steel is shown in Fig. 3.

4. MODERN FATIGUE DAMAGE MODELS FOR MULTIAXIAL CYCLIC LOADING OF METALLIC STRUCTURES

For high-cycle in-phase fatigue of ductile materials, the equivalent stress criteria of Tresca and Huber–Mises, initially proposed for static

loading, have found some application, while the Rankine's criterion is used for brittle materials. However, these criteria are not effective for low-cycle fatigue analysis.

A range of equivalent stress criteria is reviewed in Ref. [21], including the Manson–McKnight method and its modifications. This method involves using equivalent strain energy to assess fatigue levels. The total energy of plastic and elastic deformations is considered decisive for crack initiation and growth processes. The method employs a criterion that accounts for both normal and shear stresses, enabling more accurate evaluation of crack initiation conditions under multiaxial loading. The Manson–McKnight method has been applied in aviation, particularly for predicting the durability of aviation engine components [22].

Methods based on the concept of a critical plane, initiated by Findley [18], are increasingly being applied and incorporated into regulatory documents for fatigue calculations under multiaxial loading. Findley's fatigue criterion focuses on stresses acting on specific planes, referred to as critical planes; these are the planes where the maximum damage criterion is reached. A critical plane is defined as the plane where an extreme combination of shear stresses/strains and normal stresses/strains occurs. The fatigue process is governed by the combination of stresses and strains acting on the critical plane. Findley's model is based on the observation that cyclic shear stresses lead to crack initiation in ductile materials, while normal stresses influence their propagation.

In general form, this model has a view $\max(\tau_{a,n} + k\sigma_n) = f$, where $\tau_{a,n}$ is the shear amplitude on a plane with a unit normal $\mathbf{n}$, *i.e.*, $\tau_{a,n} = \Delta\tau_n / 2$, and σ_n is the normal stress on the same plane. The two material parameters k and f can be determined from two fatigue-loading tests.

Brown and Miller [6] expanded this theory by demonstrating the role of both shear strain and normal one on the maximum-shear plane. They introduced the concept of constant-life contours defined by principal strains (ε_1, ε_2, ε_3) and graphically represented by the equation

$$\frac{\varepsilon_1 - \varepsilon_3}{2} = f\left[\frac{\varepsilon_1 + \varepsilon_3}{2}\right].$$

Their work initiated widespread adoption of a new approach, namely, the critical plane concept, which has been further developed in academic research and practical applications for evaluating durability under multiaxial cyclic loading. The study demonstrated how the orientation of stress components affects fatigue damage and failure.

The critical plane concept is used for both proportional and non-proportional loading, but it is particularly valuable for analysing non-

proportional cyclic loading, where equivalent stress models are not always effective.

Fatigue damage models based on the critical plane concept are currently considered the most effective for analysing multiaxial cyclic loading. In Ref. [23], the effectiveness of several critical plane models was examined, including the Wang–Brown model, the Fatemi–Socie model, the Smith–Watson–Topper model, and others. These models were evaluated under both proportional and non-proportional multiaxial loading conditions for a wide range of durability, covering both the low-cycle fatigue zone and the high-cycle fatigue zone, and for various metals. The Wang–Brown and Fatemi–Socie approaches were found to be the most accurate.

The Fatemi–Socie model [24] extends the Brown's and Miller's model to predict multiaxial fatigue under in-phase and out-of-phase loading. It is based on the premise that maximum shear strain governs crack initiation, while normal stress must be considered in the damage parameters to account for the additional strengthening effect under non-proportional cyclic loading. The Fatemi–Socie model uses the amplitude of shear strain and the maximum normal stress on the critical plane as fatigue damage parameters:

$$\frac{\Delta\gamma_{\max}}{2}\left(1+k\frac{\sigma_{n,\max}}{\sigma_y}\right)=\frac{\tau'_f}{G}\left(2N_f\right)^{b_\gamma}+\gamma'_f\left(2N_f\right)^{c_\gamma},$$

where $\Delta\gamma_{\max}/2$ is maximum amplitude of shear; $\sigma_{n,\max}$ is maximum normal stress in the critical plane; σ_y is yield limit; G is shear modulus; b_γ, c_γ, τ'_f, γ'_f are coefficients of the Coffin–Manson equation for pure torsion at symmetrical cycle; k is correction coefficient.

In work [25], a comparison of several equivalent stress methods and critical plane approaches was conducted. The criterion of absolute maximum principal stress and the signed Mises's criterion were chosen as equivalent stress methods due to their widespread use in industry, attributed to their simplicity and computational speed.

A signing is used to reflect the real load spectrum:

$$\sigma_{eq}=(\text{sign})\frac{1}{\sqrt{2}}\sqrt{\left(\sigma_1-\sigma_2\right)^2+\left(\sigma_2-\sigma_3\right)^2+\left(\sigma_1-\sigma_3\right)^2}.$$

It is mentioned in the work [25] that there exist different approaches for signing procedure: signing should be applied according to principal stresses or by the sign of the first stress invariant.

The Findley's and Matake's criteria were selected for comparison because they have similar formulations but differ in the definition of the critical plane. Both methods yield excessively non-conservative results. It was concluded [25] that the results strongly support the crit-

ical-plane concept.

Reviews of multiaxial fatigue calculation methods for structural materials are also provided in works [26–28].

An example of a model aimed at addressing the issue of ensuring the durability of aviation hydraulic pipelines is presented in work [29]. This study proposes an enhancement to the WYT (Weighted Yielding Theory) model, which assumes that different components of the stress state have varying 'weights' (significance) in their contribution to the overall effect, such as yielding or failure. In the modified model, the maximum shear stress τ_{max} is replaced with the maximum absolute shear stress $|\tau|_{max}$:

$$\frac{\Delta\gamma_{max}}{2}\left(1+\frac{|\tau|_{max}}{\tau'_f}\right)+\Delta\varepsilon_n\left(1+\frac{\sigma_{n,max}}{\sigma'_f}\right)=f\left(N_f\right).$$

The service-life prediction results for four material samples demonstrate that the modified model yields better results compared to the original WYT model. The prediction error using the modified model falls within the range of 2σ to 3σ.

The influence of anisotropy in multiaxial loading models based on equivalent stress approaches is most prominently represented in the Hill's and Barlat's models [30, 31].

Regarding classical critical plane models, such as by Findley's and Matake's ones, they do not account for anisotropy, which can lead to errors in predicting the fatigue behaviour of materials with pronounced texture, such as rolled aluminium alloys. This necessitates the development of modified models and their experimental verification.

V. T. Troshchenko has made a significant contribution to the study of metal fatigue, including the development of fatigue failure criteria and methods for assessing strength under multiaxial loading. For instance, in work [32], deformation and energy criteria for metal fatigue failure were formulated and experimentally validated. Methods for accelerated determination of fatigue limits based on deformation and energy criteria were analysed, and approaches for predicting fatigue resistance characteristics of metals were presented. These approaches take into account the effects of stress concentration, complex stress states, loading modes, and the presence of fatigue cracks.

5. ASSESSMENT OF ACCUMULATED FATIGUE DAMAGE UNDER IRREGULAR MULTIAXIAL LOADING

To evaluate accumulated fatigue damage under irregular multiaxial cyclic loading, it is necessary to have load history data, appropriate damage criteria, and a summation rule for accumulated damage.

The calculation of accumulated fatigue damage remains an unresolved challenge, even for uniaxial loading. Regarding multiaxial proportional and non-proportional loading, it can be confidently stated that this problem is far from being solved.

Work [33] provides a detailed review of fatigue damage accumulation theories. Despite the well-known shortcomings of the Palmgren–Miner rule [34], it remains the fundamental model for assessing accumulated fatigue damage under irregular cyclic loading, including multiaxial scenarios. According to it, the failure happens when the sum of relative damage riches 1: $\sum(n_i / N_i) = 1$, where n_i is the number of loading cycles at stress level i; N_i is the number of cycles to failure at stress level i, determined from the Wöhler's curve.

At the same time, non-linear rules for fatigue damage accumulation have been proposed. These aim to correct non-linearity by accounting for the actual sequence of stress cycles and the effect of stresses below the fatigue limit.

In work [35], it is noted that the shortcomings of the Palmgren–Miner rule may be due to the use of an incorrect damage parameter. It was shown that, in the calculation of accumulated fatigue damage under uniaxial loading of stainless steel, the linear summation rule provides sufficiently accurate results if a parameter is used that accounts for both stress and strain, rather than the conventional stress–cycles (S–N) or strain–cycles (ε–N) curves.

In the case of multiaxial fatigue, changes in loading modes can also influence durability. Studies [36, 37] have demonstrated that torsion preceding tension is more damaging than tension preceding torsion. In work [38], this phenomenon was explained by the fact that torsion cycles lead to the initiation of microcracks on planes where normal stresses promote their growth, whereas tensile stresses do not facilitate crack initiation.

At the same time, as demonstrated in work [39], in the case of low-cycle fatigue of titanium, the 'tension–torsion' sequence proved to be slightly more damaging than the 'torsion–tension' sequence.

Significant contributions to addressing this issue are the reviews presented in works [40, 41].

6. APPLICATION OF SOFTWARE PACKAGES FOR ANALYZING MULTIAXIAL CYCLIC LOADING

The capabilities of various software packages can be demonstrated through practical applications.

In work [42], the study focused on turbine blades of aircraft engines operating under high temperatures and pressures. The finite element method (FEM) implemented in ANSYS was used to model operating conditions and identify critical zones. The Chaboche's model [43],

which describes material behaviour under cyclic loading, served as the baseline. For evaluating the fatigue life of turbine blades, models such as Fatemi–Socie [24], Wang–Brown [44], and modified Smith–Watson–Topper [45] were employed. These models assess the strengthening effect under non-proportional cyclic loading and the influence of mean stress in multiaxial fatigue. They are applicable to both proportional and non-proportional loading scenarios.

Work [46] focused on practical cases of fatigue damage analysis using ABAQUS and Fe-Safe. As an example, the study analysed the fatigue damage of a nose landing gear support made of SAE4130 steel. The loading scenario included vertical load, lateral force, and internal pressure in a fluid-gas shock absorber, resulting in multiaxial repeated loading. The fatigue life of the nose landing gear support under multiaxial loading was assessed using the critical plane criterion. The orientation of the critical plane was determined by the Fe-Safe algorithm based on the Brown–Miller model [6], which is widely accepted for SAE4130 steel.

Among software packages for analysing multiaxial fatigue, notable examples also include Nastran [47], LS-DYNA [48], and others.

7. CONSIDERATION OF CRYSTALLOGRAPHIC ORIENTATION IN MULTIAXIAL FATIGUE CALCULATIONS

One of the factors driving the development of the critical plane concept was Findley's observation [18], which noted the crystallographic nature of damage localization. However, the process of microplastic deformation is determined not only by the orientation of the slip plane but also by the slip direction. For face-centred cubic crystals, there are 12 equivalent slip systems, comprising 12 combinations of slip planes in the {111} family and slip directions in the [110] family [49].

It is widely accepted that slip under loading begins in the system with the maximum value of the Schmid's factor, which is determined as $m = \cos(\varphi)\cos(\lambda)$, where ϕ is angle between the axis of loading and perpendicular to the slip plane; λ is angle between the axis of loading and slip direction.

Work [50] demonstrated that accounting for the actual stress components in the slip systems of crystallites when calculating the Mises's equivalent stress under proportional cyclic tension–torsion loading of aluminium alloy 2024 T3 samples improves the accuracy of accumulated fatigue damage assessment and failure prediction. The crystallographic orientation of the crystallites was assumed to follow the texture formed during rolling. This approach was further developed in the work [52] by application for the solving the practical issue: repair of the damaged aircraft structure by the patches oriented for minimizing equivalent stresses at the multiaxially loaded spot of the structure.

However, it should be noted that the maximum Schmid's factor is not the sole determinant in analysing the slip process. For instance, in work [53], it was shown that slip activation can occur in slip systems with Schmid's factors lower than the maximum among the 12 slip systems. Experiments involving tension of zone-refined, ribbon-shaped aluminium single crystals, using the Lang's x-ray topographic method, revealed multiple activated slip systems. At early stages of plastic deformation, slip systems with lower Schmid's factors may activate earlier than those with higher factors, depending on the crystal orientation relative to external surfaces.

8. CONCLUSION

The multitude of theories and models for multiaxial cyclic fatigue damage indicates the absence of a universal approach. The most commonly used methods are equivalent-stress models and critical-plane criteria, each with its own optimal application domain.

Despite well-known criticisms of the Huber–Mises theory, particularly regarding its neglect of anisotropy in metallic structural elements, the equivalent stress formula remains widely used in many methodologies for analysing stress–strain states.

The critical-plane criterion has proven its effectiveness and is widely applied, especially, in automated computations. It has been integrated into software packages designed to address the challenge of damage assessment under multiaxial cyclic loading.

Incorporating anisotropy in metallic materials is advisable at the microstructural analysis level. This approach views the damage process as a result of microplastic slips along slip systems.

AUTHORS' CONTRIBUTIONS

M. V. Karuskevych, T. P. Maslak contributed to the formulation of the problem and methods for its solution. O. M. Karuskevych, T. P. Maslak verified the analytical approaches, conducted a literature review that combines theoretical and applied aspects of the problem of multiaxial fatigue. T. V. Turchak, M. V. Karuskevych verified the analytical approaches, synthesized information on methods for determining damage accumulation under repeated loading, and prepared the manuscript of the article. All authors reviewed and approved the final version of the manuscript.

REFERENCES

1. *European Union Aviation Safety Agency. Certification Specifications and Ac-*

ceptable Means of Compliance for Large Aeroplanes (CS-25) (2023).
2. *Rozrakhunky ta Vyprobuvannia na Mitsnist. Metody Vyznachennia Ekvivalentnykh i Dopustymykh Napruzhen vid Statychnoho Navaazhennia* [Calculations and Strength Tests. Methods for Determining Equivalent and Allowable Stresses from Static Loading], DSTU Standard 2464-94, Derzhstandard Ukrainy (Kyiv: 1994).
3. *ISO/TR 12112:2018. Metallic Materials – Principle and Designs for Multiaxial Fatigue Testing* (Geneva: ISO: 2018).
4. *ASTM E2207-15 'Standard Practice for Strain-Controlled Axial-Torsional Fatigue Testing with Thin-Walled Tubular Specimens'*.
5. *American Petroleum Institute & American Society of Mechanical Engineers. API 579-1/ASME FFS-1 Fitness-for-Service* (4th ed.) (Washington, DC: API: 2021).
6. M. Brown and K. J. Miller, *Proc. Inst. Mech. Eng.*, **187**, Iss. 1: 745 (1973).
7. J. Draper, *Modern Metal Fatigue Analysis* (Warrington, UK: EMAS Publishing: 2008).
8. Y.-L. Lee, M. E. Barkey, and H.-T. Kang, *Metal Fatigue Analysis Handbook: Practical Problem-Solving Techniques for Computer-Aided Engineering* (1st ed.) (Oxford, United States: Elsevier Science & Technology: 2012).
9. J. L. Chaboche, *Int. J. Plast.*, **2**, No. 2: 149 (1986).
10. *BS EN 13445-3:2021+A1:2025. Unfired Pressure Vessels. Part 3: Design* (London: BSI: 2025).
11. *NORSOK N-004:2021. Design of Steel Structures* (5th ed.) (Lysaker: Standards Norway: 2021).
12. *AASHTO LRFD. Bridge Design Specifications* (10th ed.) (Washington, DC: American Association of State Highway and Transportation Officials: 2023).
13. *SAE J2432. Fatigue under Combined Loading* (Warrendale, PA: SAE International: 2017).
14. G. Lanza, *Trans. ASME*, **8**: 130 (1886).
15. H. J. Gough and H. V. Pollard, *Proc. Inst. Mech. Eng.*, **131**: 3 (1935).
16. H. J. Gough, *J. Appl. Mech.*, **17**, No. 2: 113 (1950).
17. *Behavior of Metals Under Complex Static and Alternating Stresses. Metal Fatigue* (Eds. G. Sines and J. L. Waisman) (New York: McGraw-Hill: 1959).
18. W. N. Findley, *J. Eng. Ind.*, **81**, No. 4: 301 (1959).
19. A. Fatemi and N. Shamsaei, *Int. J. Fatigue*, **33**, No. 8: 948 (2011).
20. N. Shamsaei and A. Fatemi, *Fatigue Fract. Eng. Mater. Struct.*, **32**: 631 (2009).
21. J. Papuga, M. Vargas, and M. Hronek, *Eng. Mech.*, **19**, Nos. 2/3: 99 (2012).
22. J. Z. Gyekenyesi, P. L. N. Murthy, and S. K. Mital, *NASALIFE—Component Fatigue and Creep Life Prediction Program* (Washington, DC: 2005).
23. Ye. V. Savchuk and S. M. Shukaiev, *Mech. Adv. Technol.*, **7**, No. 3: 279 (2023).
24. A. Fatemi and D. F. Socie, *Fatigue Fract. Eng. Mater. Struct.*, **11**, No. 3: 149 (1988).
25. Z. Engina and D. Coker, *Procedia Struct. Integr.*, **5**: 1229 (2017).
26. Y. Y. Wang and W. X. Yao, *Int. J. Fatigue*, **26**, No. 1: 17 (2004).
27. A. Karolczuk and E. Macha, *Eng. Fract. Mech.*, **75**, Nos. 3–4: 389 (2008).
28. Y. Jiang, O. Hertel, and M. Vormwald, *Int. J. Fatigue*, **29**, No. 8: 1490 (2007).
29. Y. Wang, Y. Qiu, J. Li, J. Bai, and Y. Wang, *Materials*, **17**, No. 24: 6154 (2024).
30. R. Hill, *Proc. R. Soc. A*, **193**, No. 1033: 281 (1948).

31. F. Barlat and K. Lian, *Int. J. Plast.*, **5**, No. 1: 51 (1989).
32. V. T. Troshchenko, *Deformatsiya i Razrushenie Metallov pri Mnogotsiklovoy Nagruzke* [Deformation and Fracture of Metals under Multicyclic Loading] (Kiev: Naukova Dumka: 1981) (in Russian).
33. A. Fatemi and L. Yang, *Int. J. Fatigue*, **20**, Iss. 1: 9 (1998).
34. M. A. Miner, *J. Appl. Mech.*, **12**, No. 3: 159 (1945).
35. J. Colin and A. Fatemi, *Fatigue Fract. Eng. Mater. Struct.*, **33**, No. 4: 205 (2010).
36. J. Miller, *Mater. Sci. Technol.*, **9**, No. 6: 453 (1993).
37. S. Harada and T. Endo, *On the Validity of Miner's Rule Under Sequential Loading of Rotating Bending and Cyclic Torsion, Fatigue Under Biaxial and Multiaxial Loading* (Eds. K. Kussmaul, D. McDiarmid, and D. Socie) (London: Mechanical Engineering Publications: 1991).
38. D. F. Socie and G. B. Marquis, *Multiaxial Fatigue* (Warrendale: SAE International: 2000).
39. N. Shamsaei, M. Gladskyi, K. Panasovskyi, S. Shukaev, and A. Fatemi, *Int. J. Fatigue*, **32**, No. 11: 1862 (2010).
40. A. Niesłony and E. Macha, *Spectral Method in Multiaxial Random Fatigue* (Berlin–Heidelberg: Springer-Verlag: 2007).
41. C. Braccesi, F. Cianetti, G. Lori, and D. Pioli, *Int. J. Fatigue*, **74**: 107 (2015).
42. J. Zhou, *Safety and Reliability – Safe Societies in a Changing World* (Eds. S. Haugen *et al.*) (Trondheim: CRC Press: 2018).
43. J. L. Chaboche, *Int. J. Plast.*, **5**, No. 3: 247 (1989).
44. C. H. Wang and M. W. Brown, *Fatigue Fract. Eng. Mater. Struct.*, **16**, No. 12: 1285 (1993).
45. T. Lagoda, S. Vantadori, K. Głowacka, M. Kurek, and K. Kluger, *Materials*, **15**, No. 10: 3481 (2022).
46. R. Lee, *ABAQUS for Engineers: Engineering Fatigue Analysis with Fe-Safe*, (Boca Raton, FL: CRC Press: 2023).
47. *MSC Nastran 2023. 2 Embedded Fatigue User Guide* (Newport Beach, CA: Hexagon AB: 2023).
48. Y. Huang, Z. Cui, and Z. Chen, *Proc. of the 16th International LS-DYNA Conference* (Detroit, USA: 2020).
49. A. G. Jackson, *Slip Systems. Handbook of Crystallography* (New York, NY: Springer: 1991).
50. T. Maslak and M. Karuskevich, *Fatigue Fract. Eng. Mater. Struct.*, **46**, No. 3: 1211 (2023).
51. M. Karuskevich, S. Ignatovych, T. Maslak, and O. Karuskevych, *Aviation*, **28**, No. 4: 255 (2024).
52. O. Lohne, *Phys. Status Solidi A*, **25**, No. 2: K179 (1974).

Metallophysics and Advanced Technologies
Металофіз. новітні технол.
Metallofiz. Noveishie Tekhnol.
2026, vol. 48, No. 4, pp. 435–447
https://doi.org/10.15407/mfint.48.04.0435
Reprints available directly from the publisher

PACS numbers: 06.30.Dr, 06.30.Gv, 62.25.Jk, 81.05.Bx, 81.70.Ha, 81.70.Jb, 81.70.Pg

Experimental Method for Determining the Composition of Materials in a Sample Using an Intelligent Ballistic Dual-Channel Gravimeter

O. M. Bezvesilna, Yu. M. Koval*, M. S. Grynevych, and T. A. Tolochko

National Technical University of Ukraine
'Igor Sikorsky Kyiv Polytechnic Institute',
37 Beresteiskyi Ave.,
UA-03056 Kyiv, Ukraine
**G. V. Kurdyumov Institute for Metal Physics, N.A.S. of Ukraine,*
36 Academician Vernadsky Blvd.,
UA-03142 Kyiv

This article proposes and examines an experimental method for determining the composition of materials in a sample using a new intelligent ballistic dual-channel transformer gravimeter (IBDTG) in a diagnostic setup (the GS gravimetric system). It is demonstrated that the IBDTG accuracy, speed, and reliability are superior to those of currently available gravimeters. Its design and operating principle are described. Currently, there are no theoretical or practical studies devoted to the feasibility and practicality of using an intelligent ballistic dual-channel transformer gravimeter to analyse metal composition in a sample or on a surveyed area of the Earth's surface. A new intelligent ballistic two-channel transformer gravimeter contains a fixed tube, a magnetized test body in the form of a ball, a device for holding the test body in the initial position, a computer and an inductance winding, which is distinguished by the fact that the fixed tube is made of a dielectric material, the inductance winding acts as a primary excitation winding connected to a pow-

Corresponding author: Olena Mykolayivna Bezvesilna
E-mail: o.bezvesilna@gmail.com

Citation: O. M. Bezvesilna, Yu. M. Koval, M. S. Grynevych, and T. A. Tolochko, Experimental Method for Determining the Composition of Materials in a Sample Using an Intelligent Ballistic Dual-Channel Gravimeter, *Metallofiz. Noveishie Tekhnol.*, **48**, No. 4: 435–447 (2026). DOI: 10.15407/mfint.48.04.0435

er source, which additionally contains two identical sections of a secondary output winding, connected in series-opposite to create two measurement channels, and the device for holding the test body in the initial position contains an electromagnet, which consists of an anchor made of a soft magnetic material and an additional winding, which is connected through a switch to an additional power source. This improves accuracy and reliability, reduces temperature dependence and sensitivity to cross-accelerations, and enhances linearity. The influence of vertical acceleration, instrumental errors, and errors due to non-identical parameters of the two channels are eliminated. The output signal power of the new IBDTG is increased by feeding the output signals of the two IBDTG channels to a computer, which generates an output signal from the gravimeter equal to twice the acceleration of gravity. The computer output signal is fed to a pre-trained Fuzzy module, which determines the metal composition of the sample or the area of the Earth's surface being studied.

Key words: Fuzzy module, intelligent ballistic two-channel transformer gravimeter, automated diagnostic gravimetric system, disturbance effect, vibration acceleration, acceleration of gravity.

У цій статті запропоновано та розглянуто експериментальний метод визначення складу матеріялів у зразку шляхом використання нового інтелектуального балістичного двоканального трансформаторного ґравіметра (ІБДТҐ) діягностичної установки (ґравіметричної системи ҐС). Обґрунтовано, що точність, швидкодія та надійність ІБДТҐ вище відомих нині ґравіметрів. Описано його конструкцію та принцип дії. Нині відсутні науково-теоретичні та практичні роботи, присвячені дослідженням можливости та доцільности використання інтелектуального балістичного двоканального трансформаторного ґравіметра для аналізи складу металів у зразку або на досліджуваній ділянці Земної поверхні. Новий інтелектуальний балістичний двоканальний трансформаторний ґравіметер містить нерухому трубку, намагнетоване пробне тіло у вигляді шару, пристрій утримання пробного тіла у початковому положенні, комп'ютер і обмотку індуктивности, який вирізняється тим, що нерухому трубку виконано з діелектричного матеріялу, обмотка індуктивности виконує роль первинної обмотки збудження, підключеної до джерела живлення, яке додатково містить дві однакові секції вторинної вихідної обмотки, включені послідовно-зустрічно для створення двох каналів міряння, а пристрій утримання пробного тіла у початковому положенні містить електромагнет, який складається з якоря із магнетом'якого матеріялу та додаткової обмотки, яку через перемикач підключено до додаткового джерела живлення. Водночас підвищуються точність і надійність, зменшуються залежність від температури, чутливість до перехресних пришвидшень та збільшується лінійність. Усуваються вплив вертикального пришвидшення, інструментальні похибки та похибки від неідентичности параметрів двох каналів. Збільшення потужности вихідного сиґналу нового ІБДТҐ забезпечується шляхом подачі вихідних сиґналів двох каналів ІБДТҐ у комп'ютер, в якому формується вихідний сиґнал ґравіметра, рівний подвоєному значенню пришвидшення сили тяжіння. Вихідний сиґнал комп'ютера подається на попередньо навчений Fuzzy-модуль, який ви-

значає склад металів у зразку або на досліджуваній ділянці Земної поверхні.
Ключові слова: Fuzzy-модуль, інтелектуальний балістичний двоканальний трансформаторний ґравіметер, автоматизована діягностична ґравіметрична система, збурювальний вплив, вібраційні пришвидшення, пришвидшення сили тяжіння.

(Received 23 March, 2026; in final version, 25 March, 2026)

1. INTRODUCTION

In many countries, diagnosing metal content in samples and detecting and diagnosing mineral deposits are extremely important. This information is used in various fields, including metal physics, geology, geophysics, surveying, and other fields. An experimental setup, called a gravimetric system (GS), whose sensing element is a gravimeter, can be used for this purpose. Gravimetric measurements are conducted on a fixed base (on the Earth's surface) and on a moving base (on submarines, surface vessels, and aircraft). Each type of measurement has its own advantages and disadvantages.

The most accurate measurements are made on Earth using the well-known ballistic gravimeter. It is possible to significantly increase the accuracy by using a diagnostic gravimetric system [3], the sensitive element of which is a new intelligent ballistic two-channel transformer gravimeter, the advantages of which over the known ballistic gravimeter are higher accuracy, speed, reliability, powerful output signal, linearity of characteristics over a wide range, *etc*.

The conducted analysis of the literature showed that a great contribution to the theory and practice of experimental gravimetric measurements is associated with the names of E. I. Popov, A. M. Lozinskaya, A. A. Andreev, V. V. Malov, N. A. Shulga, V. V. Lavrinenko, S. I. Pugachev, O. P. Kramarov, A. E. Kolesnikov, P. A. Gribovsky and others [1–34].

Several types of gravimeters and gravimetric systems are known, each with its own advantages and disadvantages. In [7], the elastic element and moving mass are made of a sapphire single crystal. The invention [8] improves accuracy by reducing zero drift, increasing the linearity range, and improving inertial noise filtration. In the gravimeter [9], the sensing element for determining the acceleration of gravity (AG) is made of silicon or glass. This provides the sensing element with relatively high reliability, accuracy, and stability of readings.

Leading technical universities in the USA, Japan, Germany and other countries are working on developing new models of GS gravimeters and improving their accuracy [14–17].

However, virtually all known gravimeters simultaneously measure

the useful gravity acceleration (GAC) signal g and the vertical acceleration interference signal [4, 12, 18], which is 10^3 times greater than the useful g signal [4, 12]. They require lengthy periodic calibration, adjustment, and output signal filtration [19], which significantly complicates their operation. Furthermore, known gravimeters do not allow for the detailed determination of the material composition of the sample or section of the Earth's surface being studied. Existing latest developments relate to marine [20, 21] and aviation [19] measurement methods, which are not used in terrestrial gravimetry.

In recent years, a ballistic gravimeter (BG) [2] has been used, consisting of systems for measuring the path and time of free motion of a test body. The BG includes a measurement system consisting of a test body in the form of a magnetic sphere, a transparent tube on a fixed base, an induction coil, a device for holding the test body in its initial position, and a computer.

The well-known gravimeter [2] has a number of significant disadvantages. The known gravimeter is a single-channel inductive device. When exposed to an external electromagnetic flux (interference), the known ballistic gravimeter experiences significant errors, acting along the OZ sensitivity axis simultaneously with the useful gravitational acceleration signal g and significantly greater it in 10^3. The vertical inertial acceleration, instrumental errors caused by changes in temperature, humidity, vibration, pressure, dry friction torque and other factors act directly along the sensitivity axis OZ, distorting the operation of the known gravimeter. The measuring system of a known gravimeter consists of two subsystems, each containing a large number of devices operating on different principles, each with its own inherent errors. Therefore, combining the two subsystems does not improve accuracy, as the errors of the devices in both subsystems will be additive. The multitude of parts and components of the measuring system of the known gravimeter and the complex connections between them significantly reduce the reliability and speed of operation of the known gravimeter. The known BG does not allow the analysis of the metal content in the sample being studied or in the area of the Earth's surface being studied.

It should also be taken into account that the accuracy of measuring the acceleration of gravity by a known ballistic gravimeter is significantly affected by external electromagnetic flows: interference.

Without eliminating the above-mentioned significant shortcomings, the accuracy, speed, and reliability of measurements of metal content in a sample or on a section of the Earth's surface being studied by a known ballistic gravimeter will be low.

This article proposes and reviews a new intelligent dual-channel ballistic gravimeter (IBDTG) [1], which has clear advantages over known gravimeters: IBDTG can measure the metal content in a sample or on a

section of the Earth's surface with greater accuracy, speed, and reliability, and also has a twice as powerful output signal.

2. SUMMARY OF THE ARTICLE CONTENTS

In order to improve the accuracy, speed and reliability of measurements of the metal content in a test sample or on a test section of the Earth's surface, as well as the measurement of the gravity field, an intelligent ballistic two-channel transformer gravimeter is proposed for measuring the doubled value of the acceleration of gravity, containing a fixed tube, a magnetized test body in the form of a ball, a device for holding the test body in the initial position, a computer and an inductance winding, in which the new feature is that the fixed tube is made of a dielectric material, the inductance winding acts as a primary excitation winding connected to a power source, which additionally contains two identical sections of the secondary output winding, connected in series-opposite to create two measurement channels, and the device for holding the test body in the initial position contains an electromagnet, which consists of an anchor made of a soft magnetic material and an additional winding, which is connected through a switch to an additional power source.

This improves accuracy and reliability, reduces temperature dependence and sensitivity to cross-acceleration, and enhances linearity. The influence of vertical acceleration is eliminated, as are instrumental errors and errors due to non-identical parameters of the two channels. The output power of the new IBDTG is increased by feeding the output signals of the two IBDTG channels to the computer input, from which a signal proportional to twice the value of AG is read. The computer output is connected to an intelligent Fuzzy module, the output of which is the output of the experimental setup (gravimetric system). The intelligent Fuzzy module is pre-trained using the gravitational anomaly signal Δg to determine the metal content in a given sample or to determine the composition of minerals in a given area of the Earth's surface. The results of measurements of the gravity anomaly Δg are automatically analysed in the intelligent Fuzzy module, which contains a database of fuzzy rules and linguistic variables and generates a logical conclusion regarding the presence and type of metals in a sample or the composition of minerals in a given area. The intelligent Fuzzy module enables the processing of multiple measured data sets when analysing the composition of metals in a sample or determining the composition of minerals in a given area in real time.

Today, there are no scientific, theoretical, or practical works devoted to the study of the possibility and feasibility of using a new intelligent ballistic gravimeter of a ground-based experimental setup (GS) [1] to determine the composition of metals in a sample or on a section of

the Earth's surface. Its advantages over the known ballistic gravimeter [2] are greater accuracy (due to the use of a pre-trained Fuzzy module, eliminating the impact of vertical acceleration, instrumental and other errors), speed of operation, and reliability [1].

The object of study of this article is the process of measuring the content of metals in a sample or on a section of the Earth's surface.

The purpose of this article is to improve the accuracy, speed and reliability of a new intelligent ballistic two-channel transformer gravimeter of a diagnostic experimental setup (gravimetric system) for determining the composition of materials in a sample.

The objectives of the article are to examine the design and analyse the operating principle of a new intelligent ballistic two-channel transformer gravimeter to ensure greater accuracy, power, speed, and reliability of the output signal through the use of a pre-trained Fuzzy module by eliminating the effects of vertical acceleration, instrumental and other errors.

3. RESEARCH METHODS AND MATERIALS

Below we will outline the main methods and materials of the study in accordance with the stated goals and objectives.

3.1. Design of an Intelligent Ballistic Two-Channel Transformer Gravimeter

We solve this problem by creating an intelligent ballistic dual-channel transformer gravimeter for measuring double the acceleration of gravity. This device comprises a stationary tube, a magnetized spherical test body, a device for holding the test body in its initial position, a computer, and an inductor winding. The new intelligent ballistic dual-channel transformer gravimeter is distinguished by its stationary tube being made of a dielectric material, the inductor winding serving as the primary excitation winding connected to a power source, the gravimeter additionally containing two identical sections of a secondary output winding connected in series-opposite fashion to create two measurement channels, and the device for holding the test body in its initial position containing an electromagnet consisting of a soft magnetic armature and an additional winding connected via a switch to an additional power source.

Figure 1 shows the structural diagram of an intelligent ballistic two-channel gravimeter with a pre-trained Fuzzy module for analysing the metal content in a sample.

Figure 2 shows a generalized diagram of the design of a new intelligent ballistic two-channel transformer gravimeter [1], showing how

error compensation is carried out.

The structural diagram of the intelligent BDTG (Fig. 1) shows a fixed tube *2* made of a dielectric material, attached to a base (not indicated in Fig. 1), containing a magnetized test body *1* in the form of a ball, which can move along the tube up and down parallel to the O*Z* axis. At the top of the tube *2* is a device *12* for holding the test body in its initial position, which consists of an electromagnet *6* consisting of an anchor *7* made of a soft magnetic material and an additional winding *8*. This additional winding *8* is connected via a switch *9* to an additional power source *10*.

On the outer part of the tube *2* there is an inductance winding *3*, which acts as a primary excitation winding and is connected to a power source *5*, and two identical sections *13*, *14* of the secondary output winding *4*, connected in series-opposite to create two measurement channels.

The outputs of the secondary output winding *4* are connected to computer *11*. The output power of the new intelligent IBDTG is increased by feeding the output signals of two IBDTG channels to the input of computer *11*, from which a signal proportional to twice the val-

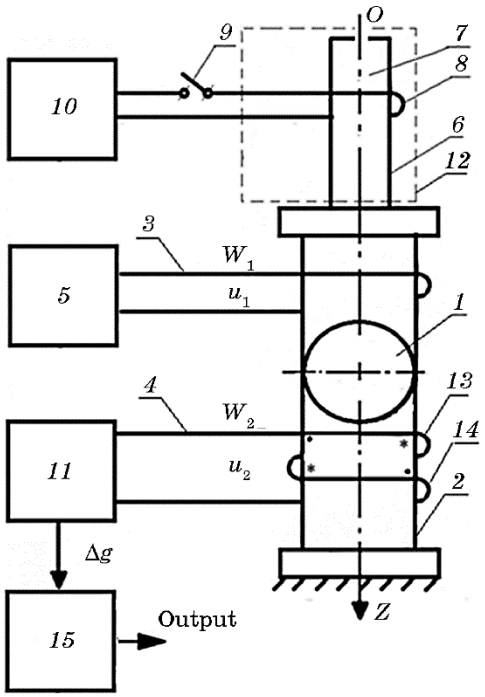

Fig. 1. Structural diagram of the intelligent ballistic dual-channel transformer gravimeter.

ue of g is read.

The output of computer *11* is connected to intelligent Fuzzy module *15*, the output of which is the output of the intelligent experimental setup (gravimetric system). Intelligent Fuzzy module *15* is pre-trained using the gravitational anomaly signal Δg to determine the types of metals in a given sample or the composition of minerals in a given area of the Earth's surface.

The results of measuring the gravitational anomaly Δg are automatically analysed in the intelligent Fuzzy module, which contains a database of fuzzy rules and linguistic variables and forms a logical conclusion regarding the composition of materials in the sample or the presence and type of minerals in a section of the Earth's surface. The intelligent Fuzzy Module *15* enables the processing of multiple measured data during sample composition analysis or in real time during the process of identifying minerals in a given area.

Figure 2 shows a generalized diagram of the design of an intelligent ballistic two-channel transformer gravimeter, where *1* is a test body of mass m, and *13* and *14* are the first and second sections of the secondary winding *4* of the intelligent ballistic two-channel transformer gra-

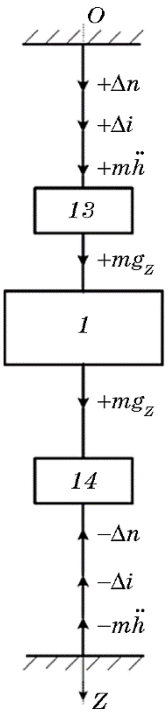

Fig. 2. Generalized diagram of the design of an intelligent ballistic two-channel transformer gravimeter (see Eq. (1)).

vimeter.

3.2. The Operating Principle of the Intelligent Two-Channel Ballistic Transformer Gravimeter

The proposed new intelligent BDTG works as follows. According to the law of electromagnetic induction, the excitation flux created by the primary excitation winding induces two oppositely directed electromotive forces in two sections of the secondary output winding, due to which, in the presence of effects from harmful external electromagnetic fluxes, inertial vertical acceleration, instrumental errors caused by changes in temperature, humidity, vibration, pressure, dry friction torque, residual non-identity of the parameters of two identical sections of the secondary output winding and other factors, their influence on the resulting accuracy of g measurement is eliminated. To create vertical movement in two opposite directions along the O*Z* axis of a test body in the form of a magnetized ball, the electromagnet winding is connected to a power source with a switch to create an electromagnetic flow of attraction of the test body, which, due to this, will rise to the extreme upper position, at the next moment the electromagnet switch is turned off, and the test body falls down under the action of gravity, the doubled output signal g, which is removed from the secondary winding, free from the influence of interference: external electromagnetic flows, inertial vertical acceleration, instrumental errors caused by changes in temperature, humidity, vibrations, pressure, the moment of dry friction forces, non-identity of the designs of two identical sections of the secondary output winding and other factors, is fed to the computer, from which the output signal of the gravimeter is removed, proportional to the doubled value of the SET.

The doubled value of the acceleration due to gravity is measured due to the fact that the output electrical signal of the ballistic two-channel transformer sensing element u_2, proportional to the total electromotive force of the two sections of the output secondary winding, will have the form (Fig. 2):

$$u_2 \equiv E_z = E_1 + E_2 \equiv mg + m\Delta\ddot{h} + \Delta i + \Delta n + mg - m\Delta\ddot{h} - \Delta i - \Delta n = 2mg\,, \qquad (1)$$

where E_1 is output signal from the first section of the secondary winding, E_2 is output signal from the second section of the secondary winding, $u_2 \equiv E_z$ is output signal of the ballistic two-channel transformer sensitive gravimeter, m is mass of the test body, Δh is vertical acceleration error, Δi is instrumental errors, Δn is errors of non-identity of parameters of two identical sections of the secondary winding.

The generalized diagram of a ballistic two-channel transformer gravimeter is shown in Fig. 2.

$$\Delta g = u_2 - \gamma_0 , \tag{2}$$

where γ_0 is reference value of acceleration due to gravity [4].

From equation (1), it is evident that the output signal of the ballistic two-channel transformer gravimeter u_2 contains the doubled value of the useful signal AG and does not contain the inertial vertical acceleration $\ddot{h}$, total instrumental Δi errors, errors from non-identity of parameters of two sections of the secondary output winding, which increases the accuracy of measurements, Signal u_2 is fed to the computer input, from the output of which a signal proportional to the doubled value of the SET is taken.

Output is connected to an intelligent Fuzzy module, whose output is the output of the experimental setup (gravimetric system). The intelligent Fuzzy module is pre-trained using the gravitational anomaly signal Δg to determine the types of metals in a given sample or the composition of minerals in a given area of the Earth's surface.

The results of gravitational anomaly Δg measurements are automatically analysed in the intelligent Fuzzy module, which contains a database of fuzzy rules and linguistic variables and generates a logical conclusion regarding the presence and type of metals in the sample or the presence and composition of minerals in a given area of the Earth's surface. The intelligent Fuzzy module enables the processing of multiple measured data during the analysis of metal composition in a sample or in real time during the determination of mineral composition in a given area.

The design features of the intelligent ballistic dual-channel transformer gravimeter significantly improve the accuracy, speed, and reliability of measurements. This enables highly accurate, reliable, and fast determination of the metal composition of a sample or the presence and composition of mineral deposits in a given area of the Earth's surface.

4. CONCLUSION

An analysis of the operation of a well-known ballistic gravimeter is conducted.

Its main shortcomings limiting its application are noted, namely: does not allow one to determine the content of metals in a sample or the presence and composition of minerals in the area of the Earth's surface being studied, the known gravimeter is a single-channel inductive device.

When exposed to an external electromagnetic flux, the known gravimeter experiences significant errors, acting along the O*Z* sensitivity axis simultaneously with the useful gravitational acceleration signal g and significantly exceeding it, the vertical inertial acceleration, in-

strumental errors caused by changes in temperature, humidity, vibration, pressure, dry friction torque and other factors act directly along the sensitivity axis OZ, distorting the correct operation of the known gravimeter.

The first and second subsystems of the known gravimeter consist of a large number of devices operating on different principles, each with its own inherent errors. Therefore, combining the two subsystems does not improve accuracy, as the errors of the devices in both subsystems will be additive, the multitude of parts and components of the measuring system of the known gravimeter and the complex connections between them significantly reduce the reliability of such a system.

The relevance of applying an experimental method for determining the metal composition of a sample using a new intelligent dual-channel ballistic transformer gravimeter, which eliminates the aforementioned shortcomings of existing ballistic gravimeters, is substantiated. It is demonstrated that the new IBDTG has a twice-powerful output signal and greater accuracy due to the presence of a pre-trained Fuzzy module, which provides analysis of the metal content in the sample, as well as compensation for vertical acceleration, instrumental errors, errors due to the non-identical design of the two channels, errors due to changes in temperature, humidity, pressure, and other factors. The new IBDTG is also more reliable, as it has fewer parts and components of the measuring system with different operating principles and fewer complex connections between them.

This article presents the following new results: for the first time, the scientific aspects of applying a new experimental method for determining the composition of metals in a sample using an intelligent dual-channel ballistic transformer gravimeter with a pre-trained Fuzzy module are presented. It is demonstrated that the new intelligent BDTG possesses greater accuracy, speed, and reliability.

The practical value of the results obtained in this article is that the feasibility of the practical use of a new experimental method for determining the composition of metals in a sample by using an intelligent ballistic two-channel transformer gravimeter is substantiated, since it has greater accuracy, speed and reliability compared to the known single-channel ballistic gravimeter, has a simpler design and a doubled output signal.

AUTHORS' CONTRIBUTIONS

O. M. Bezvesilna provided a description of the IBDTG design, explained the physics of the IBDTG operation, formulated the research task. Yu. M. Koval explained the physics of the IBDTG operation, provided the principle of operation of the IBDTG. M. S. Grynevych performed a literature review on the topic of the study. T. O. Tolochko

participated in presenting the literature review and its analysis, formatted the article.

REFERENCES

1. O. M. Bezvesilnaya, S. A. Nechay, and T. A. Tolochko, *Ballistic Two-Channel Transformer Gravimeter*, Patent for Utility Model No. 159371 (Published May 21, 2025) (in Ukrainian).
2. O. M. Bezvesilnaya, *Ballistic Gravimeter*, Patent of Ukraine No. 98058 (Published April 10, 2012) (in Ukrainian).
3. O. M. Bezvesilnaya and A. G. Tkachuk, *Aviation Gravimetric System for Measuring Gravity Acceleration Anomalies*, Patent of Ukraine No. 107637 (Published January 26, 2015) (in Ukrainian).
4. O. M. Bezvesilnaya, *Acceleration Measurements* (Kyiv: Lybid: 2021) (in Ukrainian).
5. O. M. Bezvesilnaya and T. A. Tolochko, *Tekhnichna Diahnostyka ta Neruinivnyi Kontrol*, No. 1: 16 (2025).
6. O. Bezvesilnaya, S. Nechai, M. Hrynevych, and T. Tolochko, *Herald of the Khmelnytsky National University. Techn. Sci.*: **355**, No. 4: 753 (2025).
7. O. M. Bezvesilnaya and G. S. Tymchik, *Technological Measurements and Devices. Transforming Devices of Devices* (Zhitomir: ZhTU: 2012) (in Ukrainian).
8. O. M. Bezvesilnaya and A. G. Tkachuk, *Three-Coordinate Piezoelectric Gravimeter of Aviation Gravimetric System*, Patent of Ukraine No. 113033 (Published November 25, 2016) (in Ukrainian).
9. Y. Huang, A. V. Olesen, M. Wu, and K. Zhang, *Sensors*, **12**, Iss. 12: 9336 (2012).
10. A. G. Tkachuk and O. M. Bezvesilnaya, *Transformer Gravimeter*, Patent for Utility Model No. 142824 (Published June 25, 2020) (in Ukrainian).
11. B. B. Samotokin, *Lektsiyi z Teoriyi Avtomatychnoho Keruvannya* [Lectures on the Theory of Automatic Control] (Zhitomir: ZHITI: 2001) (in Ukrainian).
12. O. M. Bezvesilnaya and N. V. Ilchenko, *Methods and Means of Improving the Accuracy Characteristics of an Instrumented System for Measuring Mechanical Parameters and Stabilization* (Kyiv: Igor Sikorsky Kyiv Polytechnic Institute: 2020) (in Ukrainian).
13. C. Roussel, J. Verdun, J. Cali, and M. Maia, *Int. Archives of the Photogrammetry, Remote Sensing and Spatial Information Sci.*, **XL-5/W5**: 199 (2015).
14. E. N. Bezvesilnaya, Y. V. Kyrychuk, M. S. Hrynevych, and T. A. Tolochko, *Bulletin of the Karaganda University Physics Series*, **112**, No. 4: 23 (2023).
15. I. Korobiichuk, O. Bezvesilna, A. Tkachuk, A. Praczukowska, and T. Khylchenko, *Systems, Control and Information Technology (May 20–21, 2016)* (Warsaw: 2016), p. 481.
16. K. Hehl, *Int. Association of Geodesy Symposium*, No. 113: 161 (1994).
17. C. Jekeli, *Bulletin Géodésique*, **69**, No. 1: 1 (1995).
18. C. Jekeli and J. H. Kwon, *Geophysical Research Lett.*, **26**, No. 3: 3533 (1999).
19. Y. Huang, A. V. Olesen, M. Wu, and K. Zhang, *Sensors*, **12**, Iss. 7: 9336 (2012).
20. M. Calvoa, J. Hinderera, S. Rosata, H. Legrosa, J.-P. Boya, B. Ducarmec, and W. Zürnd, *J. Geodynamics*, No. 80: 20 (2014).
21. G. Agostino, S. Desogus, A. Germak, C. Origlia, D. Quagliotti, G. Berrino,

G. Corrado, V. Derrico, and G. Ricciardi, *Annals of Geophysics*, No. 51: 39 (2008).
22. C. Roussela, J. Verduna, J. Calia, and M. Maiab, *The Int. Archives of the Photogrammetry, Remote Sensing and Spatial Information Sciences*, No. XL-5/W5: 199 (2015).
23. O. Bezvesilnaya, L. Chepyuk, A. Tkachuk, S. Nechai, and T. Khylchenko, *Technology Audit and Production Reserves*, **3**, No. 1: 53 (2017).
24. O. M. Bezvesilnaya, *Aviation Gravimetric System for Measuring Gravity Acceleration Anomalies*, Patent of Ukraine No. 105122 (Published April 10, 2014) (in Ukrainian).
25. O. M. Bezvesilnaya and A. G. Tkachuk, *Aviation Gravimetric System for Measuring Gravity Acceleration Anomalies*, Patent of Ukraine No. 113038 (Published November 25, 2016) (in Ukrainian).
26. T. V. Khylchenko, *Electronic Modeling*, **40**, No. 3: 87 (2018).
27. Y. Bezvesilnaya, S. Nechai, and T. Tolochko, *String Accelerometer of the Automated System* (DeProMonograph: 2025).
28. A. Tkachuk, O. Bezvesilna, I. Kryzhanivska, and M. Bogdanovsky, *Sci. Heritage*, No. 142: 58 (2024).
29. O. Bezvesilnaya, *Aviation Gravimetric System for Measuring Gravity Anomalies*, Patent of Ukraine No. 109746 (Published September 25, 2015) (in Ukrainian).
30. O. Bezvesilna, S. Nechai, and T. Tolochko, *Proc. of the 8th Int. Sci. Practical Conf.* (Berlin: 2024), p. 77.
31. O. M. Bezvesilnaya, L. V. Kolomiets, M. S. Grynevych and T. O. Tolochko, *Collection of Scientific Works of the Odessa State Academy of Technical Regulation and Quality*, **1**: 17 (2022).
32. O. M. Bezvesilnaya and M. S. Hrynevych, *Tavria Scientific Bulletin. Series: Technical Sci.*, **6**: 3 (2022).
33. O. M. Bezvesilnaya and A. G. Tkachuk, *Strain Gauge Gravimeter*, Patent of Ukraine No. 132179 (Published February 11, 2019) (in Ukrainian).
34. O. M. Bezvesilnaya, *Aviation Gravimetric System for Measuring Gravity Acceleration Anomalies*, Patent of Ukraine No. 105949 (Published July 10, 2014) (in Ukrainian).